600
10-19-78

Lg. 650

IRT-7021-019

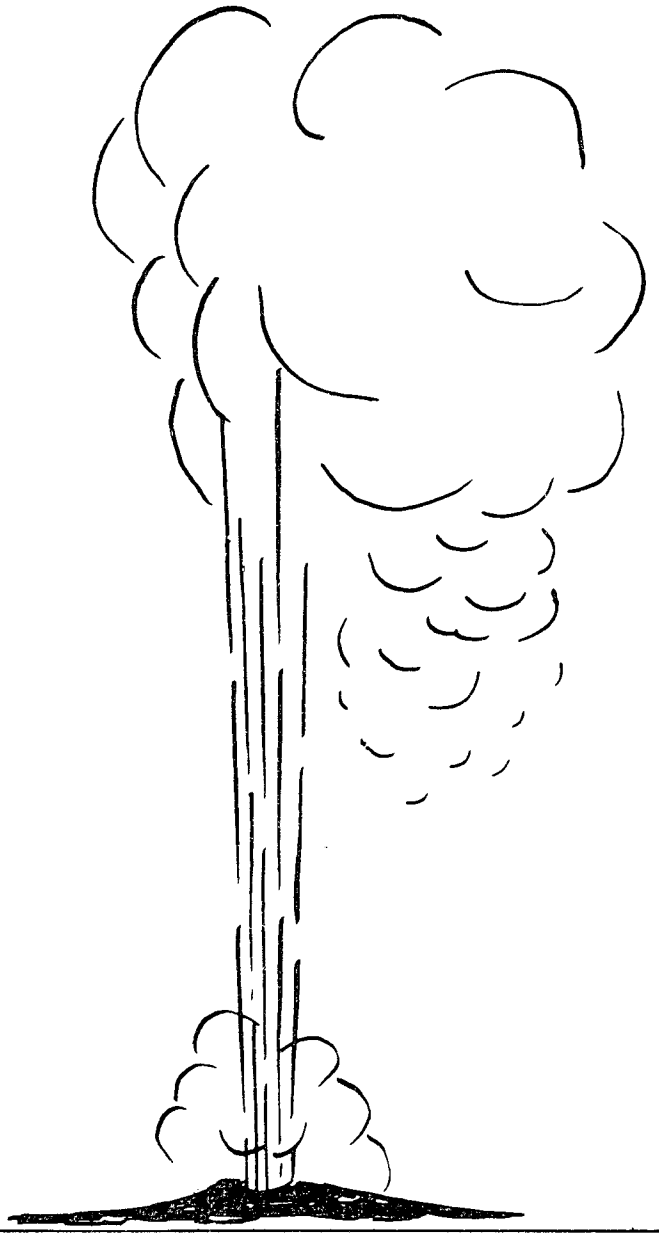

NEUTRON FORMATION TEMPERATURE GAUGE AND NEUTRON ACTIVATION ANALYSIS BRINE FLOW METER

Final Report, October 1, 1976—March 31, 1978

By
Nicholas Vagelatos
Donald K. Steinman
Joseph John

March 31, 1978

Work Performed Under Contract No. EY-76-C-03-0936

IRT Corporation
San Diego, California

U. S. DEPARTMENT OF ENERGY

Geothermal Energy

DISCLAIMER

NOTICE

IRT-7021-019
Distribution Category UC-66b

NEUTRON FORMATION TEMPERATURE GAUGE AND NEUTRON ACTIVATION ANALYSIS BRINE FLOW METER

FINAL REPORT

October 1, 1976 through March 31, 1978

Nicholas Vagelatos, Donald K. Steinman,
and Joseph John

Prepared for
DEPARTMENT OF ENERGY
Under
Contract EY-76-C-03-0936, A48

March 31, 1978

TABLE OF CONTENTS

TABLE OF CONTENTS (continued)

LIST OF FIGURES

ACKNOWLEDGMENTS

The authors wish to express their appreciation to various people for their contributions to this study. We would like to thank Mr. J. C. Young for the original estimates of the temperature gauging technique sensitivity, Professor G. C. Summerfield of the University of Michigan Nuclear Engineering Department for the neutron transport calculations, Mr. D. H. Houston for the GGC code neutron flux computations, Mr. W. J. Smith for technical assistance in preparation of the experimental equipment, and Mr. R. L. Palmer for assistance in data acquisition. We also wish to thank Mr. H. R. Lukens for the estimates of photon count rates used in assessing the flow gauging technique.

The authors especially wish to thank Mr. H. J. Weber for invaluable critical evaluation of the study.

We would like to thank Ms. L. L. Sanders and Mrs. V. G. Pitts for their assistance in manuscript preparation, handling of correspondence, and other office matters. We also wish to thank the IRT Publications Department personnel for the preparation of this report, as well as for numerous monthly reports.

ABSTRACT

Feasibility studies of nuclear techniques applicable to the determination of geothermal formation temperature and two-phase brine flow downhole have been performed. The formation temperature gauging technique involves injection of fast neutrons into the formation and analysis of the moderated slow neutron energy distribution by appropriately filtered neutron detectors. The scientific feasibility of the method has been demonstrated by analytical computation and experimental evaluation of the system response. A data analysis method has been developed to determine unambiguously the temperature, neutron absorption cross section and neutron moderating power of an arbitrary medium. The initial phase of a program to demonstrate the engineering feasibility of the technique has been performed. A sonde mockup was fabricated and measurements have been performed in a test stand designed to simulate a geothermal well. The results indicate that the formation temperature determined by this method is independent of differences between the temperature in the borehole fluid and the formation, borehole fluid density, and borehole fluid salinity. Estimates of performance specifications for a formation temperature sonde have been made on the basis of information obtained in this study and a conceptual design of a logging system has been developed. The technique for the determination of fluid flow in a well is based on neutron activation analysis of elements present in the brine. An analytical evaluation of the method has been performed. The results warrant further, experimental evaluation.

A patent application covering the temperature gauge system described in this report is on file at the U.S. Patent Office. The patent application addresses uses of the system for remote, noncontact temperature measurements in boreholes and other environments. In addition, applications of the system's ability to measure the neutron absorbtion cross section and the neutron moderating power of arbitrary media are covered by the patent application.

1. INTRODUCTION

Geothermal well logging is currently in a very early stage in its development, and the biggest effort by far is being made to adapt the technology developed over many years of oil well logging for geothermal reservoir evaluation. In many instances, this involves upgrading conventional instrumentation to withstand the hot, highly corrosive geothermal environment. Several geothermal well or reservoir parameters, however, cannot be determined reliably by conventional means. Such parameters may be essential in assessing the reservoir potential, or in providing a basis for timely decision making for field development and efficient resource exploitation. It is a goal of the IRT geothermal program to develop and make commercially available instrumentation for the determination of these parameters.

Formation temperature, pressure, and fluid flow are generally considered by the geothermal community as the three most important parameters in assessing geothermal well potential. The work discussed in this report has addressed the applicability of nuclear techniques for the determination of the formation temperature and downhole fluid flow rates. It constitutes feasibility studies of concepts developed at IRT. By far the greater emphasis has been placed on the development of a formation temperature sensor. This work includes a computational analysis, as well as experimental evaluation of the formation temperature gauging concept to demonstrate its feasibility. Only analytical evaluation of the concepts applicable to the determination of brine flow rates has been performed.

Conventional means for determining geothermal formation temperature are indirect, extremely time consuming, and not very reliable. Current techniques make use of conventional temperature sensors, e.g., thermocouples, thermistors, to measure the temperature of the borehole fluid. The formation temperature is inferred from such measurements either by extrapolation of the fluid temperature change with time or by assuming that thermal (temperature) equilibrium has been achieved between the borehole fluid and the surrounding formation. The extrapolation technique requires many hours (< 24) to several days of data gathering for a single temperature

determination. The second method is even slower, requiring many days (even a few months) for the onset of temperature equilibrium. Both methods are adversely affected by convection currents and other fluid circulation. Current (impeller type) flow meters are not applicable to two-phase (steam-water) fluid flow. In view of the importance of these parameters, and in order to expedite geothermal industry development, it is desirable that new technology be developed now which can provide the necessary information in a direct, rapid, reliable manner.

The neutron formation temperature gauging technique studied is based on well established principles of neutron moderation and thermalization theory (Refs 1,2). It involves injection of energetic neutrons into the formation and analysis of the moderated, slow neutron energy spectrum which is determined by the formation temperature, and its neutron absorption and moderating properties. Although the underlying theory is not new, the technique for analyzing the slow neutron spectrum is. It makes use of three appropriately filtered neutron detectors. Cross plotting of observed detector responses allows unambiguous determination of the temperature, and the neutron absorption cross section and moderating power of an arbitrary medium (formation). The technique is simple, direct, noncontact, and much faster than methods currently used. It appears at this point that an instrument based on the above method can best be utilized during drilling to measure bottomhole temperatures between changes of the drill bit. It is at this time that the formation will be least disturbed and the radial temperature profile will be flat up to a very small distance from the borehole wall.

The fluid flow gauging techniques examined are based on in-situ neutron activation analysis (NAA) of the brine. Elements generally found in geothermal brines are activated by neutrons from a source in a sonde, and the subsequent decay gamma radiation is monitored by detectors appropriately located in the instrument. The method does not require direct contact with the fluid. It requires only that the brine contain an activatable element. Therefore, the present methods are applicable to two-phase fluid flow as long as each phase contains a proportionate amount of the activatable substance.

The neutron formation temperature concept and the methodology for the unambiguous determination of the formation temperature are discussed in subsection 2.1 of this report. Subsection 2.2 discusses the various essential components of the system. The computational analysis of the gauge response is described in subsection 2.3. Measurements which demonstrate the scientific feasibility of the

method, as well as the initial experiments intended to demonstrate its engineering feasibility are discussed in subsection 2.4. Subsection 2.5 discusses a formation temperature sonde performance specifications estimates based largely on the results of the measurements. The conceptual design of a temperature logging system is also described in subsection 2.5. The NAA brine flow gauging methods and analysis are presented in Section 3. Further experimental work necessary to complete the demonstration of the engineering feasibility of the formation temperature gauge and to delineate its design specifications, and the need for experimental evaluation of the fluid flow gauge are discussed further in the concluding section of this report.

2. FEASIBILITY STUDY OF THE FORMATION TEMPERATURE GAUGE

2.1 UNDERLYING PRINCIPLES

The concepts underlying the technique for the determination of the formation temperature are discussed in this section. This discussion of the theory is followed by a description of the general method implementing these concepts. Details of the method are presented in subsection 2.2 which describes the various components of the temperature sensor. Subsection 2.3 describes a computational analysis of the method and subsection 2.4 discusses the experimental study of the temperature gauge response. Subsection 2.5 presents a concept design of a formation temperature sonde.

2.1.1 General Theory

When energetic (fast) neutrons are injected into a moderating medium, they propagate through it undergoing collisions with the surrounding atoms. As a result, their energies are reduced in elastic and inelastic interactions. Unless they are absorbed during the slowing-down process, neutrons eventually achieve thermal equilibrium with the moderating medium. That is, their kinetic energies are reduced to the range of thermal (periodic) motions of the various atoms. Thereafter, the slow neutrons diffuse through the medium (until they are absorbed or they decay) neither losing nor gaining additional energy, in the average, in subsequent collisions.

Because of the thermal motion of the interacting atoms and the statistical (random) nature of neutron propagation and diffusion, the slow neutron energies are not all equal, but they are distributed over a range of values. Since slow neutrons are in thermal equilibrium with their surroundings, their energy distribution reflects the thermal state of the medium, i.e., its temperature, as well as its neutron properties, i.e., absorption and scattering (Ref 1). The slow neutron spectrum generally consists of two distinct components. The thermal component occupies the lower energy part of the spectrum while the epithermal component occupies the higher energy portion, the slowing down region.

The slow neutron energy distribution is reflected in the energy dependence of the slow neutron flux. This quantity is the product of the density n(E), of neutrons with kinetic energy E, and their velocity, v(E). It is the neutron field parameter which, in conjunction with the moderator properties, determines the neutron interaction rates, e.g., scattering, absorption, etc. The slow neutron flux is generally represented accurately by the expression

$$\Phi(E) = 2\pi n \left(\frac{2}{m_n}\right)^{1/2} \cdot \left(\pi k T_n\right)^{-3/2} \cdot E \cdot \exp\left(-E/kT_n\right) + CE^{-1}, \qquad (1)$$

where $\Phi(E)$ = neutron flux; n = neutron density, m_n = neutron mass, k = Boltzman constant, E = neutron kinetic energy, T_n = neutron temperature, and C = constant.

The first term in Equation 1 is a Maxwellian function representing the thermal component of the moderated (slow) neutron flux. It is this part of the spectrum which is sensitive to the moderator temperature via the parameter T_n (Ref 1). This parameter is discussed further in following paragraphs. The second term in Equation 1 consists of neutrons with energies in the slowing down region of the slow neutron energy distribution. The constant C which determines the amplitude (neutron population) of this spectral region is independent of the moderator temperature and neutron absorption, and is determined entirely by the neutron moderating properties of the medium.

As previously noted, the slow neutron energy distribution is determined, in part, by the temperature of the moderating medium. This occurs, because T_n which characterizes the thermal component of the spectrum is a function of the moderator temperature, T. Figure 1 presents several slow neutron spectra calculated on the basis of Equation 1 for a single moderating medium, but for various values of the neutron temperature. These spectra clearly display the dependence of the thermal region on T_n. Since the various spectra shown correspond to the same medium, i.e., the same neutron properties,these distributions also exhibit the spectral dependence on moderator temperature. The figure also displays the insensitivity of the spectrum in the slowing down region to the temperature of the moderating medium.

If the neutron temperature depended on the medium temperature only, i.e., if $T_n = T_n(T)$, the temperature, T, could be determined simply by a single measurement of $\Phi(E)$ at $E = E_o$ (or in the region $E_o \leqslant E \leqslant E_o + \Delta E$) within the range of the thermal component of the spectrum. The situation, however, is not as simple as this, because, as previously noted, the slow neutron energy distribution depends on the neutron

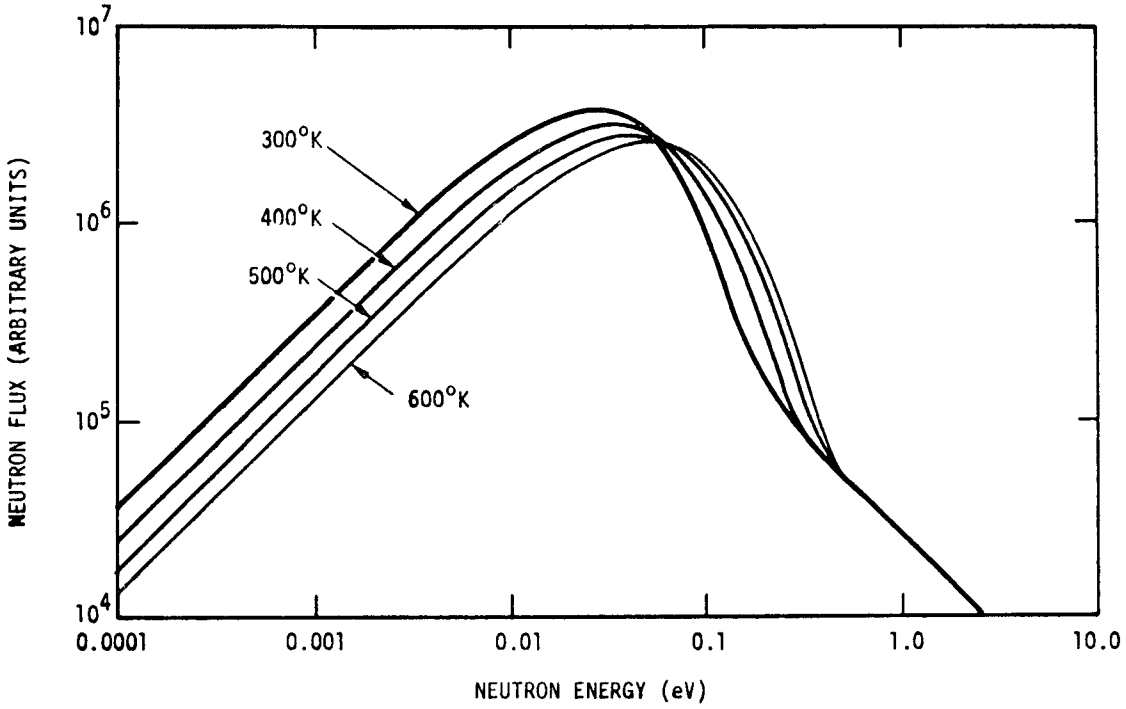

Figure 1. Thermal neutron energy distributions in a moderating medium for several values of the neutron temperature, T_n, calculated on the basis of Equation 1. Since the neutron properties of the medium are the same in each case, these distributions clearly display the spectral dependence on the moderator temperature. Generally, $T_n = T_n(T, \Sigma_a, \xi\Sigma_s)$.

properties of the moderating medium as well as on its temperature. More specifically,

$$T_n = T_n\,(T,\ \Sigma_a,\ \xi\Sigma_s) \qquad , \tag{2}$$

where T = moderating medium temperature, Σ_a = neutron absorption cross section, Σ_s = neutron scattering cross section, and ξ = average logarithmic energy loss per neutron collision with a moderator atom. $\xi\Sigma_s$ is the moderating power of a medium, i.e., a measure of its effectiveness in slowing down fast neutrons.

The specific functional dependence of T_n on the temperature and neutron properties of the moderating medium is determined by the geometry of the medium and the neutron source. For example, in an infinite medium with a uniformly distributed neutron source

$$T_n = T \cdot \left(1 + \alpha \frac{\Sigma_a}{\xi\Sigma_s}\right) \tag{3}$$

where α is an empirical constant (Ref 1,2). The validity of Equation 3 has been demonstrated for nuclear reactor cores where the above conditions are closely approximated. In contrast, the relationship corresponding to the case of a point source in an infinite medium is very complex. In this case, T_n is an integral function of T, Σ_a and $\xi\Sigma_s$ (See Appendix). Regardless of the complexity of the above expression, however, T_n (and thus, the slow neutron energy distribution) depends on the same three properties of the medium, namely the temperature, the neutron absorption cross section, and the neutron moderating power.

Since the information regarding the moderating medium temperature is implicit in the energy distribution of neutrons propagating through it, the temperature can be determined by properly analyzing the moderated neutron spectrum. The implication of the neutron temperature dependence on the neutron properties in addition to temperature is that the procedure is more involved requiring more than the single measurement discussed previously. One obvious method of analysis would involve the point by point determination of the entire slow neutron spectrum using the well known techniques of slow neutron spectrometry. This elaborate procedure, however, is time consuming and requires the use of bulky equipment. As such, it is not practical for borehole logging applications. The present technique is much simpler and faster, and it

is suitable for downhole measurements. It requires the measurement of neutrons with energies in three appropriately chosen regions in the slow neutron energy range. These regions are chosen so that the results of each set of three measurements bears a one-to-one correspondence with the set of conditions under which the measurements are performed, i.e., T, Σ_a, and $\xi\Sigma_s$. This method leads to the unambiguous determination of the medium (formation) temperature and, simultaneously, its neutron absorption cross section and moderating power.

2.1.2 Methodology

Implementation of the above concepts to actually determine the temperature of an arbitrary medium, i.e., geothermal formation, involves placing a temperature gauge, in a sonde, next to the medium (formation) of interest. The temperature sensor consists of a fast neutron source and three detectors sensitive to neutrons with energies in three different regions of the slow neutron range. Figure 2 presents a schematic diagram of the gauge. A Cf-252 fast neutron source and He-3 gas filled proportional neutron counters are particularly suitable for this application. The characteristics of the essential components of the system will be discussed in subsection 2.2. The response of the various detectors and the procedure for determining the formation temperature are discussed in this subsection with reference to the important general neutron properties of the various components.

The neutron temperature sensor (Figure 2) is placed downhole next to the formation whose temperature is to be determined. A large fraction of the neutrons emitted by the source enter the formation, propagate through it, and a large number of these achieve thermal equilibrium. The slow neutrons diffuse through the formation and many of them eventually escape (leak) back into the borehole. The energies of the slow leakage neutrons are distributed in a spectrum identical to that of the slow neutrons still diffusing through the formation. Therefore, the leakage slow neutron spectrum contains all the information regarding the formation temperature and neutron properties. When properly analyzed, this spectrum yields the values of these parameters.

The penetration distance of neutrons into the formation, i.e., the range of investigation, depends on the initial neutron energy and the formation neutron properties. The latter are largely determined by the formation hydrogen content, i.e., saturated porosity, and the salinity of the brine. The penetration depth of the formation temperature gauge can best be determined experimentally. This distance should be similar to

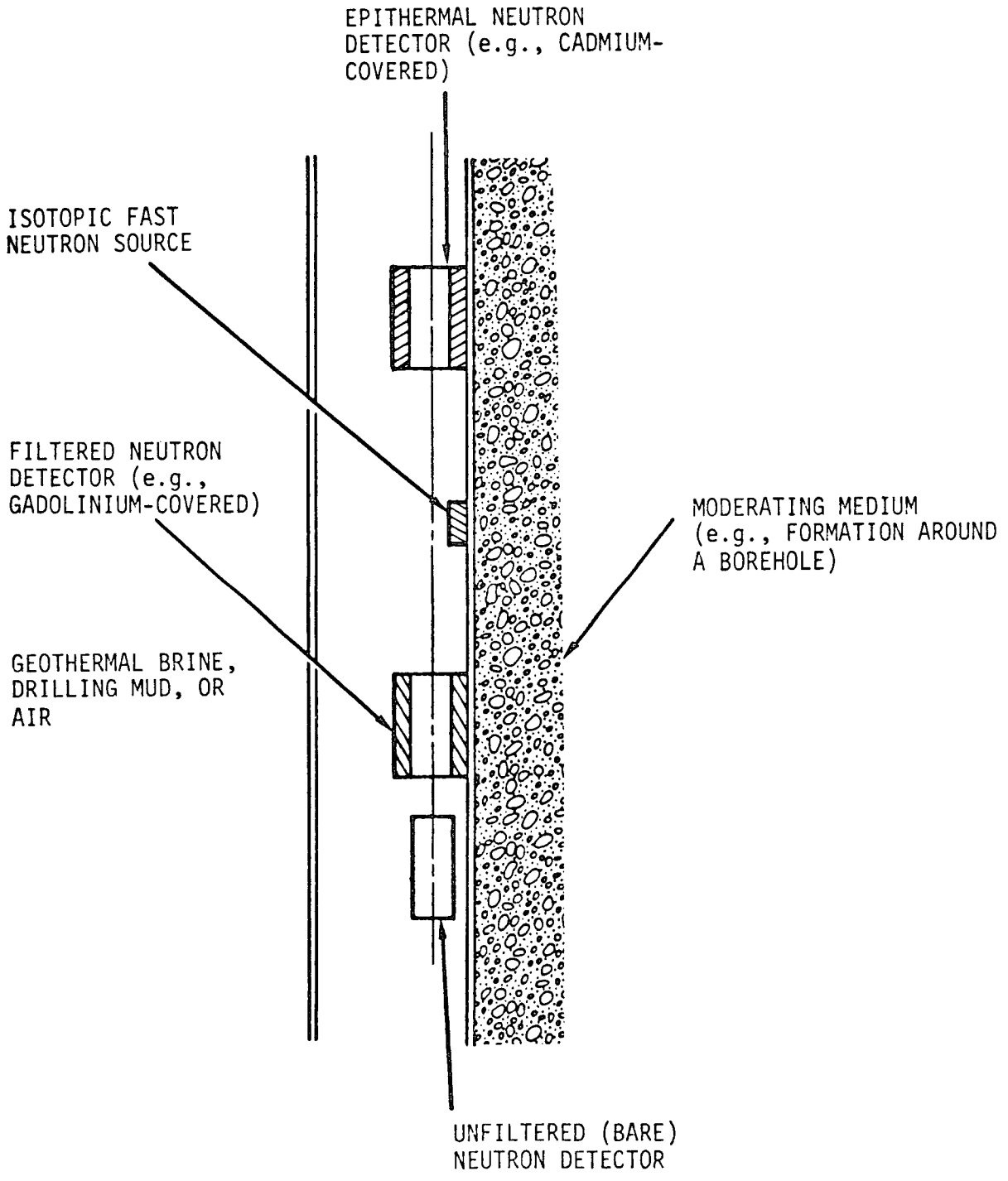

Figure 2. Schematic diagram of the formation temperature sensor showing the essential components of the system. The "sonde" is shown in the side-walled configuration which is appropriate for minimizing borehole fluid interference.

those appropriate to other neutron-neutron logging tools. It should be between five and ten inches (Ref 3,4).

Three neutron detectors, e.g., He-3, are placed in the sonde near the neutron source. When the tool is sidewalled as in Figure 2, the detectors are located next to the formation to analyze (sample) the leakage slow neutron spectrum with minimum interference from the borehole fluid. The various detectors are made sensitive to neutrons with energies in specific (different) regions of the slow neutron range by covering individual detectors with materials having different energy dependent neutron absorption characteristics (neutron filters). Appropriate materials for this application are cadminum (Cd), and gadolinium (Gd). Therefore, one of the three detectors is covered with Cd, the second is covered with Gd, and the third is used bare (unfiltered). Boron or samarium could be used in place of the gadolinium filter. This substitution, however, will result in lower sensitivity as will be shown in subsection 2.3.

Before describing the procedure for determining the formation parameters from the observed detector responses, a simple example amenable to manual computation is presented to demonstrate he validity of the approach. The number of neutrons, C_B, recorded by a bare (unfiltered) detector immersed in a neutron field is a convolution of the energy dependent neutron flux, $\Phi(E)$, at the detector position, and the energy dependent detector counting efficiency, $\epsilon(E)$. That is,

$$C_B = \int_0^{E_{max}} dE \cdot \Phi(E) \cdot \epsilon(E) \quad , \tag{4}$$

where E_{max} is the maximum kinetic energy of source neutrons. Similarly, the counts recorded by a filtered (gadolinium-, boron-, or samarium-covered) detector, C_F, are

$$C_F = \int_0^{E_{max}} dE \cdot \Phi(E) \cdot \epsilon(E) \cdot \tau_F(E, t_F), \tag{5}$$

where $\tau_F(E, t_F)$ = filter transmission for neutrons with energy E, and t_F = filter thickness. The filter transmission is determined primarily by the energy dependent neutron absorption cross section of the filter material and will be discussed further in subsection 2.2.3. The ratio of the filtered-to-bare detector responses is the quantity

$$R_o = \frac{C_F}{C_B} = \int_0^{E_{max}} dE \cdot \Phi(E) \cdot \epsilon(E) \cdot \tau_F(E, t_F) \Big/ \int_0^{E_{max}} dE \cdot \Phi(E) \cdot \epsilon(E) \quad , \quad (6)$$

which is effectively normalized to the same neutron density, n, Equation 1.

Substituting the expression for $\Phi(E)$, Equation 1, into the above equation,

$$R_o = \left\{ 2\pi n \cdot \left(\frac{2}{m_n}\right)^{1/2} \cdot (\pi k T_n)^{-3/2} \cdot \int_0^{E_{max}} dE \cdot E \cdot \exp(-E/kT_n) \cdot \tau_F(E, t_F) \cdot \epsilon(E) + \right.$$

$$\left. + C \cdot \int_0^{E_{max}} dE \cdot E^{-1} \cdot \tau_F(E, t_F) \cdot \epsilon(E) \right\} *$$

$$* \left\{ 2\pi n \cdot \left(\frac{2}{m_n}\right)^{1/2} \cdot (\pi k T_n)^{-3/2} \cdot \int_0^{E_{max}} dE \cdot E \cdot \exp(-E/kT_n) \cdot \epsilon(E) + \right.$$

$$\left. + C \int_0^{E_{max}} dE \cdot E^{-1} \cdot \epsilon(E) \right\}^{-1} \cdot \quad (7)$$

This shows that the temperature sensitivity of R_o is primarily determined by the Maxwellian component of the neutron flux. The effect of the 1/E (temperature independent) term as far as this quantity is concerned is that of an undesirable background. Correction of the filtered and bare detector responses for the 1/E contribution results in higher sensitivity of the above ratio to temperature changes (subsection 2.3.2). This correction is one of the functions of the cadmium-covered detector as will be discussed below. When the filtered and bare detector responses are corrected,

$$R = \int_0^{E_{max}} dE \cdot E \cdot \exp(-E/kT_n) \cdot \tau_F(E, t_F) \cdot \epsilon(E) \Big/ \int_0^{E_{max}} dE \cdot E \cdot \exp(-E/kT_n) \cdot \epsilon(E). \quad (8)$$

This expression provides a means for estimating the temperature gauge response sensitivity. An approximate, preliminary evaluation of the gauge response, R, can be obtained by computing the count (detector response) ratio using numerical techniques.

A rather simple case amenable to manual computation is considered realizing that the validity of the method is not confined to this example. The detector efficiency, ϵ (E), is assumed to vary inversely with the square root of the neutron energy which characterizes roughly many neutron detectors in general use. For convenience, the filter is assumed to be 0.0001 inch thick made of boron-10, and its transmission is calculated as will be described later. The calculated count ratio is plotted in Figure 3 as a function of the neutron moderator temperature which, for simplicity is assumed to be equal to the neutron temperature as is nearly the case in water. The values plotted in this figure have been normalized to the ratio at 250° C. The curve displays a linear dependence of the count ratio on temperature. The sensitivity inferred is, on the average, ~0.04 percent change in the ratio per °C change in the temperature in the range between 300°C and 350°C.

It must be emphasized at this point that this example is meant only as a demonstration of the validity of the technique and should by no means be considered an optimum system. In fact, the two-detector system is not sufficient to determine unambiguously the temperature of an arbitrary medium (formation). This would have been the case if the slow neutron spectrum depended only on the medium temperature. Then the measurements and simple analysis in the above example would suffice. The additional dependence of the neutron temperature on the formation neutron absorption cross section and moderating power requires at least three measurements, assuming that T, Σ_a, and $\xi\Sigma_s$ are independent parameters. This more complex system requires a more involved analysis, but it does indeed provide the means for the unambiguous determination of the temperature of an arbitrary formation and simultaneously its neutron absorption cross section and moderating power.

It has been the purpose of this study to optimize the system and demonstrate its ultimate feasibility. The remainder of this subsection discusses the response of the three-detector system and the analysis method to obtain the desired information. The remainder of the report presents further, more concrete evidence of the temperature gauge feasibility.

As previously noted, the present (optimum) system uses three detectors to obtain the three necessary measurements. One of these detectors is bare (unfiltered), the

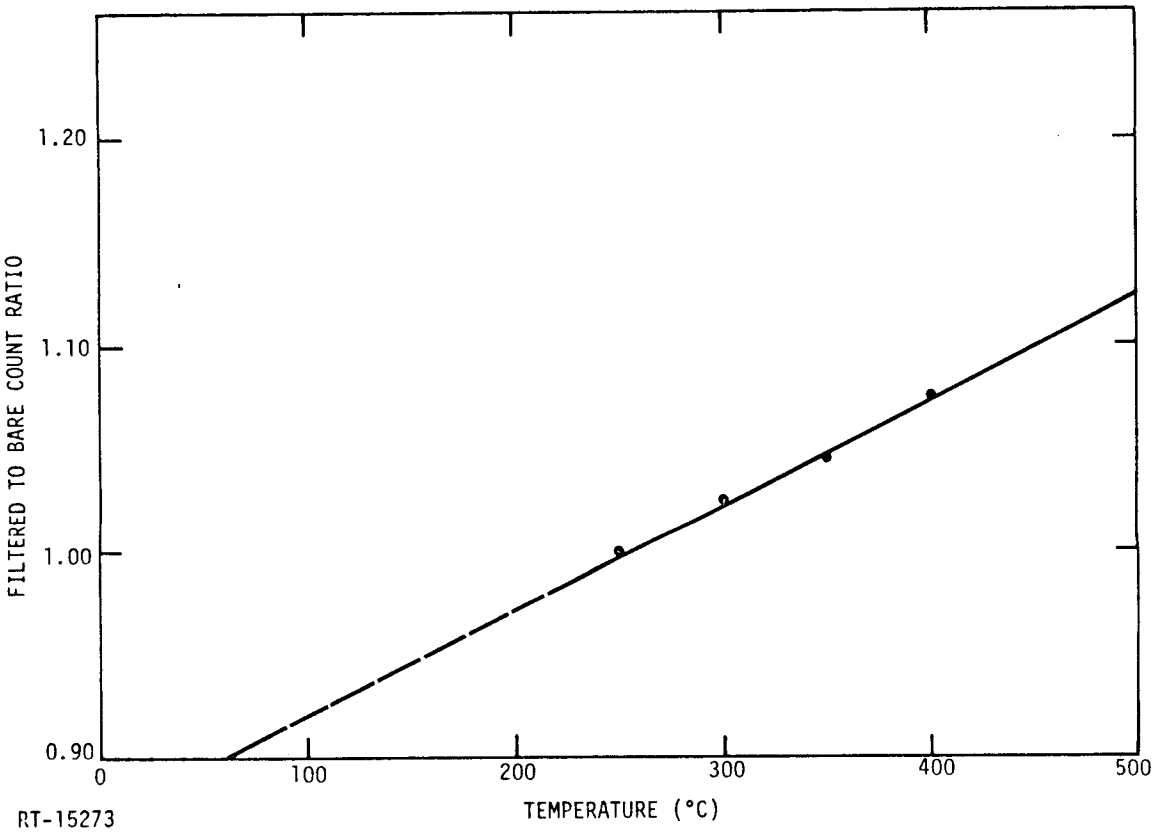

Figure 3. Preliminary calculation of the temperature gauge response assuming no 1/E contribution to the neutron detector response, $E^{-1/2}$ detector counting efficiency energy dependence, and a 0.0001-inch thick boron-10 filter. The sensitivity is 0.04 percent change in the count ratio per ^{o}C change in the temperature.

second is cadmium-covered, and the third is gadolinium-filtered. The Gd-filtered detector replaces the boron-filtered detector of the above example. The response (recorded counts) of the bare detector, C_B, is expressed by Equation 4. Similarly, the counts recorded by Gd-filtered and Cd-covered detectors are given by Equation 5 with the corresponding filter transmission function substituted for τ_F. Therefore,

$$C_{Gd} = \int_0^{E_{max}} dE \cdot \Phi(E) \cdot \epsilon(E) \cdot \tau_{Gd}\ (E, t_{Gd}) \ , \qquad (9)$$

where $\tau_{Gd}(E,t_{Gd})$ = Gd filter transmission function, and t_{Gd} = Gd filter thickness, while the Cd-covered detector counts are

$$C_{Cd} = \int_0^{E_{max}} dE \cdot \Phi(E) \cdot \epsilon(E) \cdot \tau_{Cd}\ (E, t_{Cd}) \ , \qquad (10)$$

where $\tau_{Cd}(E,\ t_{Cd})$ = Cd cover transmission function, and t_{Cd} = Cd cover thickness. Suitable filter thicknesses used in the present work are t_{Gd} = 2 mils (0.005 cm) and t_{Cd} = 30 mils (0.076 cm).

The Cd-covered transmission is characterized by a sharp cutoff at 0.4 eV (subsection 2.2.3). Therefore, the cadmium-covered detector is sensitive to neutrons with energies in the epithermal, slowing-down region (Figure 1) except at very high formation temperatures, i.e., $>1000^{o}$C. Since the number of neutrons in this part of the spectrum, i.e., the constant C in Equation 1, depends only on the neutron moderating properties of the formation, the response of the Cd-covered detector provides a measure of the moderating power, $\xi\Sigma_s$.

Similarly, the Gd-filter transmission has a rather broad cutoff at $\sim$0.03 eV (subsection 2.2.3). Thus, the gadolinium filtered detector is sensitive to neutrons with energies in part of the thermal component of the slow neutron spectrum (primarily the region above $\sim$0.03 eV, Figure 1) as well as in the slowing-down, epithermal, region. Since the fraction of the neutrons in the thermal region accessible to the Gd-filtered detector depends on the neutron temperature, T_n, the response of this detector provides a measure of this parameter.

The bare (unfiltered) detector is sensitive to all slow neutrons, i.e., neutrons with energies in both the thermal and epithermal spectral regions. All else being equal, the number of slow neutrons (regardless of energy) depends on the absorption cross section of the moderating medium (formation) (Ref 5). Therefore, the bare detector response provides essentially, a measure of the neutron absorption cross section.

According to the above discussion,

$$C_B = C_B^{th} + C_B^{ep} \quad , \tag{11}$$

and

$$C_{Gd} = C_{Gd}^{th} + C_{Gd}^{ep} \quad , \tag{12}$$

where the superscripts "th" and "ep" denote the thermal and epithermal components, respectively. Since,

$$C_B^{ep} = C \int_{E_o}^{E_{max}} dE \cdot E^{-1} \cdot \epsilon(E), \tag{13}$$

and

$$C_{Gd}^{ep} = C \int_{E_o}^{E_{max}} dE \cdot E^{-1} \cdot \epsilon(E) \cdot \tau_{Gd}(E, t_{Gd}) \quad , \tag{14}$$

where E_o is the low energy cutoff of the slowing-down region ($E_o \sim 0.15$ eV), C_B^{ep} and C_{Gd}^{ep} are independent of the formation temperature and as such they constitute backgrounds for the respective measurements. However, C_B^{ep} and C_{Gd}^{ep} can be determined from C_{Cd}, and C_B^{th} and C_{Gd}^{th} can be obtained using Equations 11 and 12, respectively.

Since T_n is determined by T, Σ_a, and $\xi\Sigma_s$, Equation 2, and C_{Gd}^{th} is a measure of the neutron temperature,

$$C_{Gd}^{th} = f(T, \Sigma_a, \xi\Sigma_s) \quad , \tag{15}$$

or

$$C_{Gd}^{th} \Big/ C_B^{th} = g(T, \Sigma_a, \xi\Sigma_s) \quad , \tag{15a}$$

and on the basis of the above discussion,

$$C_{Gd}^{th} = f'(T, C_B^{th}, C_{Cd}) \ , \tag{16}$$

or

$$C_{Gd}^{th} \Big/ C_B^{th} = g'(T, C_B^{th}, C_{Cd}) \ . \tag{16a}$$

As in the above example, the advantage of the ratio ($R = C_{Gd}^{th} \Big/ C_B^{th}$) is that this quantity is normalized to the same neutron density, Equation 1. A cross plot of the corrected detector responses (C_{Gd}^{th}, C_B^{th}, and C_{Cd}, or R, C_B^{th}, and C_{Cd}) obtained for various values of the formation temperature, neutron absorption cross section, and moderating power along three orthogonal axes constitutes a three dimensional map. Each point on this map is determined by the responses of the three detectors and it corresponds to the unique set of conditions under which these responses were obtained. That is, each point on this mapping corresponds to a unique value of the temperature and each of the neutron properties of the formation.

Calibration of the formation temperature sensor consists of a mapping of the corrected responses of the three detectors obtained in well characterized test formations at accurately known temperatures. The temperature of an arbitrary formation is determined simply by obtaining the sensor (three-detector) response, and locating the corresponding point in the calibration space. The temperature of the arbitrary formation is the temperature which corresponds to that particular calibration point. Since the correspondence is unique, the temperature determination by this noncontact method is unambiguous. Furthermore, the values of the neutron absorption cross section and the neutron moderating power (formation saturated porosity) are obtained simultaneously. Experimental evidence demonstrating the feasibility of the technique is presented in subsection 2.4.

2.2 FORMATION TEMPERATURE GAUGE

Characteristics of the various formation temperature sensor components are discussed in this section. The neutron source is discussed in subsection 2.2.1, and the neutron detector characteristics are presented in subsection 2.2.2. The essential properties of various filter materials are discussed in subsection 2.2.3.

2.2.1 Cf-252 Source Characteristics

There are currently several types of portable neutron sources in general use. These consist of isotopic neutron sources based on (α,n) reactions (reactions involving the absorption of α-particles and the subsequent emission of neutrons), sealed-beam neutron generators, and isotopic spontaneous fission sources. (α,n) reaction-based sources which include americium-beryllium, plutonium-beryllium, and radium-beryllium among others have relatively low specific activity which limits their minimum physical size. Similarly, portable neutron generators used primarily in oil well logging to determine formation porosity and neutron absorption properties are intensity limited. More intense, small-size neutron generators are currently being developed for mineral exploration applications, but these programs are not addressing the high temperature problems. The most immediately applicable neutron source for high temperature use is Cf-252 which produces neutrons through spontaneous fission. This source is physically small, and it is available in strengths yielding from less than 10^6 neutrons per second to greater than 10^{10} neutrons per second. Moreover, the standard SR-Cf-100 encapsulation has been tested successfully for integrity to 900°C. The current concept for the determination of formation temperatures makes use of a Cf-252 source.

Cf-252 decays by α-particle emission 97 percent of the time. The remaining three percent of the time it undergoes spontaneous fission. This fission rate results in the emission of 2.4×10^{12} neutrons per second per gram of this isotope. Spontaneous fission of Cf-252 results in the emission of neutrons with the energy distribution shown in Figure 4 (Ref 6) which is nearly identical to the fission neutron spectrum in a nuclear reactor. A relatively small number of neutrons are emitted in (α,n) reactions involving α-particles produced by the decay of Cf-252 and light nuclei produced by fission. In addition to the neutrons, gamma radiation is also emitted by a Cf-252 source. As shown in Figure 5, this consists of contributions from the α-decay of californium, fission, and the decay of the fission products (Ref 6). Although no β-radiation results from the decay of Cf-252 itself, β-particles are emitted as a result of fission product decay. Like the α-particles, however, this radiation is easily absorbed in materials surrounding the source. Consequently, for all practical purposes only gamma and neutron radiation is emitted by encapsulated Cf-252 sources.

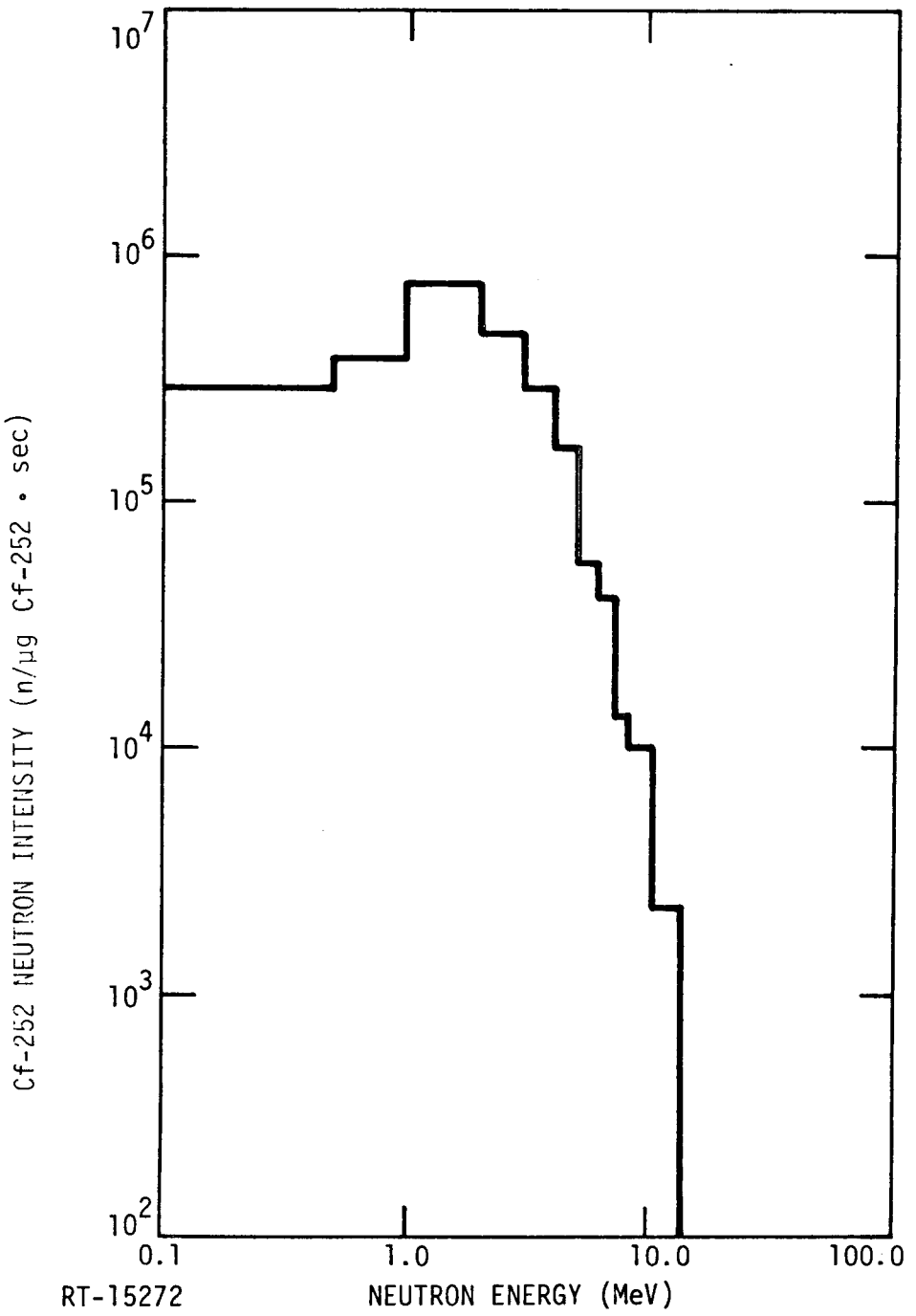

Figure 4. Californium-252 fission neutron spectrum (Ref 6)

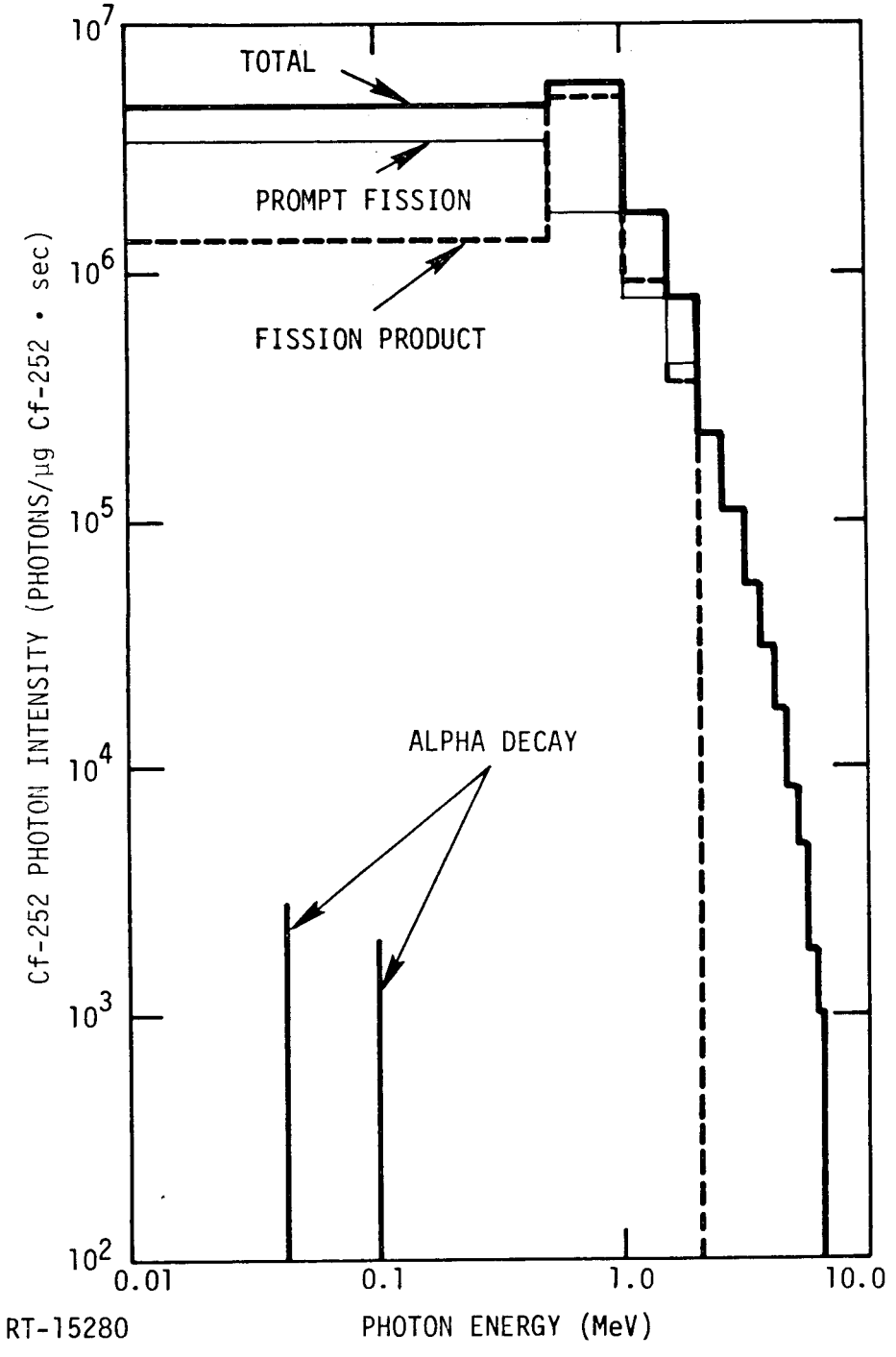

Figure 5. **Californium-252 gamma spectrum. The various components of the spectrum shown are described in the text (Ref 6).**

2.2.2 Neutron Detectors

There are several factors which must be considered in selecting a neutron detector for the present study. The most important of these is the detector characteristics. These include primarily its thermal neutron counting efficiency, its operating temperature range, and its sensitivity to background gamma radiation. Another factor is the availability of the various neutron detectors. The final consideration is the applicability of the detector selected for the feasibility study beyond the phase of concept development to the development of a prototype instrument.

The most widely used and apparently most highly developed neutron detectors are gas-filled proportional counters. These are tubes filled with gases containing neutron absorbing elements. Another type of neutron detector currently in use is the scintillation detector. In this case, the neutron absorbing element is contained in a scintillating material (crystal or liquid phosphor). Such devices would require cooling even at intermediate temperatures ($\sim 150^{\circ}C$) encountered in geothermal environments. Another important disadvantage of these detectors is their high sensitivity to gamma radiation rendering their operation inappropriate in the presence of even moderate gamma fields. Certain kinds of gas-filled counters, on the other hand, are currently used to monitor fluxes in high temperature regions inside nuclear reactors. Such detectors are operable at temperatures up to $760^{\circ}C$ without cooling. Furthermore, gas-filled counters are generally very insensitive to gamma rays even in very intense fields.

The major components of a thermal-neutron gas-filled proportional detector are the neutron sensitive element and the fill gas. The neutron sensitive element is an isotope with high affinity for thermal neutron absorption, i.e., high thermal neutron absorption cross section. It can be part of the fill gas as boron-10 in BF_3 filled counters and helium-3 in He-3 filled detectors, or it may be plated on the counter walls as boron-10 in boron-lined detectors and uranium-235 in fission detectors. Neutron absorption by the neutron sensitive elements results in the release of various charged particles in the detector chamber occupied by the fill gas. These charged particles traverse the chamber volume in directions defined by an applied electric field causing ionization of the fill gas. The induced ions and electrons are collected by the field electrodes resulting in a charge pulse at the detector output for each neutron absorbed in the sensitive volume of the detector.

The various types of gas filled thermal neutron detectors are distinguished by the kind of fill gas and the kind and form (gaseous or plated) of the active element used. The general design characteristics obviously determine the general operational detector characteristics. The type and abundance (fill gas pressure or plate thickness) of the neutron sensitive isotope used, together with the detector chamber goemetry, structural design, and fill gas pressure determine the counting efficiency. The fill gas ionization characteristics determine the pulse shape, and, hence, the detector resolution. The general insensitivity of these devices to gamma radiation is a result of the low density of the fill gas even at high fill gas pressures. The low density results in relatively low ionization of the fill gas by gamma rays.

Of the various gas filled neutron detectors available, the He-3 counters are the most efficient followed in order of decreasing counting efficiency by BF_3 filled, B–10 lined, and U-235 lined detectors. The rating in terms of sensitivity to gamma radiation is exactly the same with He-3 filled detectors being the most sensitive and the U–235 fission chambers being the least sensitive. Even the most sensitive He-3 detectors, however, are relatively insensitive to gamma radiation and they have been operated satisfactorily in the presence of moderately high gamma fluxes. Standard He-3 filled detectors used in oil well logging can be used at temperatures up to 200°C. The operating temperature limit of standard BF_3 filled counters is 100°C although special design has extended this limit to 150°C. Standard B-10 lined detectors are limited to operation at temperatures at or below 150°C, while specially designed devices are operable up to 300°C. U-235 fission chambers are operable at temperatures above the operating range of other gas filled neutron detectors. Standard devices are operable up to 300°C, while specially designed detectors have been operated at 760°C (Ref 7).

He-3 filled neutron detectors were selected for use in the present feasibility study of the formation temperature gauge for various reasons. He-3 filled detectors are the most efficient of the gas filled proportional neutron counters. The specific detectors selected for use in this study are Reuter-Stokes P4-0410-204 and P4-0404-207 counters. These are one-half-inch diameter by 12-inches and six-inches, respectively, long cylinders filled with He-3 gas at 20 atmospheres pressure. The sensitive region of these detectors is ten-inches and four-inches long, respectively. The counting efficiencies of these detectors and similar He-3 counters filled at five atmospheres pressure have been calculated and are shown in Figure 6. It is readily seen that the counting efficiency of these detectors is high for thermal neutrons but it decreases rather rapidly as the neutron energy increases beyond the thermal range. The calculated counting efficiency

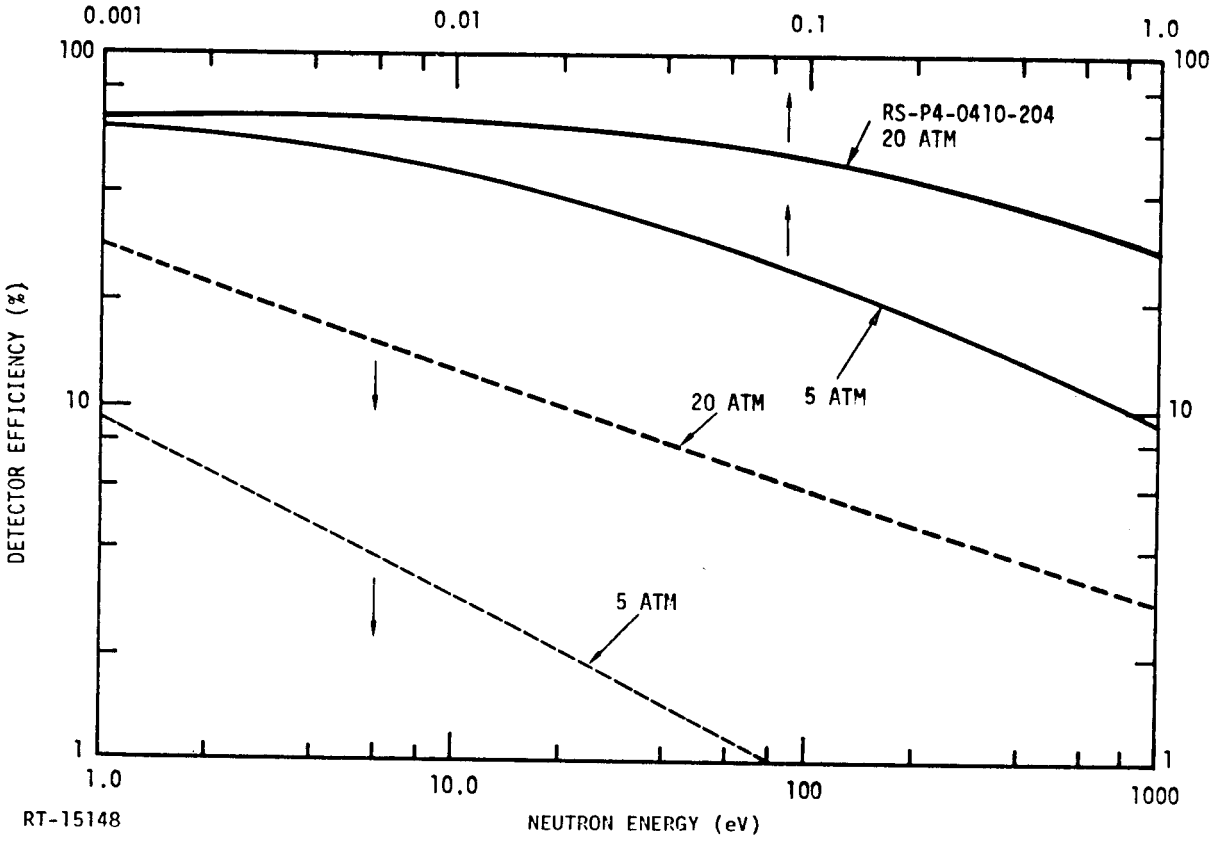

Figure 6. Calculated detector efficiency of He-3 filled proportional counters. The solid curves represent the efficiencies at the lower energies, 0.001 to 1.0 eV, while the dashed curves are their corresponding extensions in the energy range from 1.0 to 1000 eV.

curves have been used in the computational study of the formation temperature gauge response (Equation 6) which will be discussed in subsection 2.3. In addition to high neutron counting efficiency, the above detectors are sufficiently insensitive to gamma rays. The anticipated background gamma radiation due to gamma emission by the Cf-252 source and by formation elements subsequent to neutron activation will not affect significantly the operation of these detectors. Furthermore, the operating temperature range of the detector chosen is sufficiently high for the purposes of the present experimental feasibility study, i.e., $\leqslant 200^{\circ}C$ for the 12-inch long detector and $\leqslant 260^{\circ}C$ for the six-inch long counter.

Regarding the applicability of the above detectors beyond the technique feasibility phase, it should be noted that RS-P4-0410-204 detectors have been used in oil well logging tools. Their operating characteristics in logging operations have been established within their present operating temperature range. Since the operating temperature range is limited by structural design considerations, it is possible that the $260^{\circ}C$ upper limit can be extended, perhaps to or beyond the $325^{\circ}C$ DGE short-range goal, by special design. If the high operating temperature limit cannot be extended by advanced design, He-3 detectors may still be used in a geothermal well logging tool provided that they are cooled to temperatures somewhat below $260^{\circ}C$. This may prove to be not a very difficult task. Assuming that cooling the detector proves to be inconvenient or inappropriate, then a B-10 lined detector operable at temperatures up to $300^{\circ}C$ may be used instead of the He-3 filled counter. It is expected that the qualitative conclusions of this study will still be valid.

2.2.3 Filter Materials

The neutron filter, i.e., a material with selective (energy dependent) neutron absorption (or transmission) properties, is one of the critical, if not the most important component of the formation temperature gauge. Therefore, care has been taken to select the most suitable element. An ideal filter material would be one which absorbs practically all neutrons with energies lower than ~ 0.03 eV (see Figure 1), but none of the neutrons with energies higher than this cutoff. Such a material would have to have a very high-neutron absorption cross section below the cutoff energy, and very low or zero cross section above it. Unfortunately, such an ideal material does not exist.

Therefore, the first criterion in selecting a suitable neutron filter for the temperature gauge is that its neutron absorption (transmission) characteristics approximate as closely as possible those of the ideal.

A search revealed several promising materials. These can be categorized as 1/v absorbers and low-energy resonance absorbers. The first category includes elements whose thermal neutron absorption cross section varies inversely with the neutron velocity (or inversely with the square root of the neutron kinetic energy) and is exemplified by boron-10 (B-10) and lithium-6 (Li-6). The second category includes elements with resonances (peaks) in their thermal absorption cross section. Such elements include cadmium (Cd), lutetium (Lu), samarium (Sm), xenon-135 (Xe-135), and gadolinium (Gd) with resonances at 0.173, 0.142, 0.095, 0.082, and 0.03 eV, respectively.

Further considerations in the filter selection process include nuclear stability of the above elements, availability, and radiation emission subsequent to neutron absorption. On the basis of these and the above criterion, the filter choice was narrowed down to B, Sm, and Gd. Neutron transmission curves were computed for these materials using the expression

$$\tau_F(E,t_F) = \exp\left[-\Sigma_a(E) \cdot t_F\right] \quad , \tag{17}$$

where $\Sigma_a(E)$ is the neutron absorption cross section for neutrons with kinetic energy E, and the remaining variables are the same as in Equation 5. The computed transmission curves are shown in Figure 7. The ultimate criterion for the selection of the most suitable filter is the temperature gauge sensitivity or rate of variation of the filtered-to-bare detector count ratio with temperature, Equation 6, obtained when each of the three filters is used. This selection has been made on the basis of calculations described in the next section.

The neutron transmission function of the cadmium cover, $\tau_{Cd}(E, t_{Cd})$, was also computed for t_{Cd} = 0.03 inches (0.076 cm). This curve is presented in Figure 8. As noted previously, this function has a rather sharp cutoff at 0.4 eV.

2.3 COMPUTATIONAL STUDY OF THE TEMPERATURE GAUGE RESPONSE

As is generally the case with the study of a new concept, the purpose of the present computational analysis was two-fold. First, it was the purpose of the calculations to be described in this section to establish the soundness of the formation

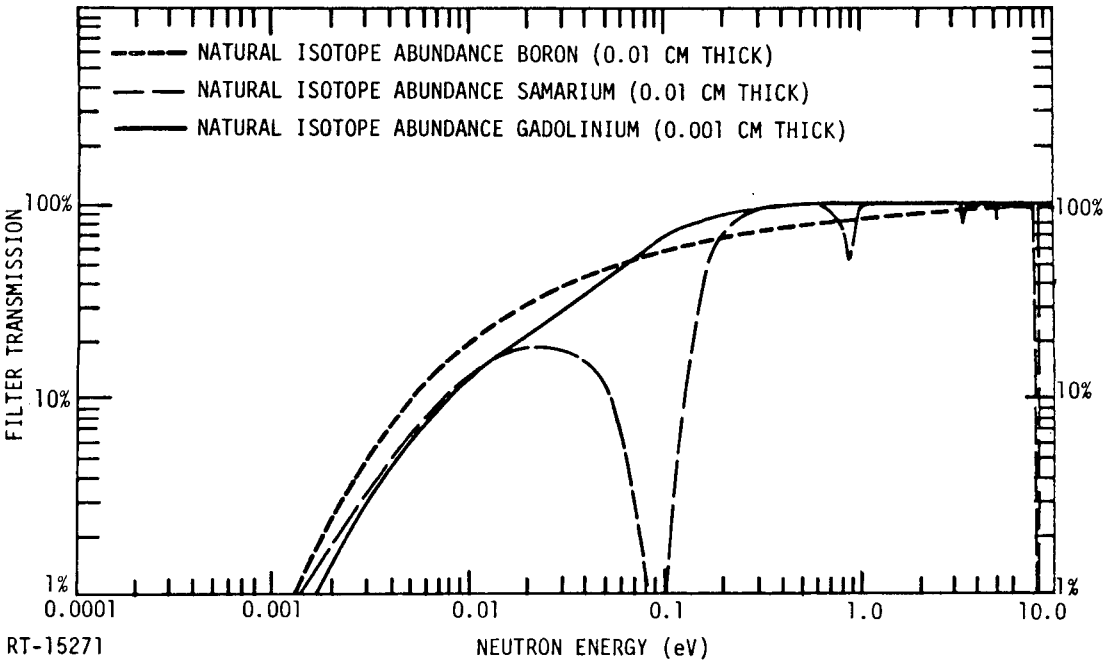

Figure 7. Calculated transmission functions for boron, samarium, and gadolinium filters. The corresponding filter thicknesses are given. In each case, the isotopic abundance of the filter material is that which is found in the natural composition of the element.

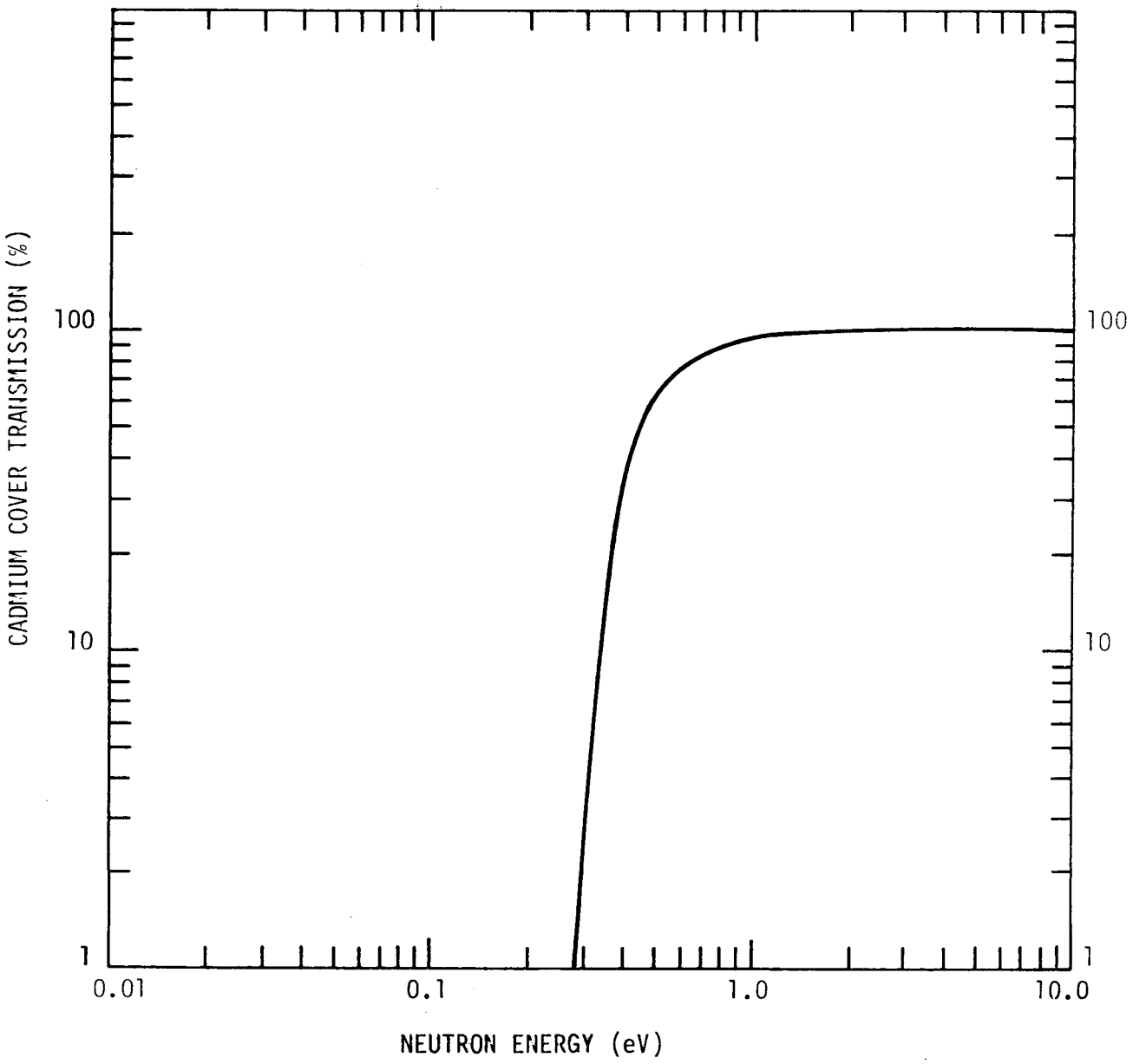

Figure 8. **Calculated transmission function for cadmium. The cover thickness is 0.03 inches (0.076 cm).**

temperature gauge concept and in so doing, to determine whether or not an experimental study of the technique would be warranted. Having established the applicability of method, the results of the calculations determined suitable detector and filter combinations and served as a starting point for optimization experiments.

It is extremely difficult and very costly to perform the necessary calculations for situations corresponding exactly to the experimental arrangement in terms of geometric and compositional details. Since the above stated aims of the computational study can be fulfilled by performing approximate (simplified model) calculations, elaborate calculations were not warranted. The computations described in the following paragraphs were based on a simplified model. Although they serve the purposes stated above, their results are rather approximate. For this reason, it is not, nor has it ever been, our intention to use the results of the present computational study as a calibration of the temperature gauge response. As previously stated, the instrument calibration curves will be generated experimentally.

2.3.1 Computational Model

As noted in subsection 2.1, the neutron temperature (which characterizes the Maxwellian component of the slow neutron spectrum) is determined in part by the moderator temperature (Equation 2). In fact, in the case of an infinite medium with a uniformly distributed fast neutron source, T_n is directly proportional to the medium temperature, T, the proportionality constant depending simply on the formation neutron properties (Equation 3). In order to determine the proportionality between the neutron and moderator temperatures for materials to be used in this study, and to check the validity of assumptions made regarding the nature of the thermal neutron energy distributions, fluxes were computed at various temperatures of the moderator using essentially a very simple transport code. The particular computer program used is the GGC code developed at General Atomic (Ref 8). It considers a monoenergetic, fast-neutron source uniformly distributed in the moderating medium. To avoid the complexity inherent in finite geometry computations of this kind, the code also assumes an infinite medium. The thermal neutron flux resulting from the slowing down of source neutrons is computed using well established, standard nuclear reactor physics techniques, and the most recent nuclear cross-section data.

To test the validity of our assumptions regarding the shape of the thermal neutron energy distributions, Equation 1, thermal neutron fluxes were calculated in an infinite

water moderator at various temperatures in the range of interest (300°K to 600°K, or from about room temperature to 327°C). The results of this set of calculations verified our assumptions. The calculations indicate that Equation 1 is completely valid for a water moderator. Furthermore, they show that in water the neutron temperature, T_n, is approximately equal to the moderator temperature, T, i.e., the proportionality between the two quantities, Equation 3, is nearly one. This is shown in Figure 9 which is a comparison between the GGC-calculated flux in water at 300°K (27°C) and a Maxwellian functions with $T_n = 300$. The agreement is just as good at the various other temperatures at which similar comparisons were made. The constant C to be used in Equation 1 can be determined from the high-energy region of the GGC-calculated flux. For water $C \sim 4125 \cdot n$ (neutrons/$cm^2 \cdot$ sec).

Similar computer calculations of the thermal neutron flux were performed for moderators consisting of various mixtures of silica sand (SiO_2) and water at 300°K. As in the case of the pure water moderator, this set of calculations verifies the assumed functional dependence of the thermal neutron flux on the neutron energy, Equation 1. In this case, however, the neutron temperature, T_n, is not the same as the temperature of the moderator, T. The proportionality constant is shown graphically in Figure 10 as a function of the water content of the $SiO_2 \cdot H_2O$ mixture. The points represent the neutron temperatures inferred from the GGC-calculated thermal neutron fluxes and the error bars represent the corresponding uncertainties. The solid line is a plot of the expression reported by J. A. Czubek in Reference 9. This expression is equivalent to Equation 3. The dashed curve represents the same equation with a rather small adjustment of the empirical constant in Czubek's expression, contained in 0.02687, whose value is "questionable". The adjusted expression fits the neutron temperatures inferred from the GGC-flux calculation very well, thus establishing the validity of Equation 3, and the relation between T_n and T for various $SiO_2 \cdot H_2O$ mixtures.

The assumptions of an infinite medium and a uniformly distributed (infinite) fast-neutron source made to simplify the computations may appear to be limiting at first. This is not the case, however, since the slow neutron spectra calculated under the above assumptions are only slightly different from those produced by a point source in an effectively infinite medium, but at points sufficiently removed from the source (Ref 10). The minimum distance from the neutron source beyond which the point and uniformly distributed sources yield approximately the same spectra depends on the moderating medium neutron properties, and it is a minimum for water.

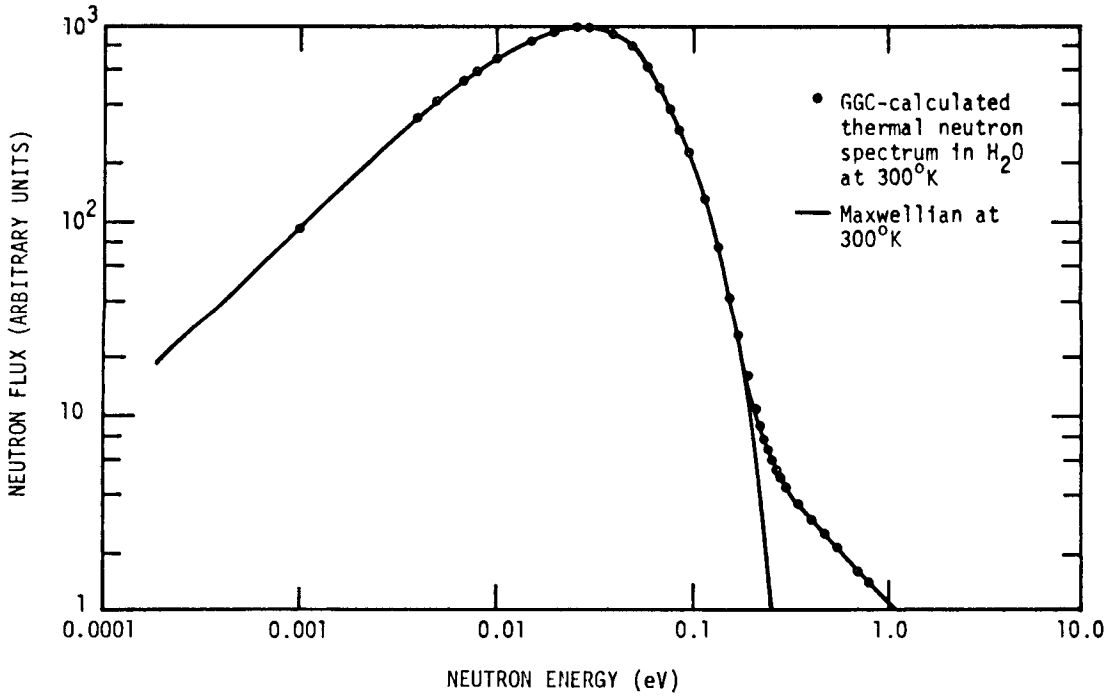

Figure 9. Comparison between the transport-calculated (GGC) thermal neutron flux in water at 300°K and the corresponding Maxwellian function, i.e., the first term of Equation 1, with T_n = 300°K.

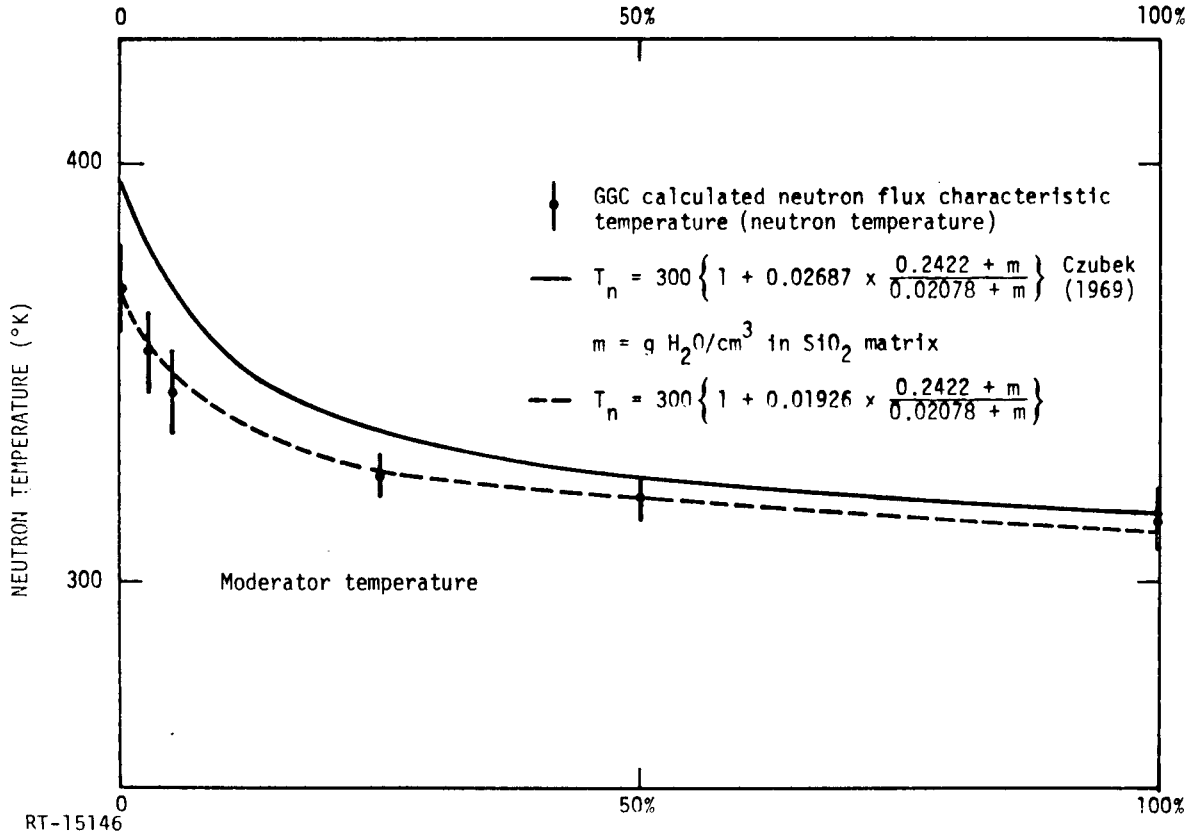

Figure 10. Variation of the apparent formation temperature, T_n, of 17 percent porous quartz formation with various degrees of water saturation. The neutron temperatures inferred from the GGC-calculated spectra (data points) are compared with the expression of Czubek (Ref 9) (solid curve). The dashed curve represents a least squares fit to the data by a similar expression by varying the empirical constant (implicit in 0.02687).

2.3.2 Calculation of the Filtered-to-Bare Detector Count Ratio

In order to minimize the complexity of the problem and to make comparison between calculation and experiment as direct as possible, the filtered-to-bare detector count ratios, Equation 6, were computed for an infinite water medium. This approach avoids finite geometry problems, thus keeping the calculations as simple as possible, and takes advantage of the near equality between the neutron and moderator temperatures. The results of these calculations will be compared with measurements of the corresponding ratios in water, the geometry of the experiment being such as to approximate as closely as practicable the computational situation. Such a comparison will result in a basic understanding of the gauge response which is essential prior to its application in the complex geometry approximating closely the geothermal well environment.

The temperature gauge response, i.e., the filtered-to-bare detector count ratio as a function of temperature, has been calculated according to Equation 6. The necessary integrals, Equations 4 and 5, were evaluated on a computer by numerical integration. Count ratios, R, were computed at moderator (water) temperatures from $300^{o}K$ ($27^{o}C$) to $600^{o}K$ ($327^{o}C$). The thermal neutron fluxes, $\Phi(E)$, used in the calculations were computed according to Equation 1 with the value of the constant C extracted from the GGC-calculated fluxes. Most of the calculations were performed using the calculated counting efficiency of the RS-P4-0410-204 He-3 detector shown in Figure 6, although a limited number of calculations were also performed for comparison using the efficiency curve of the five atmosphere fill gas pressure detector. The transmission functions of boron, samarium, and gadolinium filters computed according to Equation 17 were used to determine the most suitable filter.

The computed count ratios appropriate to the RS-P4-0410-204 He-3 filled detector and to boron, samarium, and gadolinium filters of various thicknesses are shown in Figures 11, 12 and 13, respectively. It should be pointed out that the computed ratios contain the contribution from the slowing down part of the slow neutron spectrum. The technique sensitivities corresponding to the various filters and filter thicknesses are more readily compared when the corresponding gauge responses are normalized to the count ratio values at one temperature. Therefore, the same sets of curves normalized to the corresponding count ratio values at $27^{o}C$ ($300^{o}K$) are shown in Figures 14, 15 and 16, respectively. The normalized curves for each of the three filters show that use of the thicker filters results in higher gauge sensitivity. The higher sensitivity,

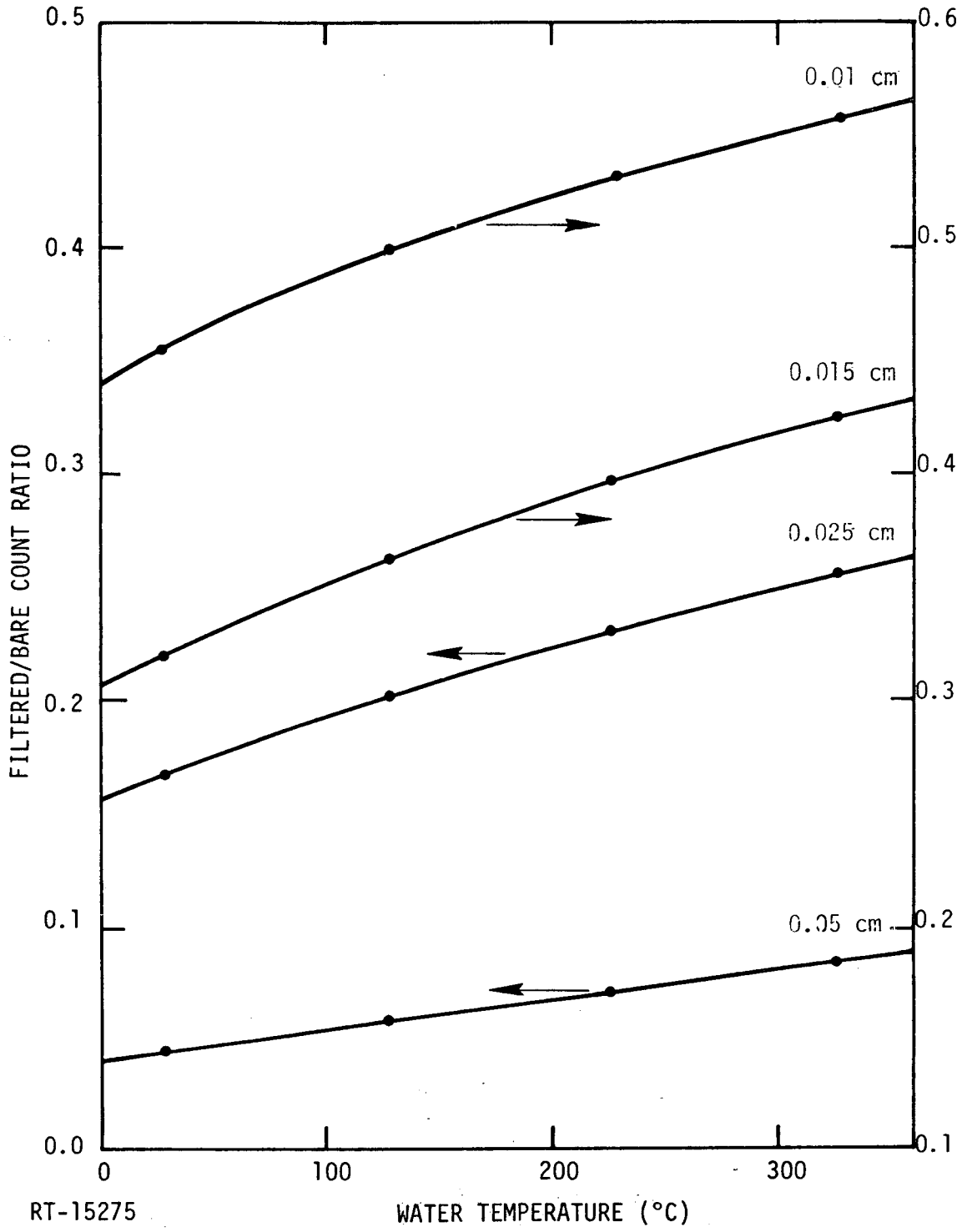

Figure 11. Calculated formation temperature gauge response, Equation 6, in water using a RS-P4-0410-204 He-3 filled detector, and natural isotope abundance boron filters of various thicknesses.

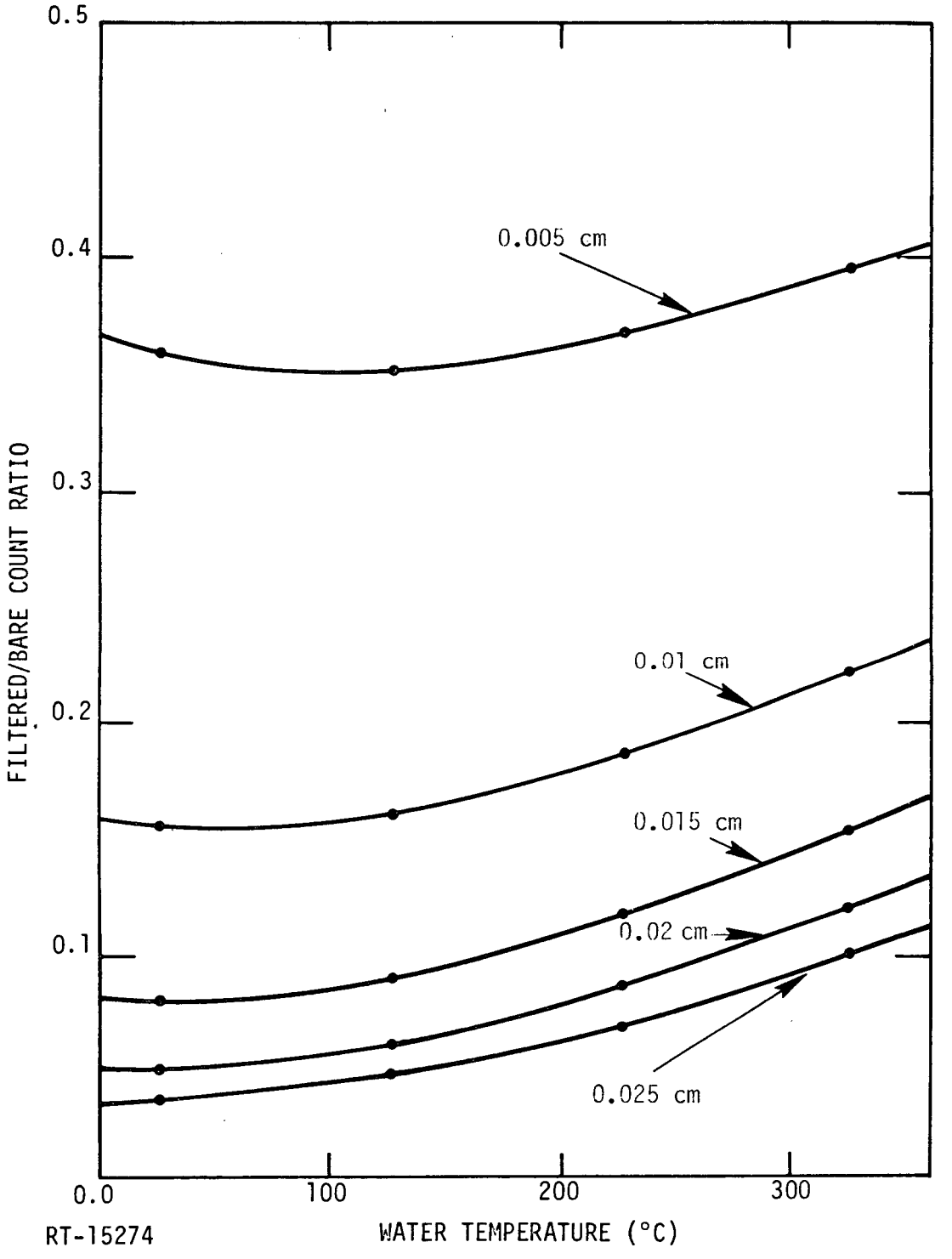

Figure 12. Calculated formation temperature gauge response, Equation 6, in water using a RS-P4-0410-204 He-3 filled detector, and natural isotope abundance samarium filters of various thicknesses.

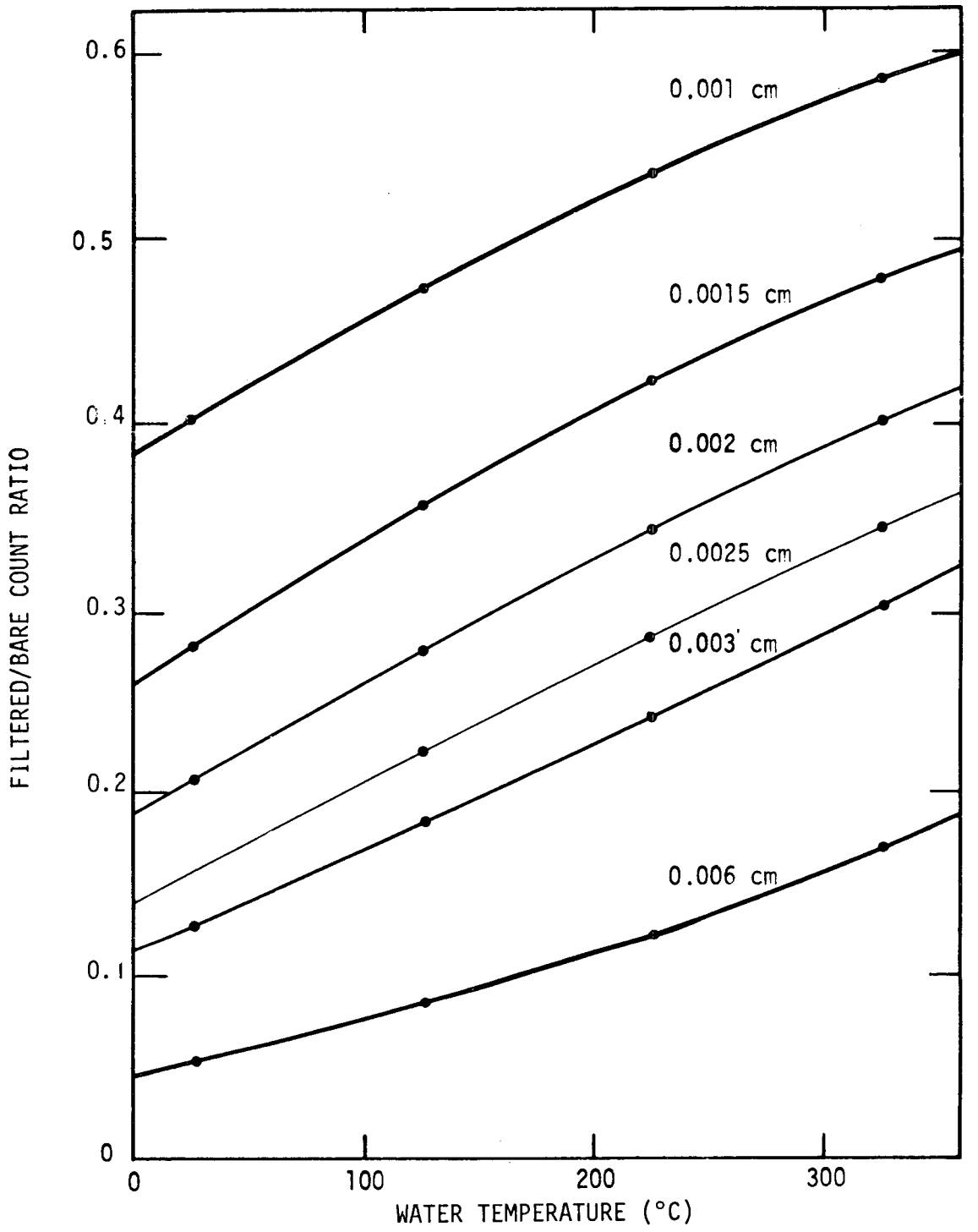

Figure 13. Calculated formation temperature gauge response, Equation 6, in water using a RS-P4-0410-204 He-3 filled detector, and natural isotope abundance gadolinium filters of various thicknesses.

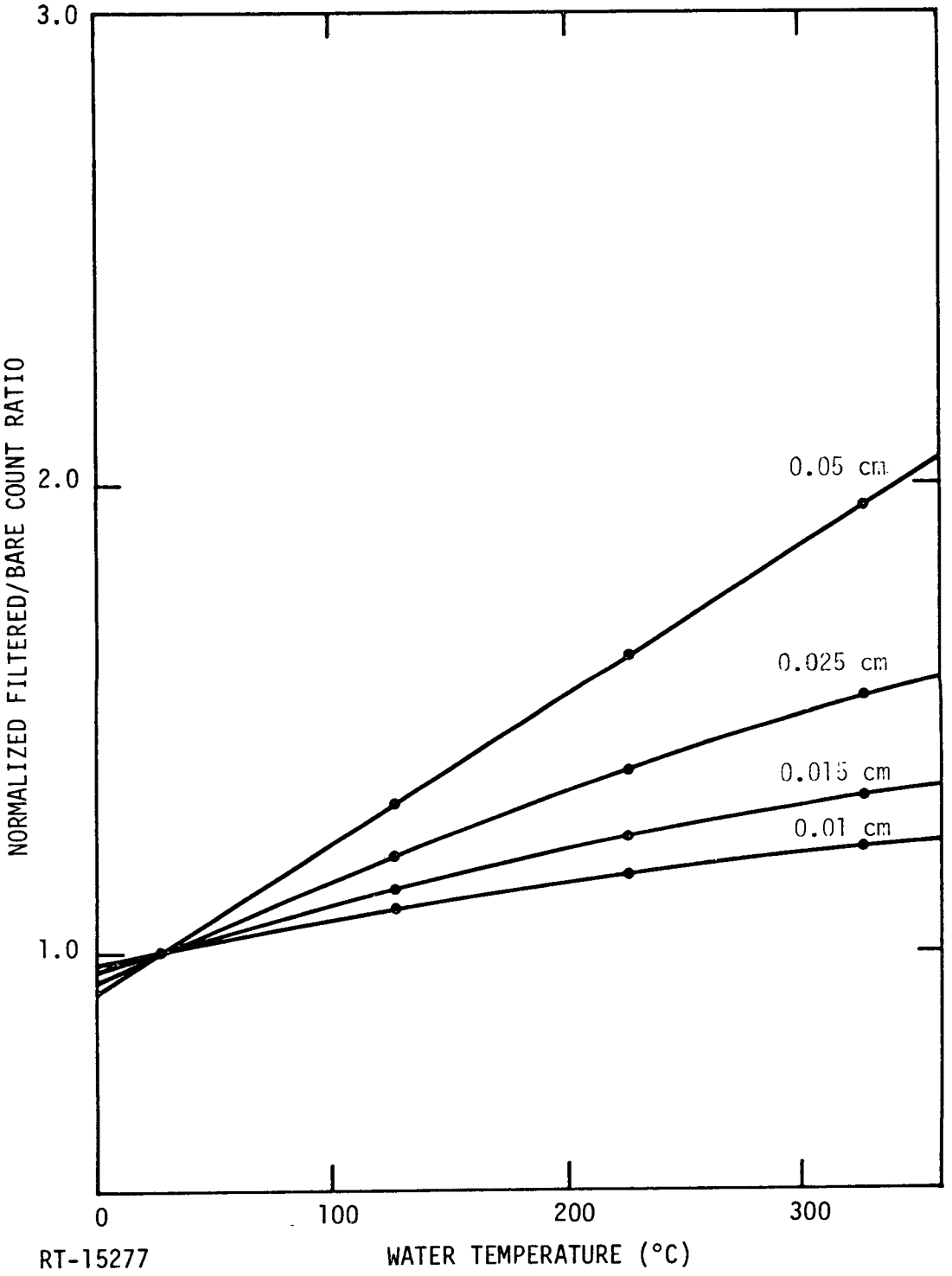

Figure 14. Calculated formation temperature gauge response, Equation 6, in water using a RS-P4-0410-204 He-3 filled detector, and natural isotope abundance boron filters of various thicknesses. These curves have been normalized to the corresponding count ratio values at 27°C.

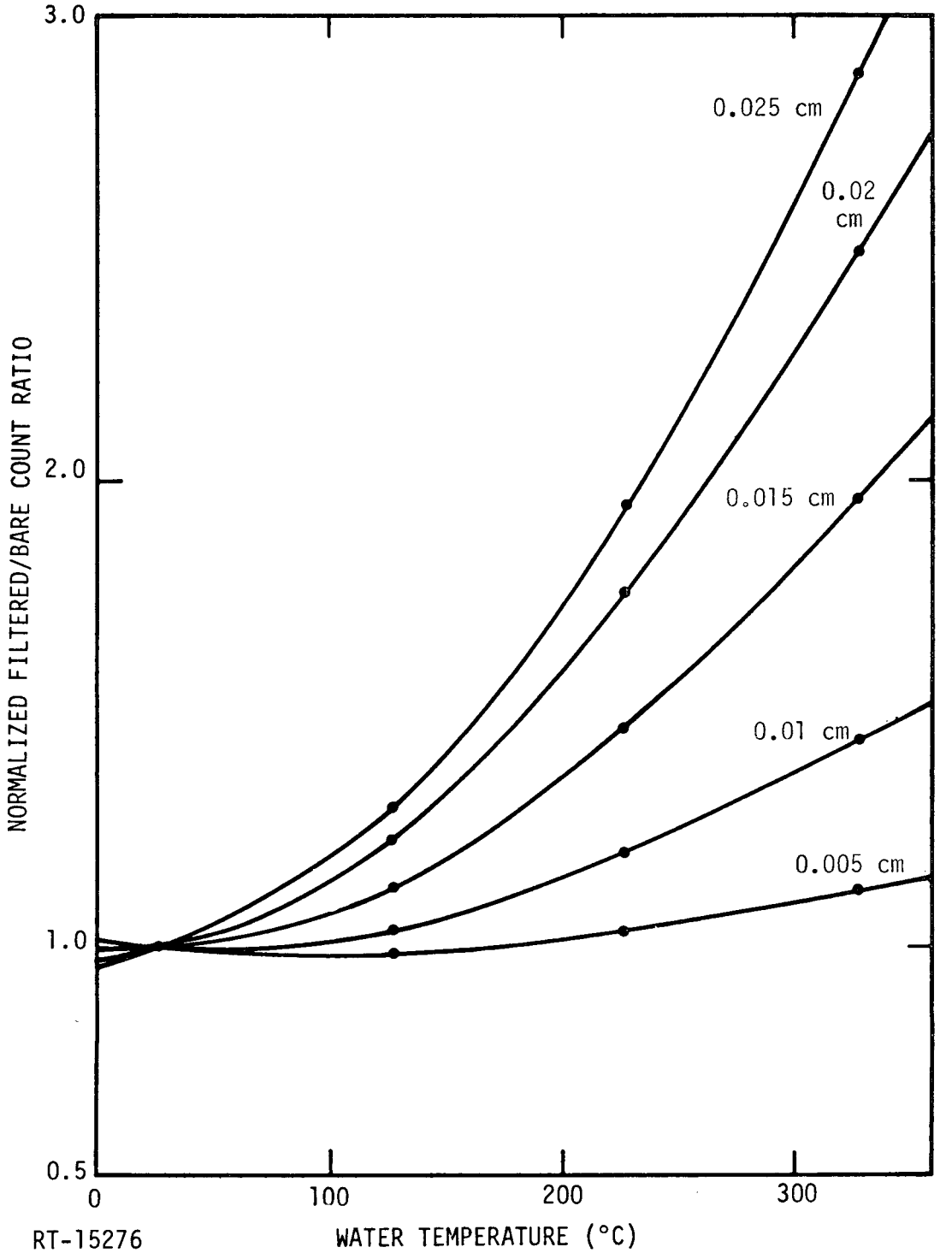

Figure 15. Calculated formation temperature gauge response, Equation 6, in water using a RS-P4-0410-204 He-3 filled detector, and natural isotope abundance samarium filters of various thicknesses. These curves have been normalized to the corresponding count ratio values at 27°C.

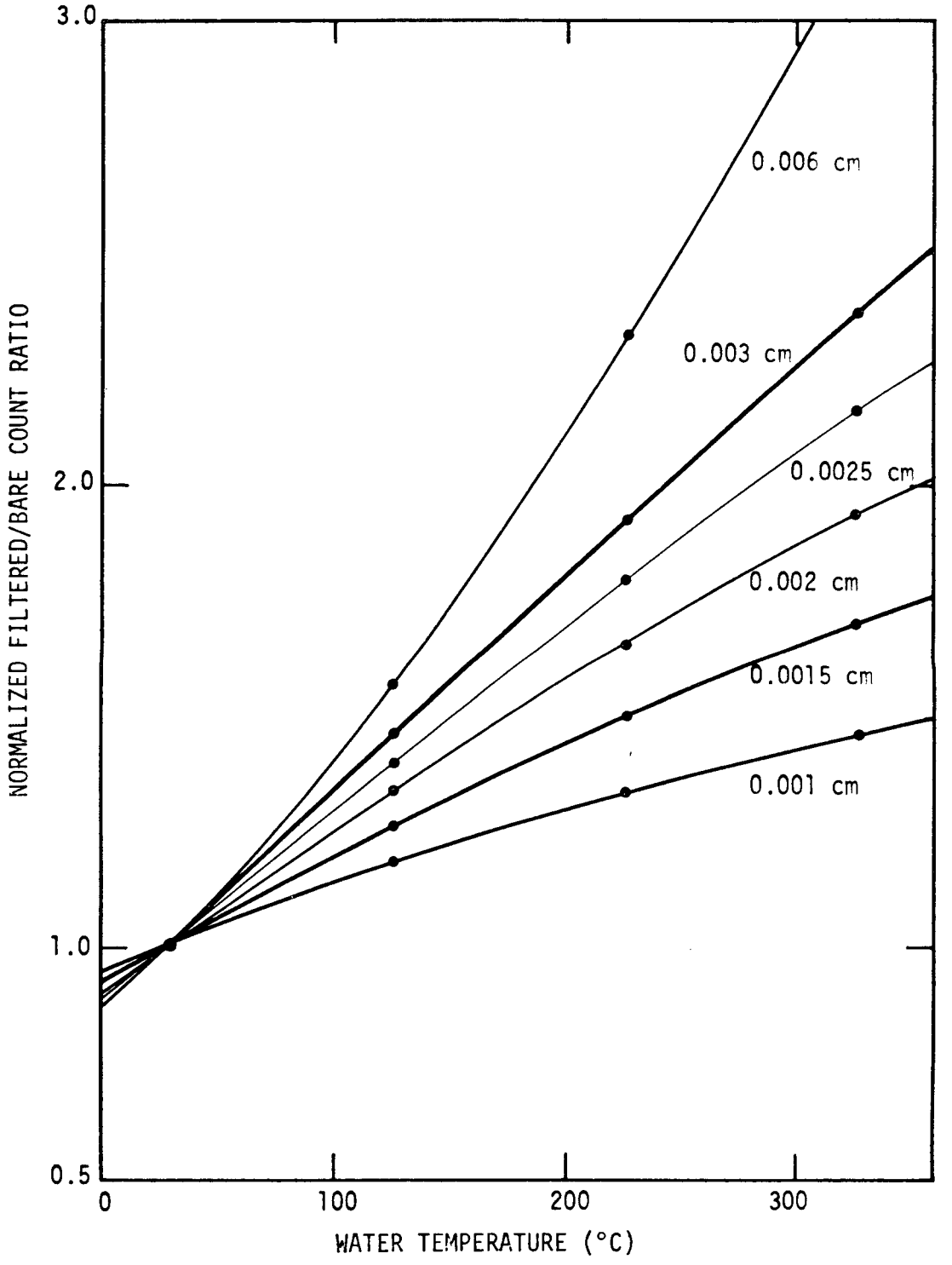

Figure 16. Calculated formation temperature gauge response, Equation 6, in water using a RS-P4-0410-204 He-3 filled detector, and natural isotope abundance gadolinium filters of various thicknesses. These curves have been normalized to the corresponding count ratio values at 27°C.

however, is achieved at the expense of lower transmission as shown by the corresponding absolute values of the count ratios. Therefore, the system sensitivity is limited by the filter transmission, and a filter thickness should be used which renders the gauge sufficiently sensitive at reasonable filter transmission values. Put another way, the filter transmission must be sufficiently high to yield detector count rates with high statistical accuracy at reasonable counting intervals. Comparing the computed temperature gauge response corresponding to the various filters it is apparent that the highest sensitivity is obtained with the "thick" gadolinium filters. On this basis a ~0.006 cm thick gadolinium filter appears to be the most suitable.

The accuracy of the computed values of the count ratio, R, can be estimated in terms of the relative uncertainties in the thermal neutron flux, the detector counting efficiency, and the filter transmission. This is readily accomplished by the standard error propagation method once the integrals in Equation 6 are approximated by sums in the process of numerical integration. In other words, since

$$R = \frac{C_F}{C_B} \sim \frac{\sum_i \Delta E_i \cdot \Phi(E_i) \cdot \tau_F(E_i, t_F) \cdot \epsilon(E_i)}{\sum_j \Delta E_j \cdot \Phi(E_j) \cdot \epsilon(E_j)} \quad , \tag{18}$$

$$\sigma_R^2 \sim \left\{ \Delta E_i \cdot \epsilon(E_i) \cdot \sum_j \Delta E_j \cdot \Phi(E_j) \cdot \epsilon(E_j) + \right.$$

$$\left. - (\Delta E_i)^2 \cdot \Phi(E_i) \cdot \epsilon^2(E_i) \right\}^2 \cdot \frac{e^{-2 \cdot \Sigma_a(E_i) \cdot t} \cdot \sigma^2_{\Phi(E_i)}}{\left[\sum_j \Delta E_j \cdot \Phi(E_j) \cdot \epsilon(E_j) \right]^2} +$$

$$+ \left\{ \Delta E_i \cdot \Phi(E_i) \cdot \sum_j \Delta E_j \cdot \Phi(E_j) \cdot \epsilon(E_j) + \right.$$

$$\left. - (\Delta E_i)^2 \cdot \Phi^2(E_i) \cdot \epsilon(E_i) \right\}^2 \cdot \frac{e^{-2 \cdot \Sigma_a(E_i) \cdot t} \cdot \sigma^2_{\epsilon(E_i)}}{\left[\sum_j \Delta E_j \cdot \Phi(E_j) \cdot \epsilon(E_j) \right]^2} +$$

$$+ \left\{ \frac{\Delta E_i \cdot \Phi(E_i) \cdot \epsilon(E_i)}{\sum_j \Delta E_j \cdot \Phi(E_j) \cdot \epsilon(E_j)} \right\}^2 \cdot t^2 \cdot e^{-2 \cdot \Sigma_a(E_i) \cdot t} \cdot \sigma^2_{\Sigma_a(E_i)} , \tag{19}$$

where σ_R, $\sigma_{\Phi(E_i)}$, $\sigma_{\epsilon(E_i)}$, $\sigma_{\Sigma_a(E_i)}$ are the uncertainties in the count ratio, and the flux, detector efficiency, and filter absorption cross section at neutron energy E_i. Assuming that the relative uncertainty in the flux is ±5 percent throughout the thermal energy range, the relative uncertainty in the computed counting efficiency is ±0.5 percent, and the relative uncertainty in the neutron absorption cross section is ±2 percent, the uncertainty in the calculated count ratios, R, is ±1 percent in the tmperature range considered. The corresponding uncertainty in the temperature for the system using a 0.006 cm thick gadolinium filter is $\sim \pm 2^{o}$C. Since the sensitivity is lower for the various other filters considered the corresponding temperature uncertainty will be greater than $\pm 2^{o}$C.

The sensitivity of the temperature gauge utilizing a 0.006 cm thick gadolinium filter is plotted in Figure 17. The quantity plotted is the percent change in the computed count ratio per ^{o}C change in the water temperature. It should be pointed out that this sensitivity represents an order of magnitude improvement over our preliminary estimates (Figure 3).

The effect of the detector efficiency on the gauge response has been examined by comparing the calculated count ratios corresponding to two detectors with different counting efficiencies, i.e., different fill gas pressures. The two detectors considered are the RS-P4-0410-204 (20 atm fill gas pressure) and the five atmosphere fill gas pressure detector whose counting efficiencies are shown in Figure 6. The computed count ratios are plotted in Figure 18. The more efficient (higher fill gas pressure) detector yields higher count ratios and a slightly higher slope of the count ratio versus temperature curve. Therefore, the temperature gauge utilizing the more efficient detector is more sensitive to temperature changes.

In an infinite moderating medium with a uniformly distributed neutron source, the flux given by Equation 1 is independent of position. In a finite moderator, localized source situation, however, the 1/E portion of the neutron energy distribution is position dependent in the immediate vicinity of the source. In other words, C (in units of n) in Equation 1 decreases with increasing distance from the source approaching its infinite moderator-uniformly distributed source value at points sufficiently removed from the neutron source. Thus at sufficient distance from the source, a state of equilibrium is established between thermal neutron diffusion and fast neutron thermalization. Beyond the distance necessary for the onset of this equilibrium C stays fixed, and the neutron flux, Equation 1, in the finite geometry differs only slightly from that in the infinite medium-uniformly distributed source situation.

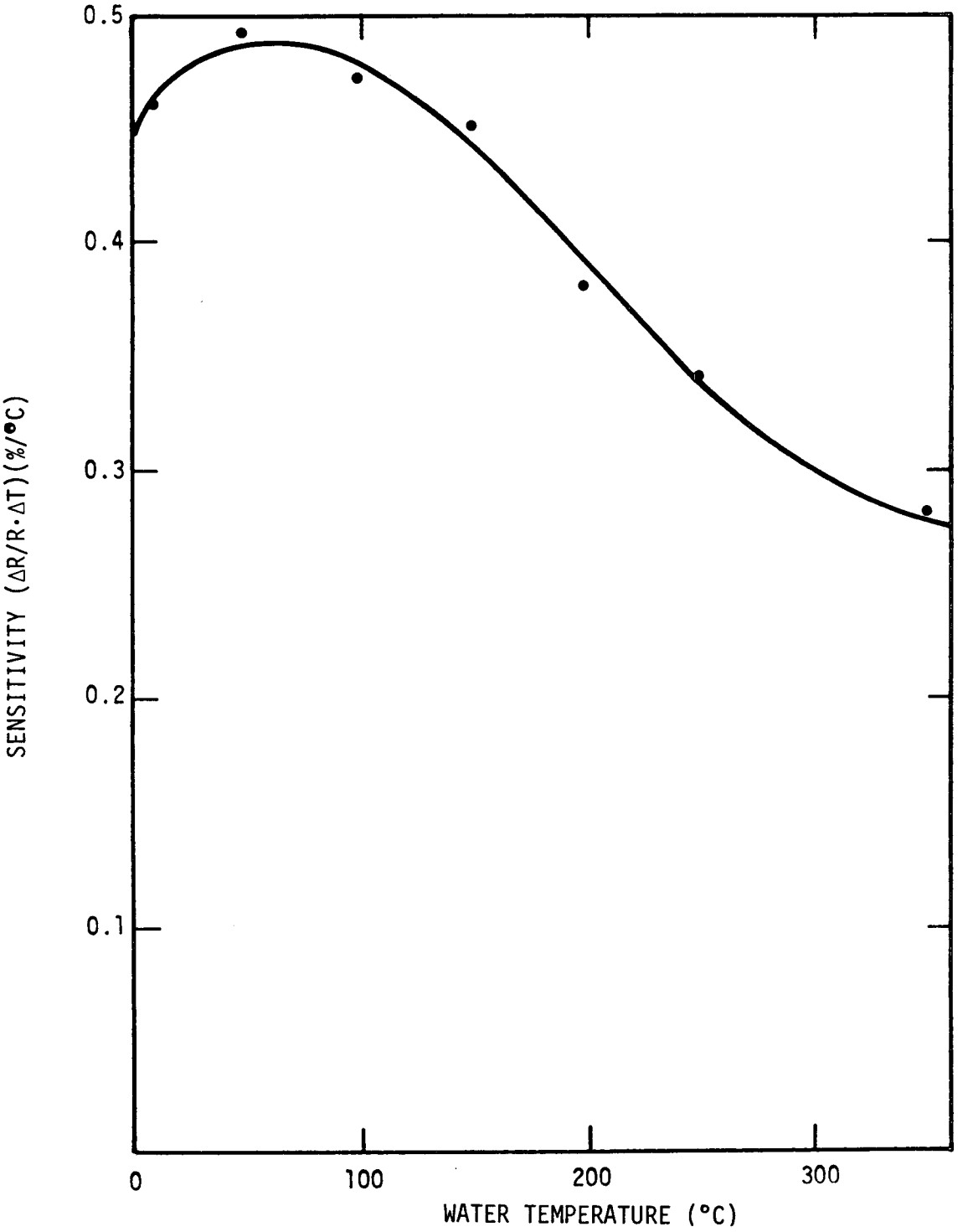

Figure 17. Formation temperature gauge sensitivity derived from the calculated temperature gauge response in water using Equation 6, an RS-P4-0410-204 He-3 filled detector, and a 0.006 cm thick natural isotope abundance gadolinium filter.

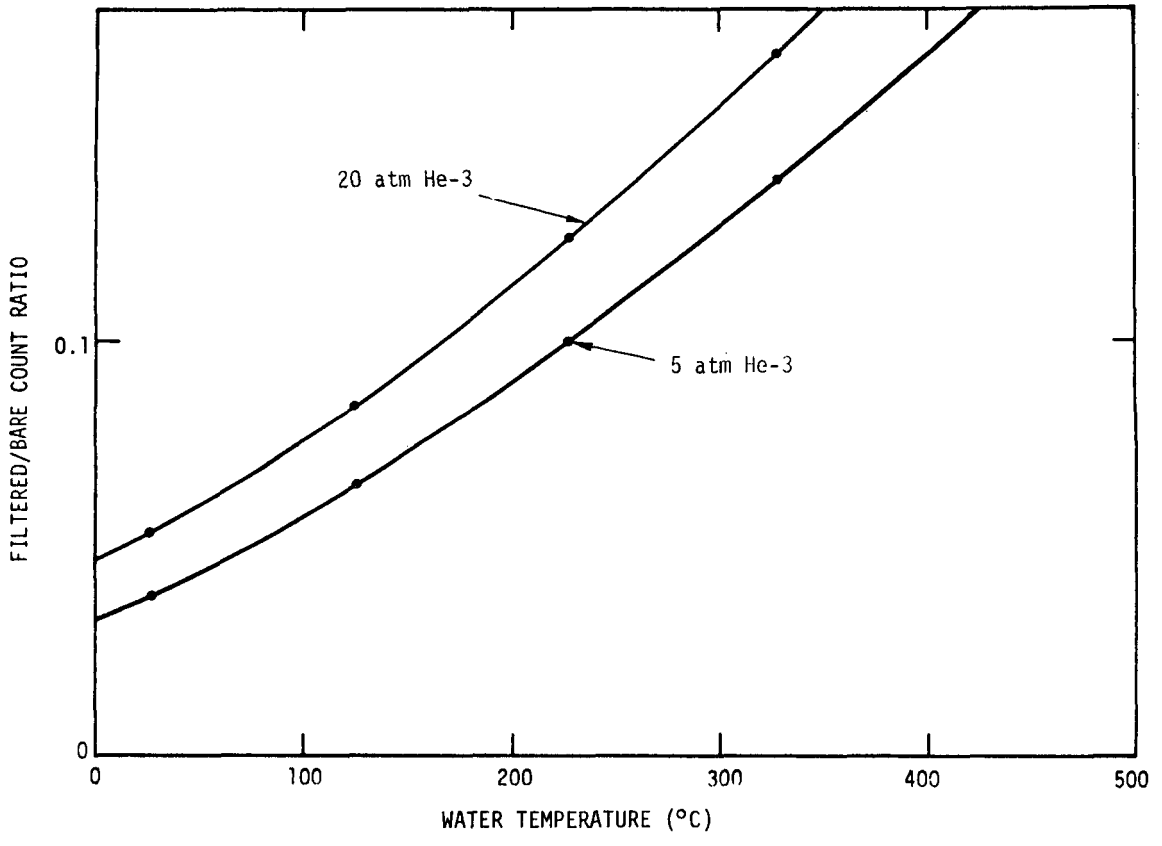

Figure 18. Calculated formation temperature gauge response using Equation 6 with a RS-P4-0410-204 He-3 filled detector and a similar detector with five atmospheres fill gas pressure and with a 0.006 cm thick natural abundance gadolinium filter. Higher sensitivity is obtained with higher detector efficiency, i.e., higher fill gas pressure.

The effect of position dependence of $\Phi(E)$ on the temperature gauge response has been examined by comparing the computed count ratios corresponding to neutron fluxes with various numbers of neutrons in the 1/E portion of the energy distributions, i.e., for various values of C. These ratios are plotted in Figure 19. It is apparent that a higher 1/E contribution (small source to detector distance) results in higher count ratios but lower sensitivity (lower slope of the count ratio versus temperature curve). Therefore, the highest possible sensitivity to temperature changes can be obtained by "correcting" the filtered and bare detector responses to remove the contributions by the 1/E (slowing-down) part of the slow neutron spectrum. As discussed in subsection 2.1, the correction is determined from the response of the Cd-covered detector.

2.4 EXPERIMENTAL STUDY OF THE TEMPERATURE GAUGE RESPONSE

2.4.1 Preliminary Measurements

Having computed the response of the formation temperature gauge on the basis of a simplified model as described in the previous subsection, simple, preliminary measurements were performed. Their purpose was to demonstrate the scientific feasibility of the technique by verifying results of the calculation and the validity of the data analysis method discussed in subsection 2.1 before proceeding to more elaborate, costly, realistic experiments. The preliminary measurements were performed with an experimental arrangement using the simplest possible geometry.

2.4.1.1 Experimental Arrangement

The test media in which the preliminary measurements were performed were placed in a cylindrical container made of 1/8 inch thick stainless steel. A photograph of the apparatus is presented in Figure 20. Its diameter was 10.5 inches and its length 27 inches. Two immersion heaters capable of supplying 1000 watts each at 240V were fitted to the bottom of the container. A Variac was used to control the voltage applied to the heaters and hence their power output and test medium temperature. Provisions were made to circulate the water in the various media from the bottom of the tank to the top in a closed loop using a pump with maximum circulation rates of $\sim$7 gallons/min. This was done to ensure that the test medium was evenly heated. Alternatively the water could be circulated through a heat exchanger to enhance cooling. This was

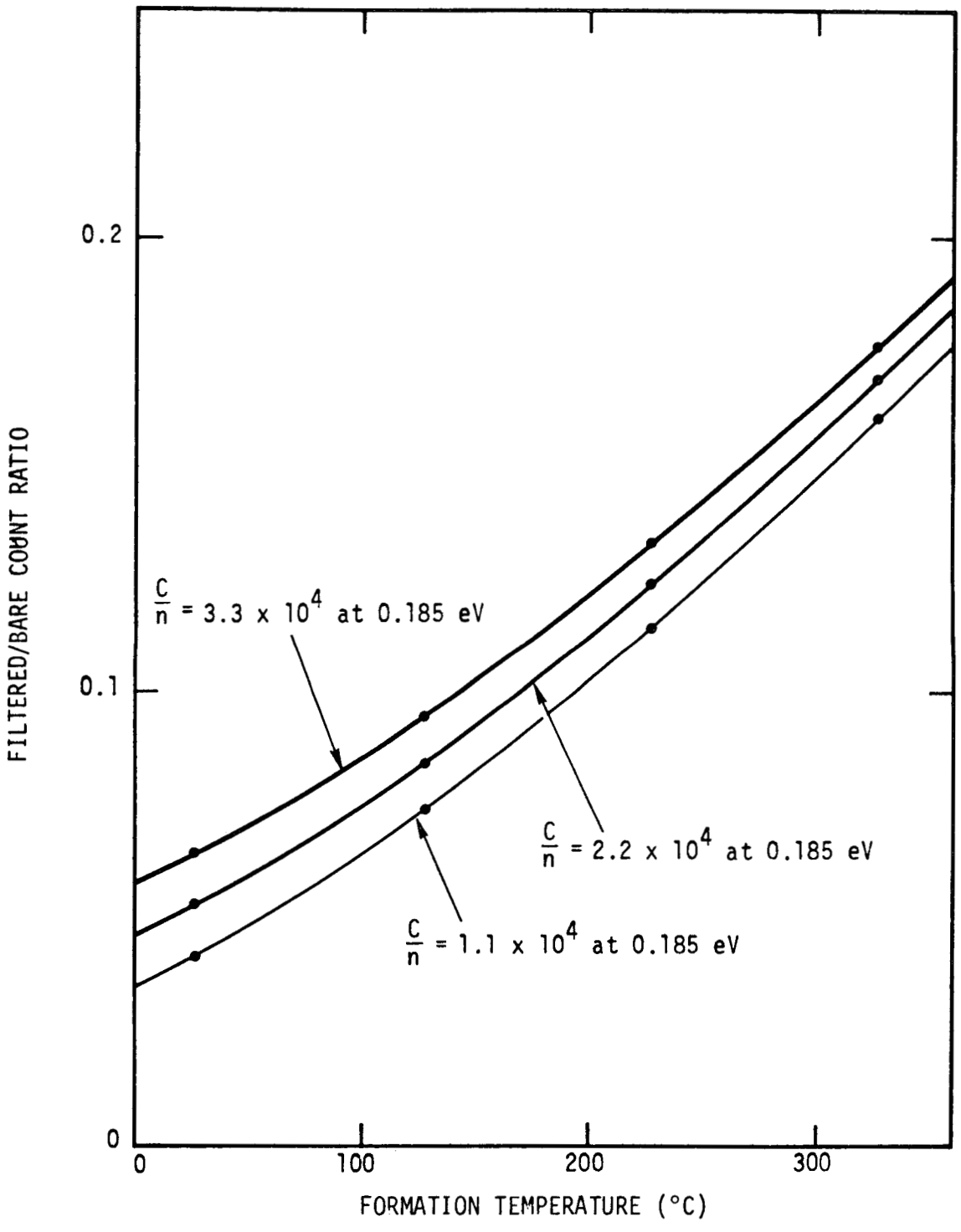

Figure 19. Calculated formation temperature gauge response using Equation 6 for various 1/E spectrum amplitudes (various values of C) with a RS-P4-0410-204 He-3 filled detector and a 0.006 cm thick natural abundance gadolinium filter. Higher sensitivity results with more complete thermalization, i.e., lower 1/E contribution.

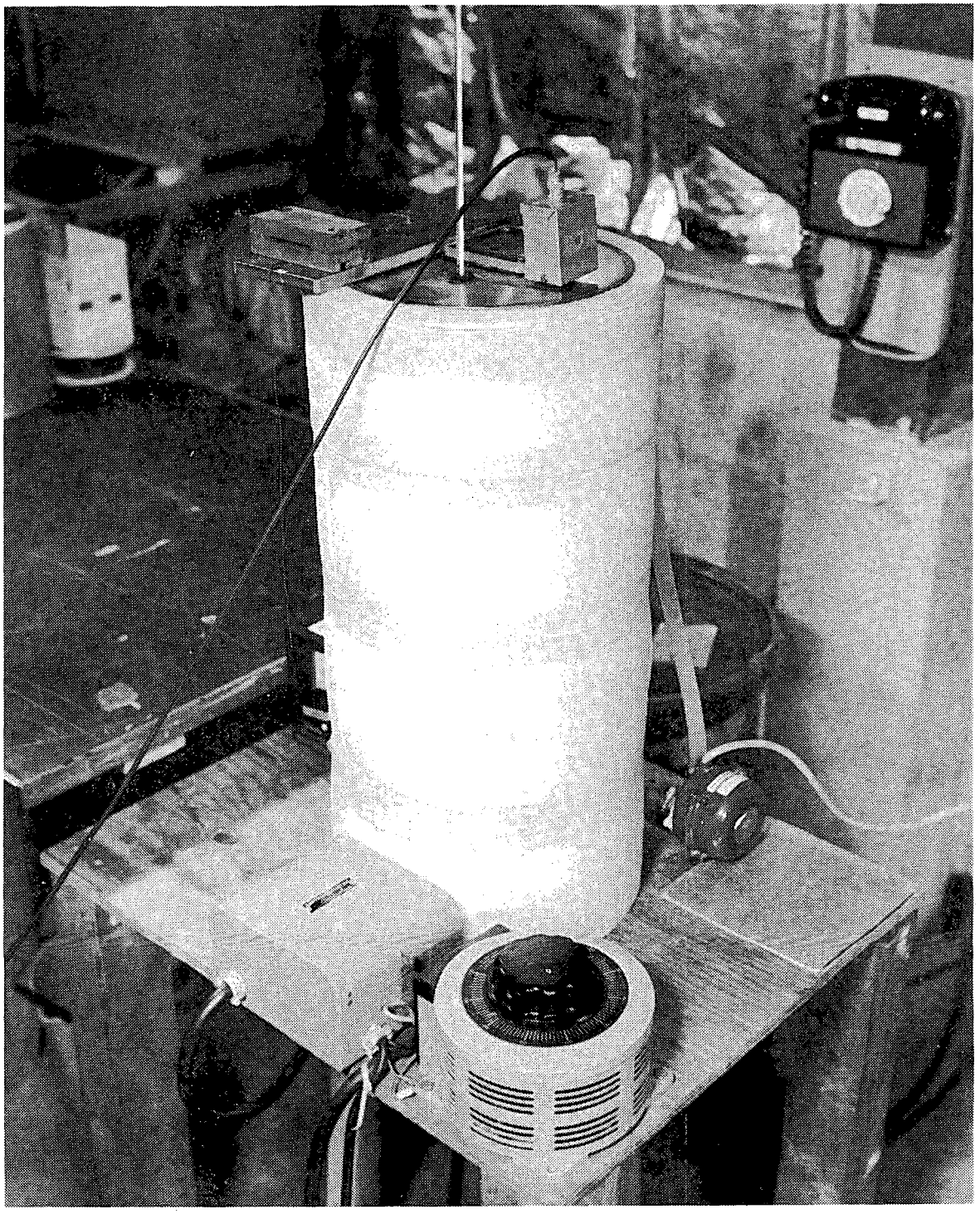

Figure 20. Photograph of experimental equipment used for the preliminary measurements.

necessary to reduce the times required to lower the test medium temperature, and also to provide additional temperature control. Such control was accomplished manually. The test medium temperature was determined sufficiently accurately (to within a few tenths of a degree) using a laboratory mercury thermometer.

Figure 21 is a schematic top view of the experimental arrangement showing the positions of the Cf-252 source and the He-3 filled detector. Very thin wall stainless steel tubes with the bottom ends closed were immersed in the test medium. They were located on a diameter each approximately two inches away from the tank wall and with a separation distance of six inches between their centers. The californium source (0.3 μg Cf-252 equivalent to $\sim$150 μCi) was lowered into one of the tubes $\sim$7 inches below the test medium surface and the detector was inserted into the other. Although most of the measurements described below were performed in this configuration data were taken at various other source to detector distances and source location depths to ensure that the above configuration was optimum.

The detector used was an RS-PA-0410-204 He-3 filled proportional counter designed for oil well logging application. The associated counting electronics used were standard NIM bin components available at IRT. The filter used was a cylinder with diameter slightly larger than that of the detector ($\sim$1/2 inch), and two mils (0.005 cm) thick. It was made of two layers of 1 mil thick gadolinium foil.

2.4.1.2 Experimental Results

The measurements discussed in this section consist of counts observed with various test media at different temperatures between 20^{o}C and 95^{o}C. At each temperature, counts were generally recorded with the detector bare (unfiltered), and alternately covered with a two-mil (0.005 cm) thick gadolinium sleeve, or a 30 mil (0.076 cm) thick cadmium sleeve. The measurements were made after the test medium temperature had been stabilized at preselected values by adjusting the voltage to the immersion heaters and/or the water circulation rate through the heat exchanger. Sufficient counts were accumulated at each temperature for the statistical uncertainty to be acceptably low. The count ratio (R_o) was computed at each temperature by dividing the Gd-filtered detector count by the bare detector count at the same temperature, Equation 6. The "corrected" count ratio (R) was computed by first subtracting the 1/E contributions from the observed total bare and Gd-filtered detector counts, Equations 11 and 12, and then dividing the corrected filtered detector count by the corrected bare detector count, Equation 8.

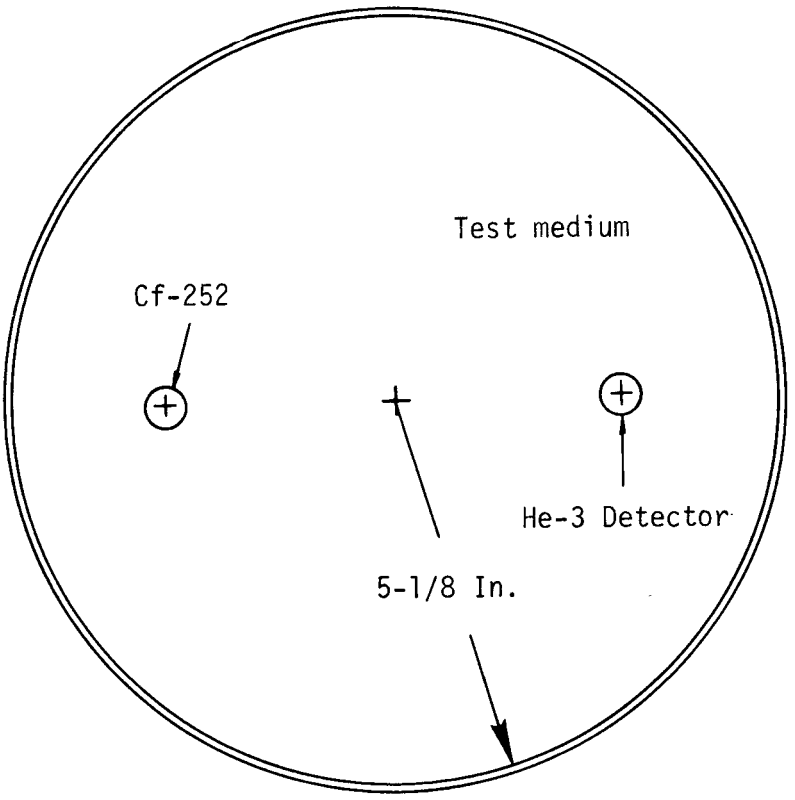

Figure 21. Schematic of the top view of the experimental arrangement for preliminary temperature gauge response measurements. The diagram shows the relative positions of the neutron source and detector.

Results of the computational analysis indicated that the temperature gauge sensitivity is higher the smaller the relative number of neutrons with energies in the slowing-down (1/E) region, i.e., the lower the value of C in Equation 1. In fact, in a large but finite moderator with a localized neutron source the sensitivity is maximum when the detector is located at points sufficiently distant from the source where equilibrium exists between fast neutron thermalization and thermal neutron diffusion. This is the same requirement noted earlier for a point source arrangement to approximate the results of the uniformly distributed, infinite source computations. In order to demonstrate the validity of the computations it was necessary to compare the calculated filtered-to-bare detector count ratios with the corresponding quantities measured in water. Therefore, it was important at the outset to determine the optimum source to detector distance in water. This distance is determined by two competing factors. The thermal neutron flux decreases rapidly with distance away from the source as the sensitivity increases up to a certain point. Therefore, the optimum distance is that at which the above equilibrium state is reached if it is not so large that the thermal neutron flux is unacceptably low. In the present arrangement it was found to be ~6 inches (15.24 cm). This value was determined by measuring the count ratio, R_o, for various source to detector distances. The count ratio reached its minimum value slightly below the six-inch source to detector separation.

Following the above optimization of the experimental arrangement, the temperature variation of the Gd-filtered-to-bare detector ratio, R_o, was obtained with water as the test medium. The data generated is presented in Figure 22. The error flags represent the corresponding statistical uncertainities. Count ratios were determined more than once at several temperatures to demonstrate repeatability. On the same figure is shown the calculated response for the infinite moderator--uniformly distributed infinite source situation. It can be readily seen that although the agreement between the measured and calculated response is not exact, the maximum diagreement is about 15 percent at the lower temperatures. (Note that the vertical axis of this figure starts at a count ratio value of 0.05 not 0). The discrepancy is largely due to the finite dimensions of the experimental arrangement, although part of it is certainly due to the fact that the spectra used in the calculations are slightly different from those observed when a point source is immersed in an effectively infinite water moderator (Ref 10). The diameter of the test medium container may not have been sufficiently large to approximate an infinite medium in this dimension. Therefore, the neutrons escaping the water may result in a modified spectrum accounting largely for the above disagreement.

It must be emphasized that the calculations are not intended to provide a calibration for the temperature gauge. In view of the above discussions, the discrepancy between observed and calculated ratios is of no great concern. The above comparison was made only to demonstrate the validity of the simplified model calculations. On the basis of this comparison, it is reasonable to assume that the results of the computations are valid. The significant facts are that both the calculated and the measured count ratios vary with temperature, and the relative variations are approximately equal. More importantly, the variations are reasonable with regard to the feasibility of the method. The average sensitivity implied by both the calculated and the measured responses shown in Figure 22 is about 0.3 percent change in the count ratio, R_o, per ^oC change in the temperature.

In addition to demonstrating the reasonable nature of the simplified calculations, the above, preliminary measurements demonstrate also the feasibility of the method when the medium temperature is the only variable, i.e., when the neutron properties are fixed. In order to demonstrate that the present method is capable of determining unambiguously the temperature of an arbitrary medium, it was necessary to determine experimentally the behavior of the Gd-filtered-to-bare detector count ratio under various conditions of T, Σ_a, and $\xi\Sigma_s$. It should be recalled (subsection 2.1) that the moderating medium temperature, T, neutron absorption cross section, Σ_a, and moderating power, $\xi\Sigma_s$, are the three parameters which determine the neutron temperature and hence the count ratio. The measurements which are discussed below were designed to demonstrate the independence of the three parameters and the validity of the analysis discussed in subsection 2.1.

Gd-filtered-to-bare detector count ratios were obtained using test media with different neutron absorption and moderating properties and at various temperatures. The test media used are listed in Table 1. In the same table are also listed the values of the thermal neutron absorption and scattering cross sections and the average logarithmic energy loss per collision, ξ. These were calculated on the basis of elemental composition of the various media and published cross section data. Water, water-saturated silica sand (silica + water), and water-saturated silica sand lead shot mixture (silica + lead + water) represent media with different neutron moderating power. The addition of boric acid (H_3BO_3) to water and water saturated silica sand increases the neutron absorption cross section of these media (boron is a strong thermal neutron

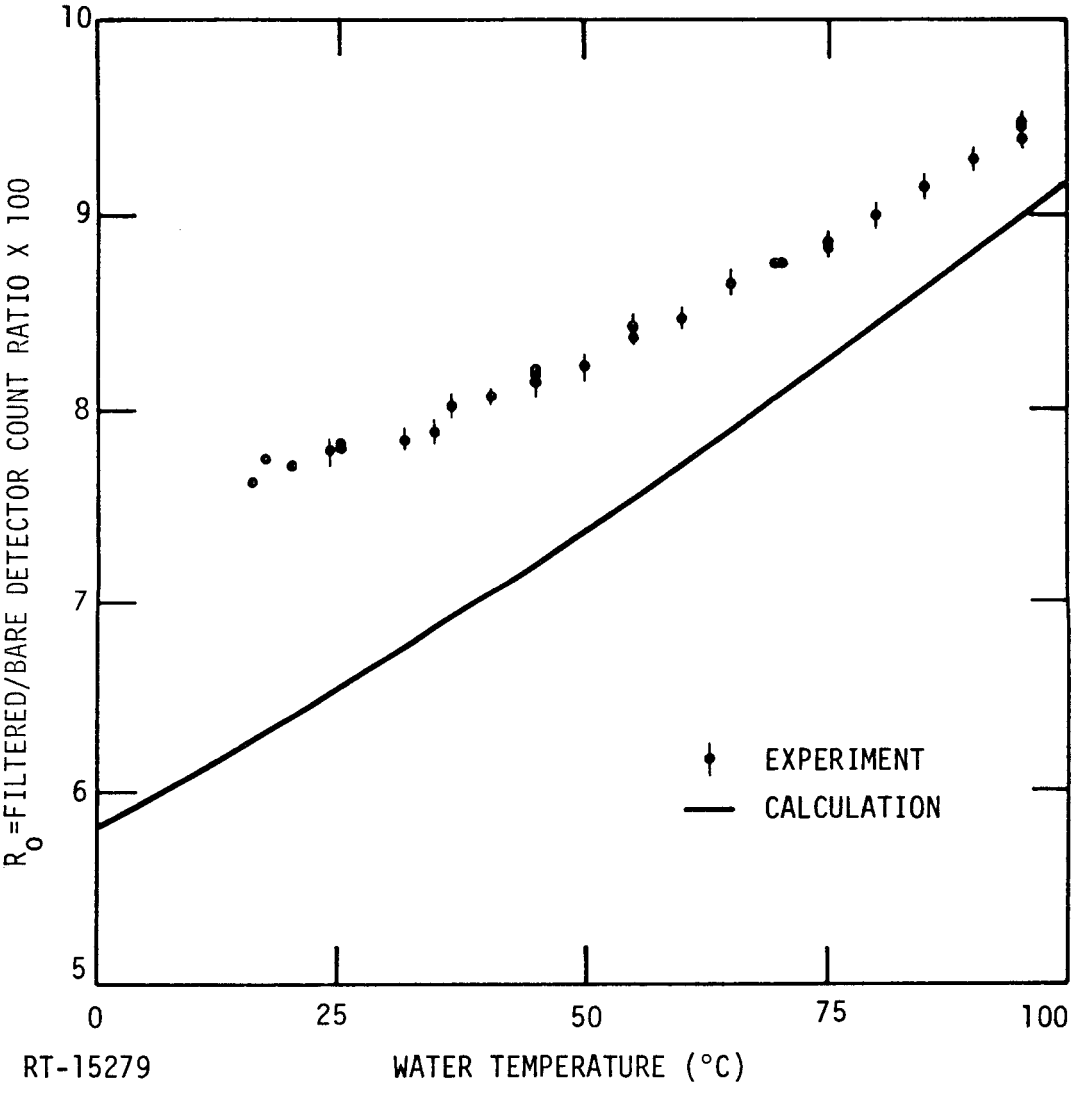

Figure 22. Calculated and observed count ratios of Gd-filtered-to-bare detector counts in water. The calculated response (line curve) was obtained for an infinite medium using Equation 6. The measured response corresponds to the finite geometry arrangement in Figure 20. In both cases the filter is 0.005 cm thick natural abundance gadolinium.

absorber), but, in the concentration used, it leaves the moderating power, $\xi\Sigma_s$, essentially unchanged. The two water boric acid solutions listed contain different amounts of H_3BO_3.

Table 1. Summary of the Neutron Properties of the Various Test Media Used for the Preliminary Measurements

Test Medium	Σ_a (cm^{-1})	ξ	Σ_s (cm^{-1})
Water	0.0222	0.9642	3.443
Water + Boric Acid	0.0306	0.9639	3.445
Water + Boric Acid	0.0389	0.9636	3.447
Silica + Water	0.0122	0.8873	1.665
Silica + Water + Boric Acid	0.0145	0.8872	1.666
Silica + Lead + Water	0.0108	0.7915	1.356

The count ratios, R, observed for the various test media are plotted in Figure 23 as functions of the medium temperature. These ratios have been corrected for the 1/E ("background") contribution. This was necessary for the meaningful comparison of the response obtained for media with different moderating power. The slow neutron spectrum component in the slowing-down region depends on the moderating power of the medium. Therefore, the 1/E contribution to the bare and Gd-filtered detector responses is different for the test media with different values of $\xi\Sigma_s$ (for formations containing different concentrations of hydrogen). Furthermore, by eliminating the 1/E contribution, the count ratio, R, becomes more sensitive to temperature changes. The appropriate corrections were determined semi-empirically from the observed response of the Cd-covered detector (subsection 2.1).

The reasons for presenting the data in the manner shown in Figure 23 is to exhibit the dependence of the count ratio on the various parameters, and to demonstrate the inadequacy of this simple analysis. It is obvious from this figure that the value of the

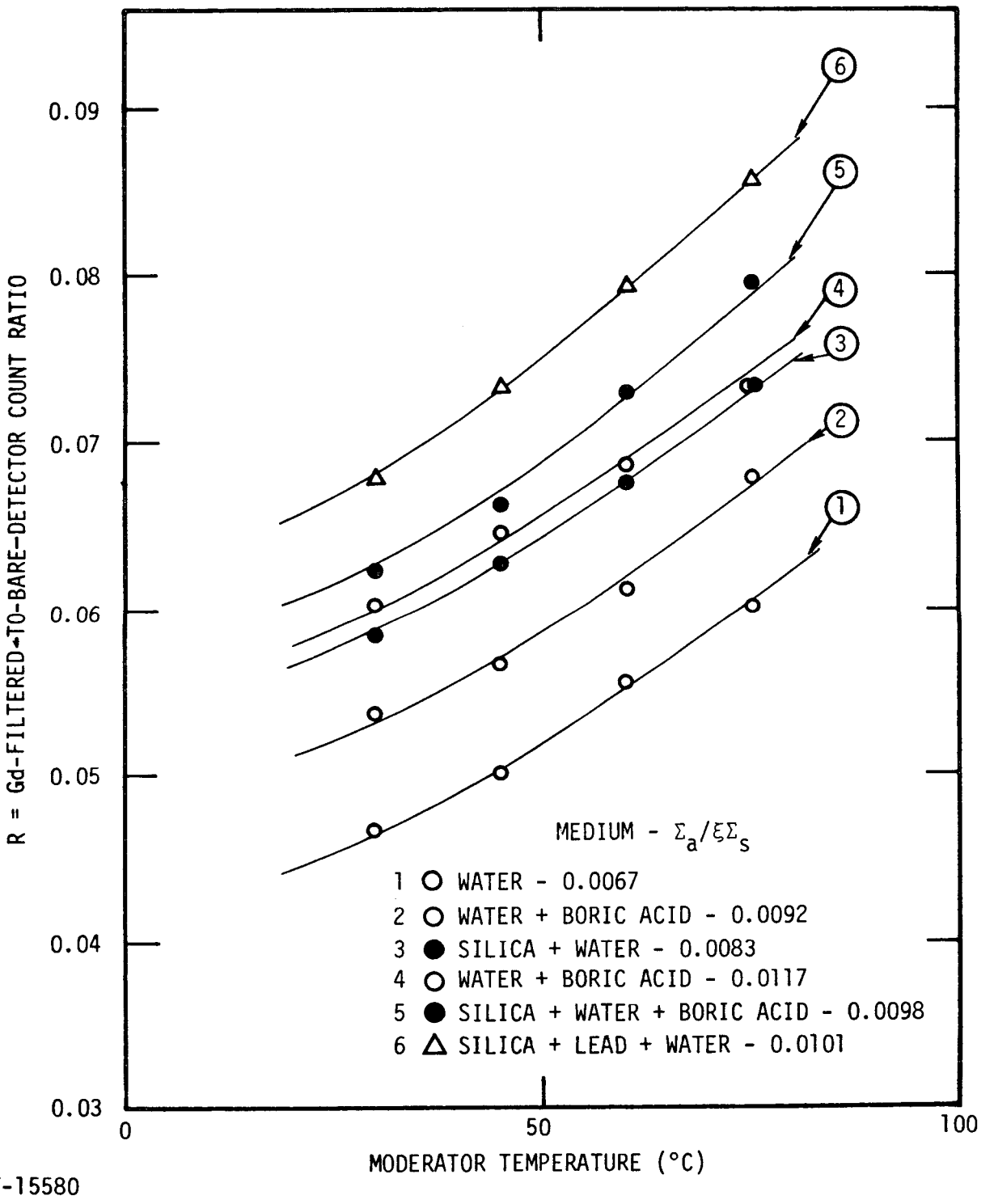

Figure 23. Observed count ratio, R, in the various test media as a function of the temperature. The data were obtained with the preliminary experimental arrangement and were experimentally corrected for the 1/E background.

count ratio alone is not sufficient to determine the medium temperature unambiguously. A more complete analysis of the available information, i.e., use of the bare and Cd-covered detector responses in addition to the count ratio, R, is necessary to accomplish that. This is demonstrated in the following paragraphs.

The same data shown in Figure 23, are plotted in Figure 24 as a function of the bare-to-Cd-covered detector count ratio. As in Figure 23, the open circles represent the data obtained in water and water boric acid solutions. The full circles represent the results of measurements performed in water-saturated silica and and silica sand saturated with water boric acid solution. The triangles are the data obtained for the water saturated silica sand lead shot mixture. The lines drawn through the data represent either measurements performed at constant temperature (labeled in ^{o}C), or at constant neutron absorption cross section and neutron moderating power (labeled by the corresponding Σ_a and $\xi\Sigma_s$ values).

The reason for analyzing the data in this manner was to determine whether Σ_a and $\xi\Sigma_s$ are independent parameters or T_n (and hence R) depends simply on the ratio $\Sigma_a/\xi\Sigma_s$ as is the case for an infinite medium with a uniformly distributed neutron source, Equation 3. Since the bare (unfiltered) detector response, C_B^{th}, provides a measure of the absorption cross section, and the Cd-covered detector count, C_{Cd}, provides a measure of the moderating power, the ratio C_B^{th}/C_{Cd} is a measure of $\Sigma_a/\xi\Sigma_s$. The difference in the slopes of lines representing constant moderation and absorption properties for media with different moderating power, $\xi\Sigma_s$, but similar values of the ratio C_B^{th}/C_{Cd} clearly indicates the independence of the moderation and absorption parameters. It verifies our previous assertion of three independent variables and hence the need for a three-dimensional representation of the count ratio data, R, as a function of C_B^{th} and C_{Cd}. When R, C_B^{th}, and C_{Cd} are plotted along three orthogonal axes the above data represents points in a three dimensional space. Each point is determined by the observed response of the detector in turn bare (unfiltered), Gd-filtered, and Cd-covered, i.e., by $R = C_{Gd}^{th}/C_B^{th}$, C_B^{th}, and C_{Cd}. Moreover, each point in this space corresponds to the unique set of conditions under which the measurements were performed, i.e., the values of T, Σ_a, and $\xi\Sigma_s$.

Figure 25 presents a mapping (cross plot) of the data obtained for water and the water boric acid solutions. The count ratios, C_{Gd}^{th}/C_B^{th}, are plotted along the Y-axis, and the bare detector, C_B^{th}, counts along the x-axis. The Cd-covered detector counts,

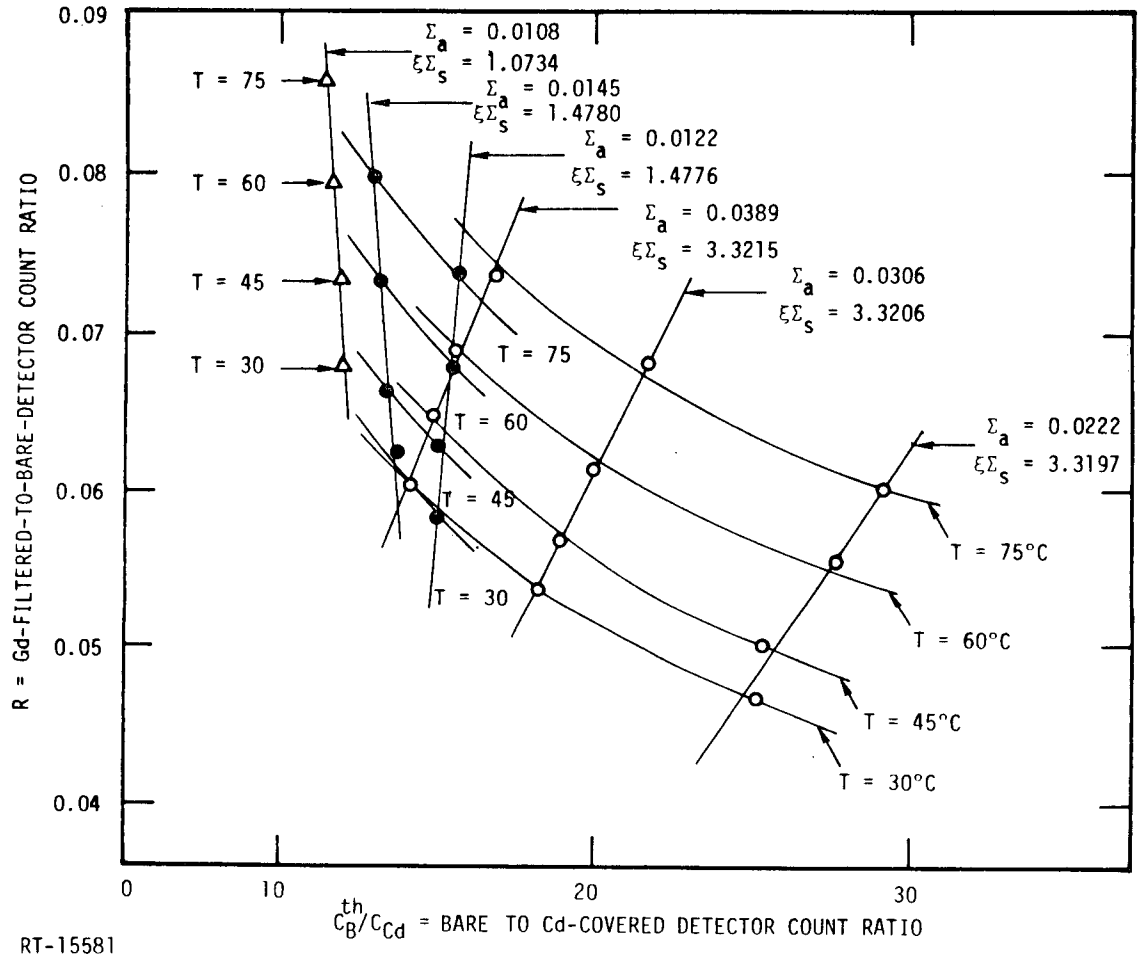

Figure 24. Mapping of the count ratio as a function of the ratio C_B^{th}/C_{Cd}, i.e., the ratio of absorption to moderating properties, for various conditions of formation temperature, absorption and moderating power. The curves represent conditions of constant temperature (in ^{o}C) or constant absorp- and moderation (in cm^{-1}). The difference in the slope of lines representing constant moderation and absorption for media with different moderating power, $\xi\Sigma_s$, but similar values of C_B^{th}/C_{Cd} clearly demonstrates the independence of the moderation and absorption parameters.

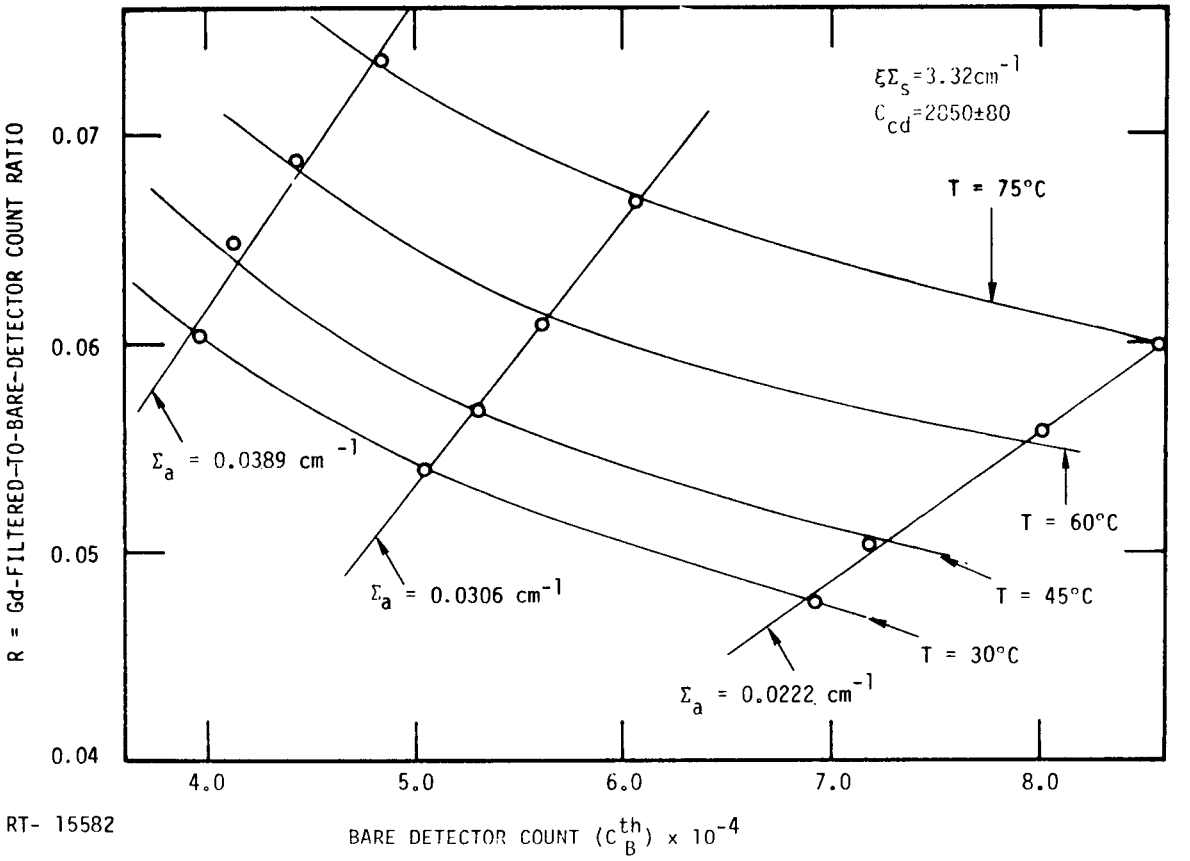

Figure 25. Mapping of the count ratio as a function of the bare detector counts for various conditions of the formation temperature and absorption, but for constant moderating power. The data are those measured in water containing various amounts of absorber (H_3BO_3). The Cd-filtered detector counts which depend on the moderating properties of the medium are constant at C_{Cd} = 2850 ±80. These data represent a plane in the three-dimensional mapping of $R(T, C_B^{th}, C_{CD})$.

C_{Cd}, are plotted along the Z-axis (perpendicular to the page). C_{Cd} is constant, within the experimental uncertainty, for the test media consisting of water and water boric acid solution. This is to be expected, since the moderating power, $\xi \Sigma_s$, of the water is not changed significantly by the addition of small amounts of boric acid (Table 1). Therefore, Figure 25 represents a single plane in the three-dimensional plot of $R(T, \Sigma_a, \xi \Sigma_s)$, the plane being perpendicular to the C_{Cd} axis. The curved lines in this plane represent measurements performed at constant temperature (variable Σ_a), while the straight lines represent measurements made in media with the same neutron absorption cross section. The significance of this analysis is that each point on the plot which is determined by the measurements in the three regions of the spectrum (subsection 2.1) corresponds to a unique set of conditions under which the measurements were performed. Thus, each set of measurements determines uniquely the value of the medium temperature, and equally unique values of the neutron absorption cross section and moderating power.

When the moderating power of the medium is different from that of water, the points determined by the corresponding measurements lie off the plane shown in Figure 25, but in another plane similar and parallel to it. Such a plane is presented in Figure 26. This is a mapping of the data obtained for water-saturated silica sand and silica sand saturated with water boric acid solution. The corresponding Cd-covered detector counts are again constant but different from those measured in water and the various water-boric acid solutions. This is clearly due to the different moderating power of the water and silica-water test media (Table 1). The silica-lead-water data lie in still another plane of constant C_{Cd}. They were not plotted, because only data for a single value of the absorption cross section have been obtained.

2.4.1.3 Experimental Technique Accuracy

The experimentally determined uncertainty in a single determination of the Gd-filtered-to-bare detector count ratio is ± 0.0004 for values of the ratios in the range from 0.045 to 0.090. This results in a temperature uncertainty of less than $\pm 3.5^{\circ}C$ near room temperature, to less than $\pm 2^{\circ}C$ near $100^{\circ}C$. These values of the temperature uncertainty are conservative estimates of the technique accuracy because no attempt was made to optimize the neutron counting system. That is, use was made of only a very small neutron source (0.3 μg Cf-252), reasonably short counting intervals (15 minutes), and standard detection and counting equipment available in our laboratory.

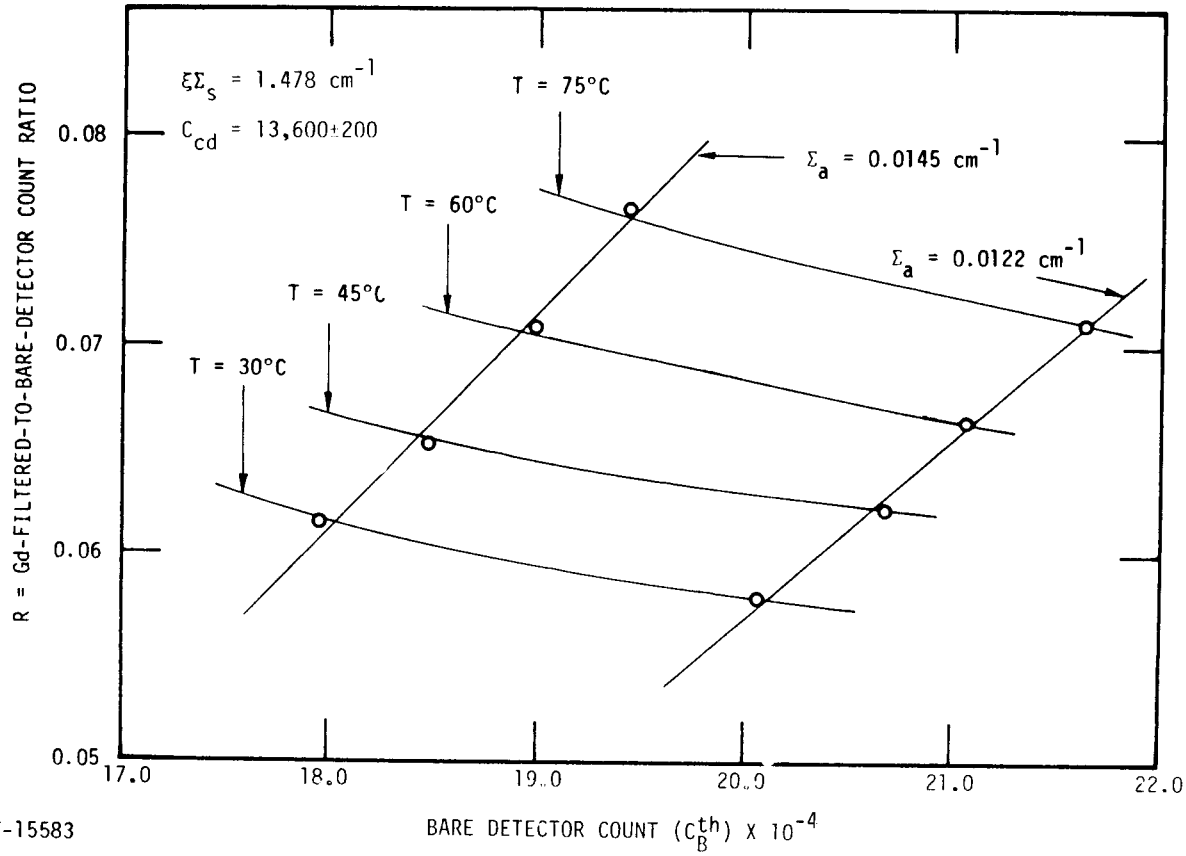

Figure 26. Mapping of the count ratio as a function of the bare detector counts for various conditions of the formation temperature and absorption, but for constant moderating power. The data are those measured in silica + water and silica + water + boric acid. The Cd-filtered detector counts are constant at C_{Cd} = 13,600 ±200. These data represent a plane in the three-dimensional mapping of $R(T, C_B^{th}, C_{Cd})$ different from that shown in Figure 25.

Therefore, a precision of $\pm 2^{o}C$ at a temperature of $300^{o}C$ is a reasonable projection of the above low temperature data.

Since the observed uncertainty due to counting statistics is ± 0.0002 to ± 0.0003 in the above ratio range, it is obvious that the uncertainty in the system response is largely due to counting statistics which depend entirely on the number of counts recorded by the neutron detection system. Therefore, it can be minimized by increasing the total number of recorded counts, i.e., by increasing the detetion efficiency, the neutron source strength, and/or the length of the counting interval. Systematic errors can result from system instabilities and these have to be determined by a large number of independent measurements. Having experimentally determined the temperature dependence of the system response, R, and the uncertainty in any single determination of this response, it was possible to estimate the total uncertainty in the temperature measurement. The above precision estimates take into account both the counting and systematic uncertainties. In the final analysis, however, it is expected that the perturbations caused by the borehole will be the limiting factor in achieving the best possible precision. The experiments described below and those proposed will help define these limitations.

2.4.2 Measurements in the Well Geometry

Geometry effects notwithstanding, the preliminary measurements described in the preceding section substantiate the results of our computations. Furthermore, they demonstrate the feasibility of the concept in the "simple" geometry and indeed justified proceeding with the second phase of the experimental study involving measurements in an arrangement simulating a geothermal well. A test stand used to perform these measurements is described below. Also described in the following paragraphs are the sonde mockup used to perform the initial measurements, the measurements themselves and their results. The purpose of these experiments was to evaluate the temperature sensor design and assess the effects of the borehole fluid on the gauge response. They also serve as the initial step in verifying the results of the preliminary measurements for the more complex, realistic geometry, and, thus, in demonstrating the engineering feasibility of the method. Additional measurements which are necessary to complete this task are discussed in the final section of the report.

2.4.2.1 Test Stand

A photograph presenting an overview of the test stand designed to simulate geothermal well conditions is shown in Figure 27. In addition to the test formation container located on the platform, the photographs shows the associated electronics for neutron counting and monitoring of the detector operation. At the far left is a heat exchanger whose function is discussed below. A schematic diagram of the system is presented in Figure 28. The test formation chamber is located on a platform so that the "borehole" and sonde mockup are accessible from the bottom as well as from the top. The test formation container is a large cylindrical tank made of 1/4-inch thick mild steel. It has a diameter of 54 inches (1.37 m) and it is 54 inches high. A concentric hole, the borehole, consists of a 10-inch (25.4 cm) outside diameter aluminum tube with wall thickness of 0.094 inches (0.239 cm). This borehole diameter was chosen to correspond roughly to the minimum diameter of an uncased geothermal well (Ref 11). As a result, the test formation thickness is 21.75 inches (55.245 cm). This dimension is several times greater than the effective infinite volume dimension for water but only about 2/3 the effective infinite volume dimension for dry silica. Effective infinite volume is the finite volume of a sample whose dimensions are sufficiently large so that the effect of the finite geometry on the quantity being measured is negligible. As a consequence of the above choice of the test formation thickness, practically all of the source neutrons entering the test volume will be thermalized within a few inches ($\sim$6 inches) from the borehole wall when the tank is filled with water. On the other hand, when the test formation is dry silica sand all but a small fraction (a few percent) of the neutrons traversing the 21.75 inches of silica will have been thermalized. It is not expected that this will have a significant effect on the results of this study. A larger sample volume for the present study would be impractical because of heating requirements.

In the present experimental arrangement, the power necessary to heat the test formation is provided by 12 strip heaters oriented parallel to the cylinder axis, and spaced uniformly around the periphery. Each heater generates 1250 watts of heat at 240V and can withstand temperatures as high as 250 to 300^{o}C. Variable voltage is provided by three coupled Variacs each controlling four heaters connected in parallel. The Variac output is switched on and off by a contactor switch which is operated by a thermocouple temperature controller so that it is engaged, and the Variac output is

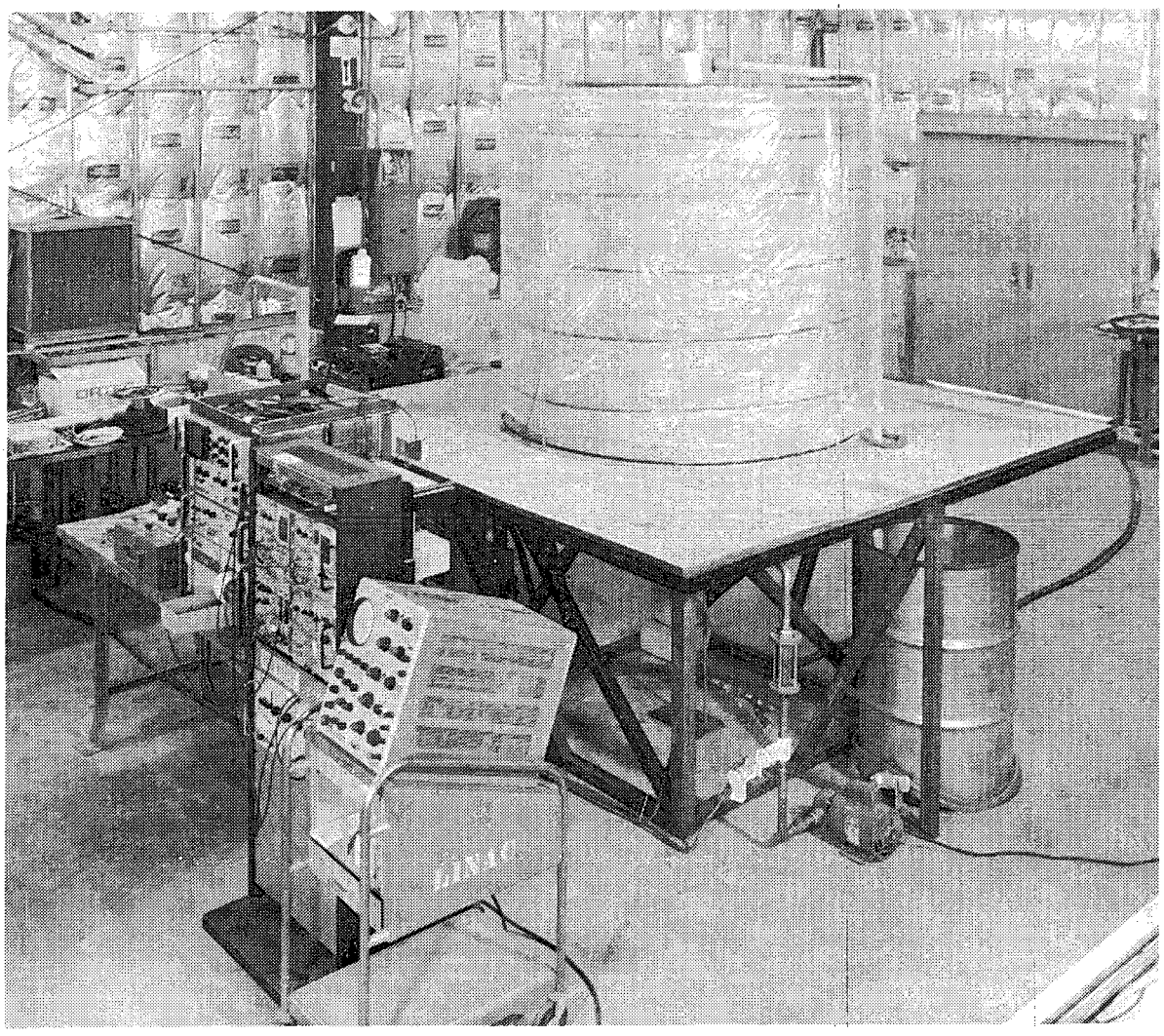

Figure 27. Overview of the geothermal test stand showing the heat exchanger (far left), the neutron counting electronics, and the test formation chamber.

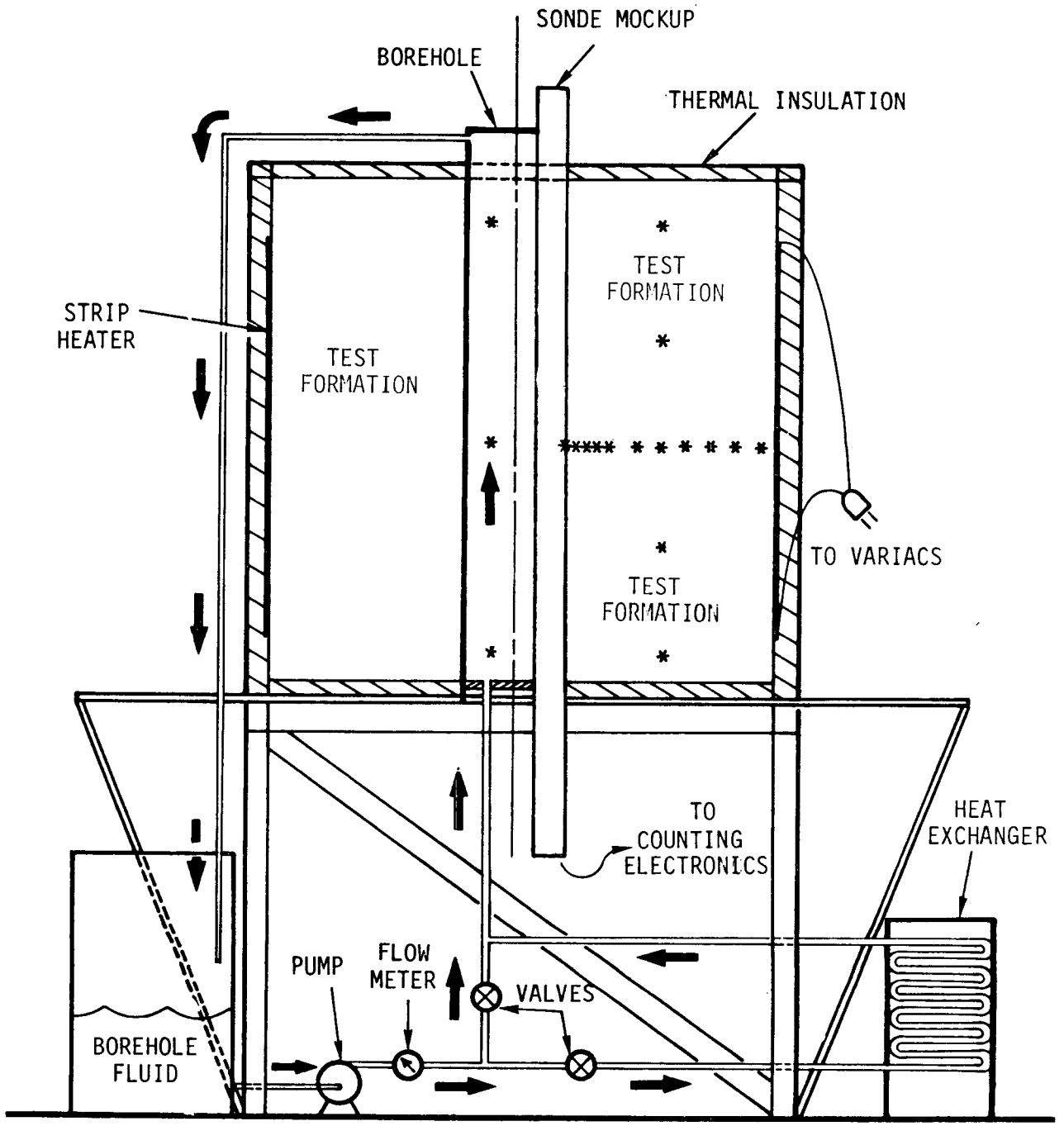

Figure 28. Schematic diagram of the formation temperature gauge test stand. Its various components and their dimensions are discussed in the text. (*) designate thermocouple positions.

applied to the heaters, when the controlling thermocouple indicates a temperature below the preset value. When the temperature has reached (or just passed) the value preset on the controller, the contactor is disengaged and the voltage to the heaters is cut off. Power to the strip heaters is then cycled on and off controlling the formation temperature automatically with small, periodic deviations from the preset value.

The controlling thermocouple is one of several thermocouples, located in the test formation and in the borehole. Their locations are designated by asterisks (*) in Figure 28. The rather large number of thermocouples may be necessary to determine very carefully the temperature variations within certain test formations. This will be important in interpreting the data. The thermocouples inside the central tube (borehole) are needed to monitor the temperature of the water which will be circulated through it as will be discussed below. Figure 29 is a photograph of the interior of the empty test formation chamber showing the central aluminum tube (borehole) and the sonde mockup stainless steel case in the sidewall configuration. Thermocouples are positioned along the spring-loaded aluminum rod pressing against the outside of the aluminum tube and the inside surface of the test formation container. All tne inside surfaces were painted with high temperature aluminum paint.

The test formation container and attached heaters are covered on all sides by thermal insulation (ETR board). This essentially eliminates significant heat losses through the tank walls and facilitates heating of the test formation, greatly reducing the time between temperature changes.

Provisions have been made to circulate the "borehole fluid" (water or water boric acid solution) through the borehole and into a retainer tank as shown schematically in Figure 28. Alternately the fluid can be circulated through a heat exchanger prior to entering the borehole to simulate the situation generally encountered in geothermal wells where the temperature of the borehole fluid is generally lower than that of the formation.

2.4.2.2 Sonde Mockup

The arrangement of the neutron source and He-3 detectors incorporated in the sonde mockup is presented schematically in Figure 30. It consists of the various component shown, located inside the three-inch (7.6 cm) outside diameter (type 304) stainless steel tube. The position of the mockup in the test stand is shown in Figures 28 and 29. The diameter was selected to correspond approximately to that of standard

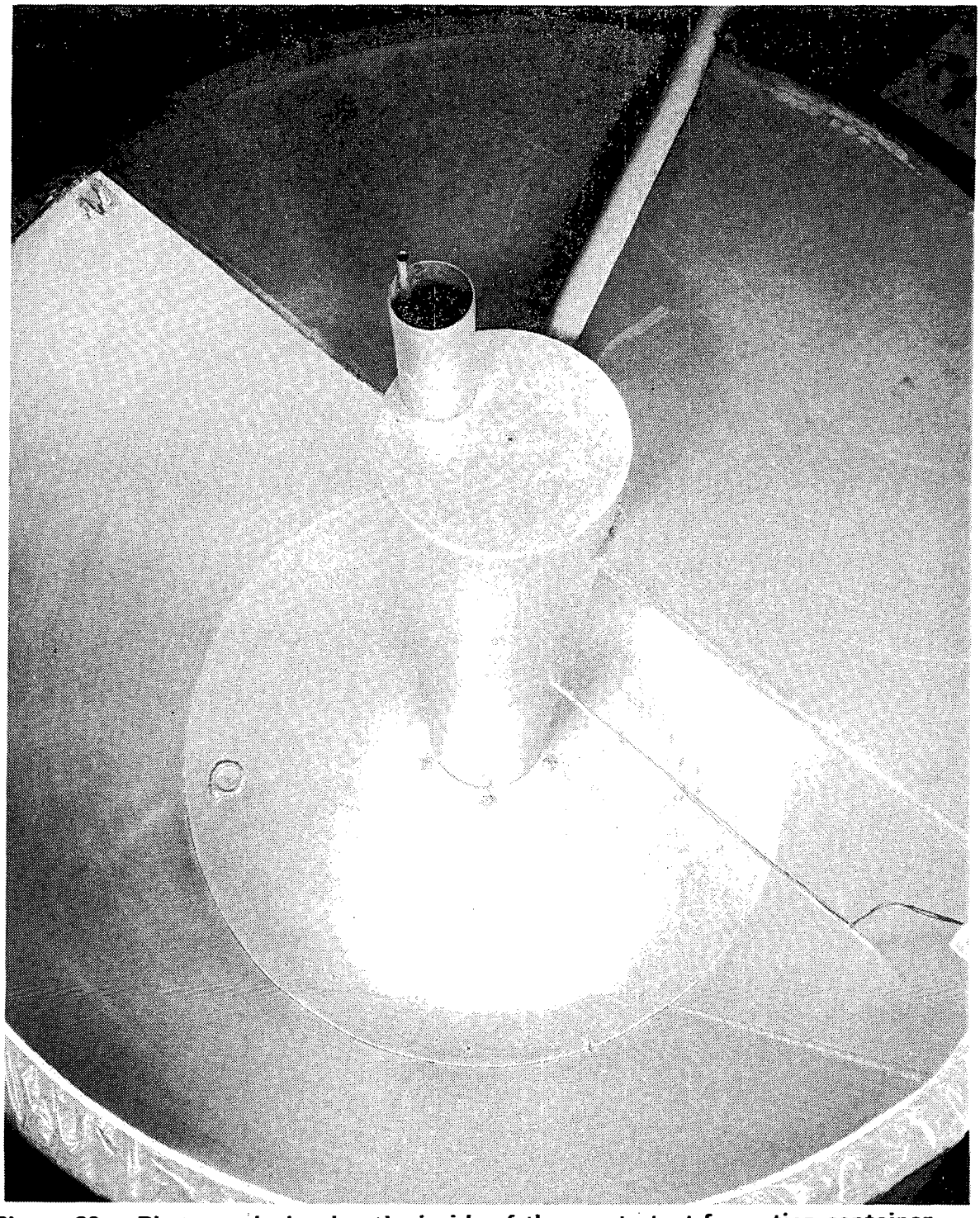

Figure 29. Photograph showing the inside of the empty test formation container. Thermocouples are attached to the spring-loaded bar between the central tube and the chamber wall.

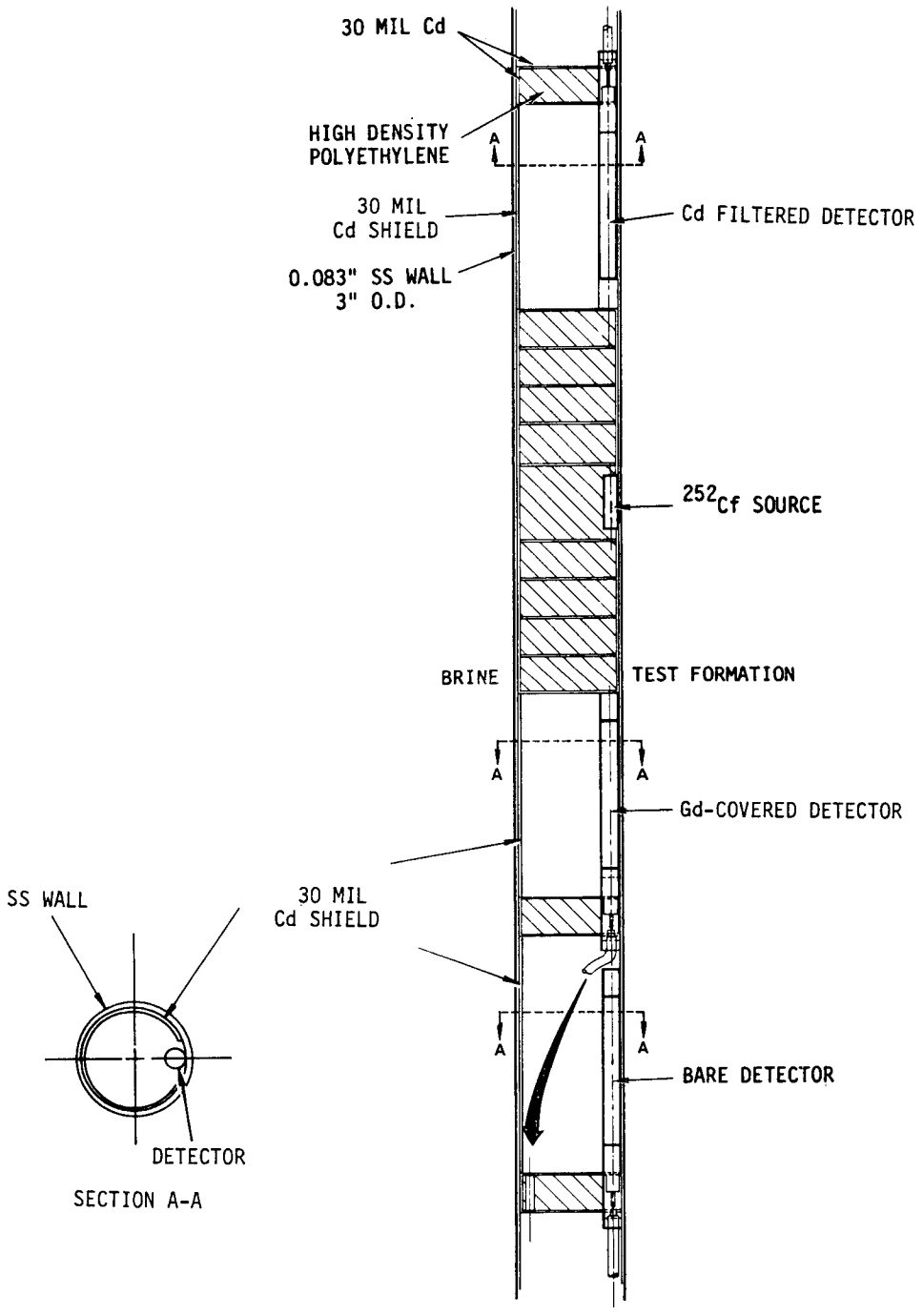

Figure 30. Sonde mockup configuration used for evaluation of the formation temperature sensor. Support members, i.e., two 1/4" DIA SS rods and aluminum clamping devices, are omitted for clarity. These are designed to allow flexibility in positioning the components shown in the drawing relative to each other and to permit changes in the polyethylene/30 mil Cd shields.

downhole tools used in uncased oil wells. The diameter of such instruments is 3 5/8 inches (9.208 cm). The wall thickness of the tube is 0.083 inches (0.211 cm). The various sensor components are supported by two 1/4-inch(0.64 cm) diameter stainless steel rods, and they are positioned along the rods by aluminum support/clamping devices shown in Figure 31. Support members are omitted from the drawing in Figure 30 for clarity and only the essential features of the device are shown.

The Cf-252 source is located inside a cavity in a polyethylene/Cd cylindrical structure (source shield) at a position such that it will be next to the borehole wall when the instrument is sidewalled and properly oriented. The polyethylene/Cd source shield is designed to minimize the number of source neutrons emitted directly into the borehole. This is accomplished by slowing down of fast source neutrons in the polyethylene (high hydrogen content material) regions of the shield and subsequent absorption in the various 30 mil Cd layers and the surrounding 30 mil thick Cd cylinder. Consequently, only a small fraction of the source neutrons which would have been emitted directy into the borehole in the absence of the shield actually reach the borehole fluid when the source shield is used. The overall length of this shield is 10.3 inches (26.16 cm).

The three He-3 detectors used are the RS-P4-0404-207 counters discussed in subsection 2.2. Of the three detectors shown in Figure 30, one is surrounded by a 30-mil (0.076 cm) thick cadmium (Cd) sleeve, another is surrounded by 2-mil (0.005 cm) thick gadolinium (Gd) foil, and the third is bare (unfiltered). The neutron transmission of the filters and the response of the various filter/detector combinations have been discussed (subsection 2.1). The Gd-filtered and Cd-covered detectors are located closer to the source each at an equal distance from it. The bare detector is located further from the source as shown in Figure 30. The filtered detectors are placed closer to the neutron source because of the lower count rates expected due, obviously, to absorption in the Gd and Cd filters. All three detectors are aligned with one another and with the source so that all three detectors and the neutron source are adjacent to the borehole wall when the test sonde is sidewalled and properly oriented.

The remaining three polyethylene/CD shields (each $\sim$1.06 inches or 2.69 cm thick) and the 30-mil (0.076 cm) Cd shields are designed to provide additional shielding of the detectors against neutrons which thermalize in the borehole fluid near the detectors. Although the source shield largely reduces the number of source neutrons directly emitted into the borehole, it does not prevent neutrons which are initially emitted into

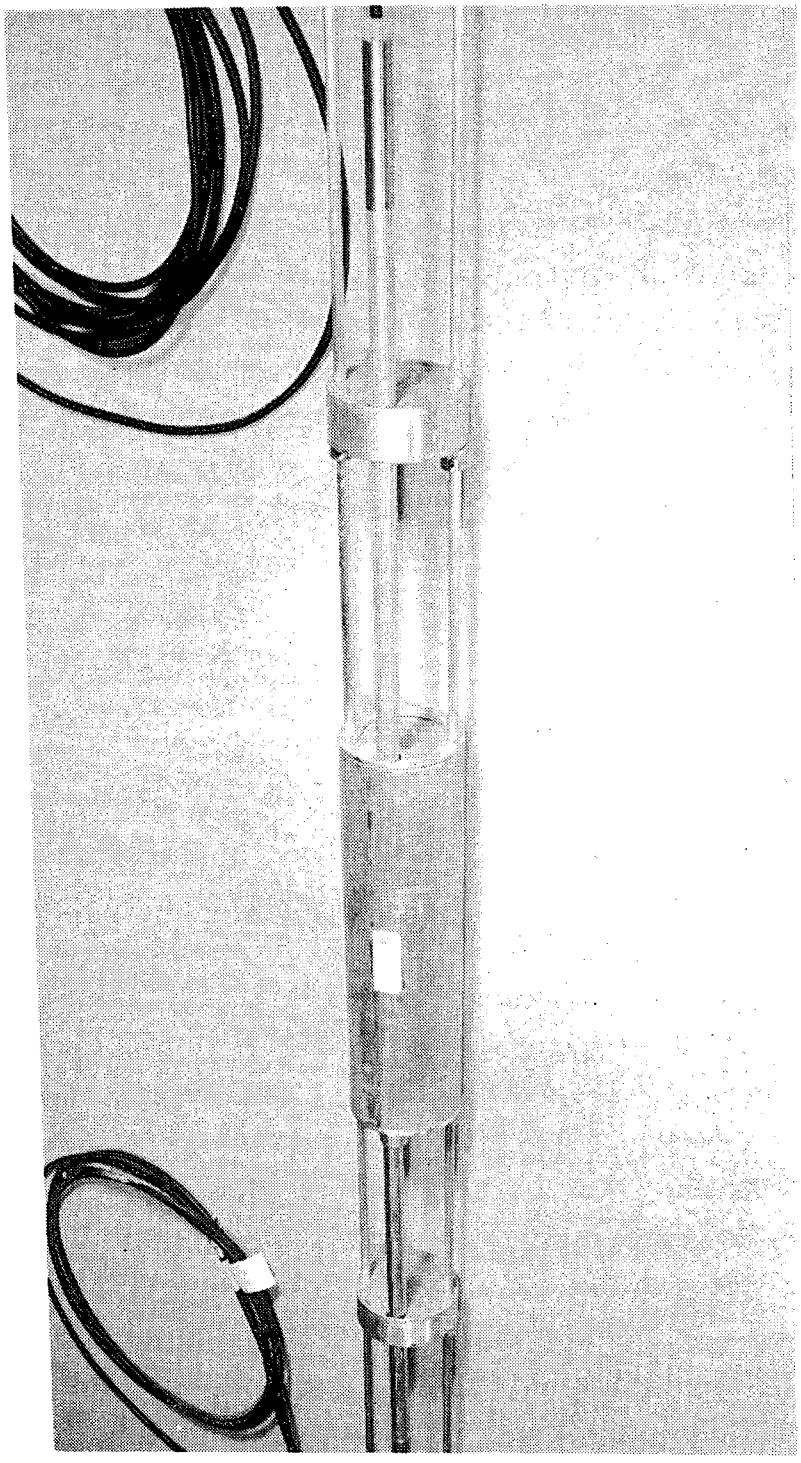

Figure 31. Partial photograph of the sonde mockup showing the structural devices used to position and support the various sensor components. The He-3 detectors used in the mockup are six inches long. The detectors shown here are the twelve-inch long detectors used for the preliminary measurements.

the formation from scattering (or diffusing) into the borehole. Such neutrons could thermalize (or rethermalize) there, and in the absence of the above shields they could eventually reach the detectors causing undesirable interference, i.e., modification of the gauge response to conditions in the test formation. The 30-mil Cd shields cover the inside of the sonde mockup in the region of the detectors leaving slots at the detector positions, as shown by the section drawing in Figure 30, so that only thermal neutrons from the test formation can reach the detectors unhindered.

The above test device has been designed to permit changes dictated by the results of the planned evaluation experiments. The source-to-detector distances can be changed easily and rapidly. The shield dimensions and configuration can also be changed readily. High density polyethylene can be replaced readily by another equally effective substance (with high hydrogen content), e.g., glycerine in appropriate containers, if it becomes necessary for later, higher temperature measurements. The initial evaluation of the above system was performed in water test formations ($T < 100^{o}C$). In this case high density polyethylene is a most convenient moderator to use from the point of view of ease in fabrication and design modification.

2.4.2.3 Initial Measurements

Measurements were performed using the sonde mockup described above in the test stand described at the beginning of this subsection. These measurements consisted of counts obtained with the three detectors simultaneously at each temperature of the test formation and for various conditions in the borehole. The test formations were water and a water boric acic solution containing a concentration of H_3BO_3 which is equivalent to 2.4 weight percent concentration of NaCl. The borehole conditions were:

1. Borehole full of water at the temperature of the test formation.
2. Borehole full of water at a temperature lower than that of the test formation.
3. Borehole empty.
4. Borehole full of water boric acid solution at the temperature of the test formation. The boric acid concentration used was equivalent to 3.5 weight percent concentration of NaCl.
5. Borehole full of water boric acid solution at a temperature lower than that of the test formation.

An ~8 g Cf-252 neutron source was used for these measurements. This yielded counts in the range of 400 counts per second for the Cd-covered detector, 550 counts per second for the Gd-filtered detector and 60 counts per second for the bare detector when the borehole was full. With the borehole empty the observed count rates were in the range of 670, 850, 650 counts per second for the Cd-covered, Gd-filtered and bare detector, respectively.

It should be recalled that the bare (unfiltered) detector was located further from the neutron source than the filtered detectors (Figure 30). The observed bare detector counts were corrected to compensate for this difference. The correction involved multiplying the observed bare detector response by the ratio of counts obtained with the bare detector at the two (short and long) source/detector distances. Next, the Cd-covered detector counts were used to correct both the Gd-filtered and the compensated bare counts. Finally, the ratio, R, of the corrected Gd-filtered-to-bare detector counts was computed at various temperatures and for the above test formation and borehole conditions.

Results of measurements made with water as the test formation are presented in Figure 32. R is the ratio of the Gd-filtered-to-bare (unfiltered) detector counts. The various data points represent measurements made with the borehole full of water at the temperature of the test formation (full circles), at a temperature lower than that of the test formation by the number of degrees shown (full triangles), and with the borehole empty (open circles). The agreement between the data obtained under the various conditions in the borehole indicates that the sensor response is determined essentially by conditions in the test formation.

Next, measurements were performed with water as the test formation, but with a water boric acid solution as the borehole fluid. The concentration of boric acid used in the present measurements is equivalent to 3.5 weight percent concentration of sodium chloride in the brine. The data obtained are shown in Figure 33. Measurements were performed with the borehole full of water boric acid solution at the temperature of the test formation (full circles) and at a temperature lower than that of the test formation by the number of ^{o}C shown (full triangles). The broken line curve in this figure represents the response observed with water as the test formation and with water also as the borehole fluid. The effect of the above concentration of boric acid (or the

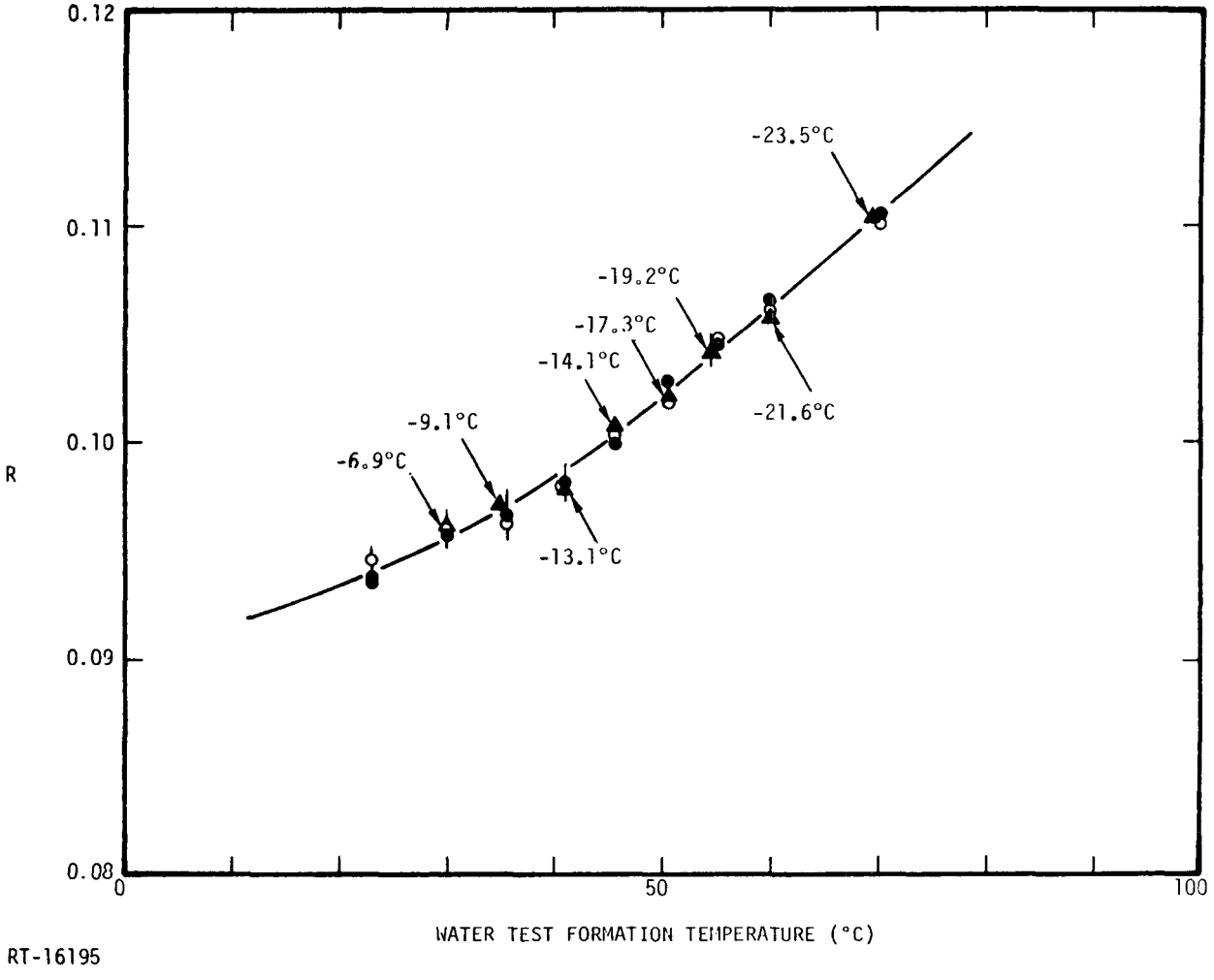

Figure 32. Data obtained with the sonde mockup. R is the ratio of the Gd-filtered to bare detector counts after correction for the 1/E contribution. The test formation is water. Data are shown for the borehole empty (○), the borehole full of water at the temperature of the test formation (●), and at a temperature lower by the number of degrees given (▲).

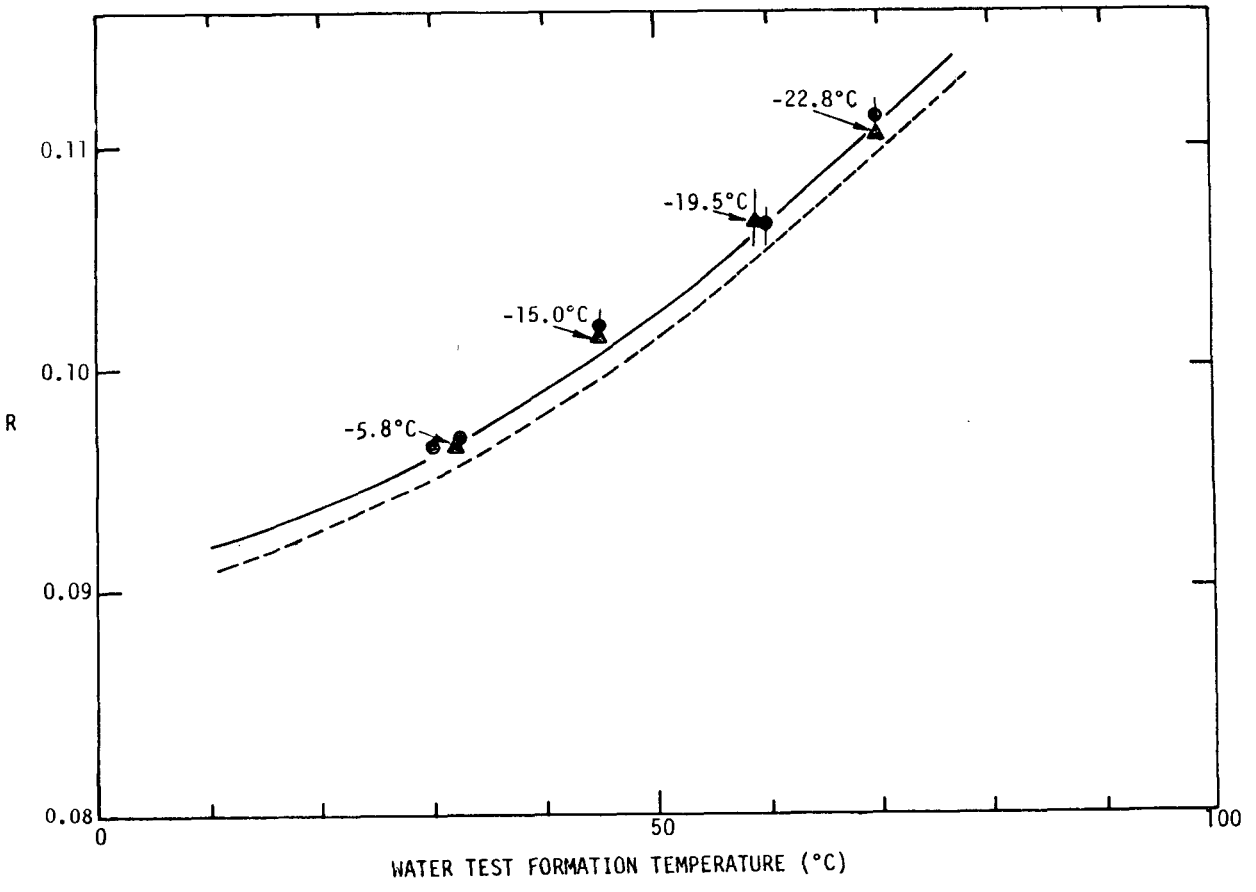

Figure 33. Data obtained in water test formation with water boric acid solution as the borehole fluid. R is the ratio of the Gd-filtered to bare detector counts after correction for the 1/E contribution. Data are shown for the borehole full of water at the temperature of the test formation (●), and at a temperature lower by the number degrees given (▲). The broken line is the sensor response obtained with water as the borehole fluid.

equivalent sodium chloride concentration) in the borehole fluid is about a one percent increase in the sensor response, R. This is small (at least by one order of magnitude) compared to the effect of the same concentration of absorber in the test medium as observed in our preliminary measurements. The above data indicate that the effect of borehole fluid salinity on the sensor response is small (for generally encountered salinities). It will be shown below that the borehole fluid salinity does not affect the determination of the formation temperature. It only modifies the effective neutron absorption cross section of the moderating medium in the vicinity of the sensor.

Following the above measurements in water, measurements were performed with a water boric acid solution as the test formation. The data obtained with water as the borehole fluid and with the borehole empty are shown in Figure 34. The various symbols represent the borehole conditions discussed previously (Figure 32). Curves 1 and 2 are the observed response shown in Figure 33 and are included in this figure to facilitate comparison. The higher count ratios observed with increased absorption are in agreement with the results of the preliminary measurements. Unlike the data obtained with the water test formation (curve 1 and Figure 32), it appears that the count ratio, R, values obtained with the boric acid solution test formation and with the borehole empty are somewhat lower than the corresponding ratios observed with the borehole full. This difference ($\sim$2.5 percent) may not be significant. It is very sensitive to the factor used to compensate the bare detector counts for the greater distance of this counter from the neutron source. In the above case, $\sim$1 percent change in the factor used would bring the empty and full borehole responses into agreement. This may be a weakness of the present method of computing the ratios and alternative methods should be examined. One such method would compensate the Cd-covered detector response for the longer source/detector distance in order to correct the bare detector counts for the 1/E contribution. According to this method, the bare detector counts will not be corrected for the source/detector distance, and, as a result, the computed, 1/E-corrected Gd-filtered-to-bare detector count ratios would be an order of magnitude (20 to 30 times) higher than the corresponding values obtained by the present method. In retrospect, the above alternative approach is statistically more attractive and it should be examined. The present method was used largely in order to allow a more direct comparison of the well geometry results with the results of the simple geometry, preliminary measurements.

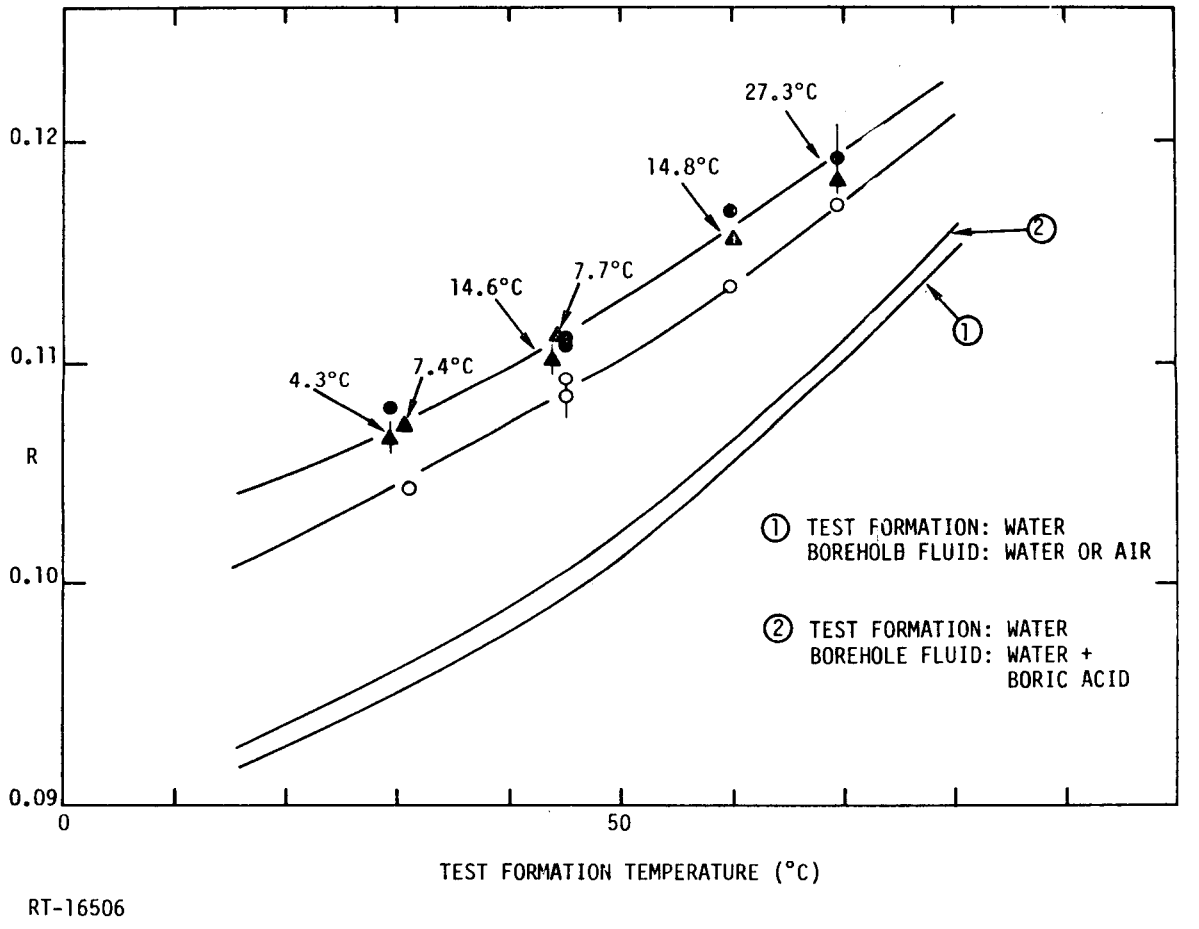

Figure 34. Data obtained in water boric acid solution test formation with water as the borehole fluid. R is the ratio of the Gd-filtered to bare detector counts after correction for the 1/E contribution. Data are shown for the borehole empty (○), the borehole full of water at the temperature of the test formation (●), and at a temperature lower by the number of degrees given (▲). The lower line curves are the sensor response shown in Figure 33.

The final set of measurements in the present phase were performed with water boric acid solution (2.4 weight percent equivalent NaCl concentration) as the test formation, and water boric acid solution (3.5 weight percent equivalent NaCl concentration) as the borehole fluid. Again the response of the sensor obtained previously under various conditions is included for ease of comparison. As in the case of the data obtained with water as the test formation, the count ratio, R, observed with increased neutron absorption in the borehole fluid (increased fluid salinity) result in slightly higher ratios. The increase in this case is $\sim$1.75 percent and as in the case of the water test formation it will not affect the determination of the formation temperature.

The plots of the formation temperature gauge response presented in Figure 35 clearly show that the observed trend in the initial well geometry data is the same as that observed in the preliminary, simple geometry experiments (Figure 23). The well geometry data presented in this section constitute points in a single plane of the three dimensional space discussed earlier. The Cd-covered detector counts are constant for all the well geometry data presented. $C_{Cd} = 394 \pm 2$ counts per second with the borehole full and $C_{Cd} = 648 \pm 3$ counts per second with the borehole empty. This difference in C_{Cd} and similar differences in the count rates recorded by the Gd-filtered and the bare detectors can be eliminated by normalization of the observed count rates to the corresponding count rates obtained with a particular test formation at one specific temperature. The present data were normalized to the observed detector count rates for the water test formation at 31.0°C with and without water in the borehole. Under these conditions $C_{Cd_{th}} = C_B^{th} = 1.0000$ both with the borehole full of water and with the borehole empty. C_{Gd}^{th} is equal to the value of R corresponding to the condition in the borehole. The Cd-covered detector count rates normalized in this manner average 0.9988 ± 0.0036 and 0.9959 ± 0.0024 for all the full and empty borehole measurements respectively. The average normalized C_{Cd} for all measurements regardless of the conditions in the borehole is 0.9973 ± 0.003.

The normalized data are presented in Figure 36. This is a mapping of the count ratios observed under the various conditions discussed in the preceding paragraphs and the corresponding normalized Cd-covered and bare detector counts. Just as the preliminary data obtained for the various water-boric acid solutions, Figure 25, the present data all lie in a plane of the three dimensional mapping of R, and the normalized C_B^{th} and C_{Cd}. Furthermore, it is clear that the higher count ratios obtained with increased borehole fluid salinity, curves 2 and 5 in Figure 36, do not affect the

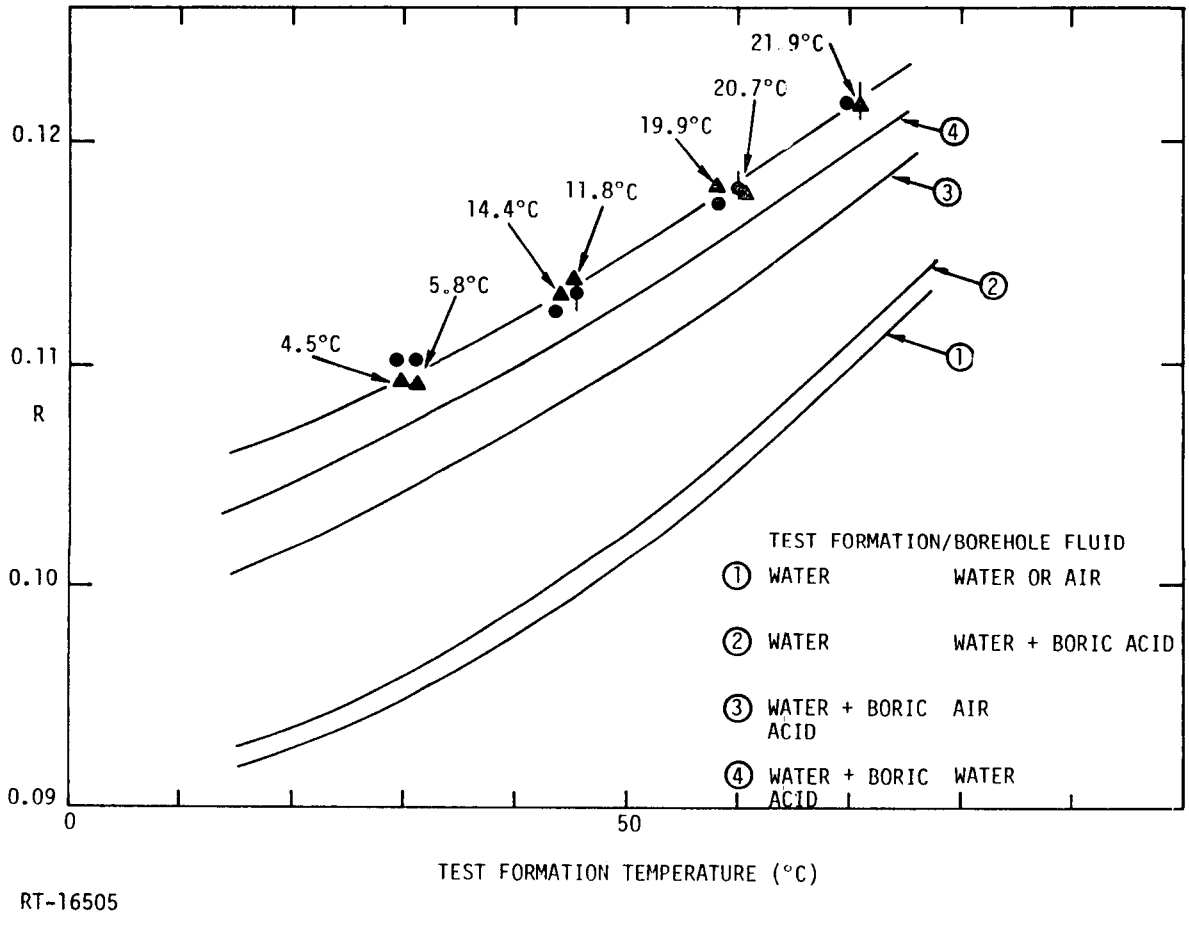

Figure 35. Data obtained in water boric acid solution test formation with water boric acid solution as the borehole fluid. R is the ratio of the Gd-filtered to bare detector counts after correction for the 1/E contribution. Data are shown for the borehole full of fluid at the temperature of the test formation (●), and at a temperature lower by the number degrees given (▲). The curves represent the response of the sensor shown in Figures 33 and 34. They are included for comparison.

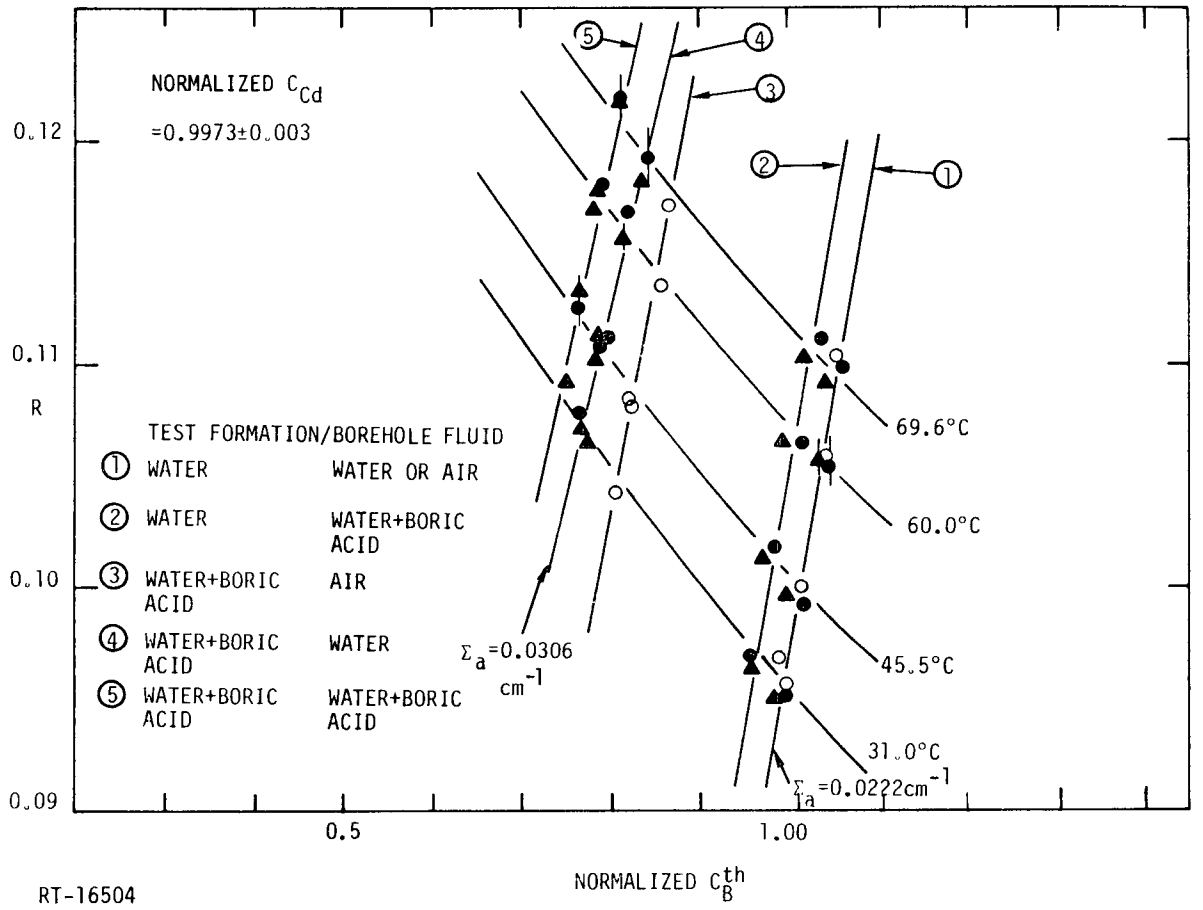

Figure 36. Mapping of the count ratio, R, as a function of the normalized bare detector counts for various conditions of the test formation and borehole fluid temperature and neutron absorption cross section (salinity), but for constant neutron moderating power. Data are shown for the borehole empty (O), the borehole full of water or water boric acid solution at the temperature of the test formation (●), and at a temperature lower than that of the test formation (▲). The formation temperature is uniquely determined regardless of conditions in the borehole.

determination of the formation temperature since the data points obtained lie on the equal-temperature curve corresponding to the formation temperature. The same is true of the empty borehole data, curve 3. The effect of borehole fluid salinity and/or fluid density appears to be a modification of the effective neutron absorption cross section, Σ_a, in the vicinity of the gauge. The significant facts are that the temperature determination is unique and that the temperature determined is that of the formation regardless of the borehole conditions considered. The above effects on Σ_a could be taken into account in the sensor calibration.

2.5 PRELIMINARY CONCEPTUAL DESIGN OF A FORMATION TEMPERATURE SONDE

Having demonstrated the scientific feasibility of the neutron technique for the determination of the formation temperature, a conceptual design of a formation temperature sonde and logging system was developed. Performance specifications were estimated on the basis of available information. These are discussed in the following paragraphs.

2.5.1 Estimates of Performance Specifications

Performance specifications have been estimated for the system which will be described below on the basis of data obtained in the present study and from relevant literature. These specifications are listed in Table 2. Obviously, the primary parameter to be determined is the formation temperature. However, the neutron absorption cross section, Σ_a, of the formation can also be determined as described previously from a mapping of the gadolinium-filtered-to-bare detector count ratio as a function of the bare detector counts. Σ_a together with the corresponding cadmium-covered detector counts can be used to estimate the saturated porosity of the formation. The temperature determination accuracy estimates listed are based on the above feasibility study data. The main contribution is due to counting statistics (50 to 75 percent), but they also include a contribution due to systematic uncertainties. Since the detection system used was not optimum and the source strength was rather low, these accuracy estimates may be rather conservative.

A possible limitation to the applicability of the present technique may be a very high absorption cross section of the moderating medium. As Σ_a of the moderator increases the Maxwellian portion of the moderated neutron energy spectrum decreases

Table 2. Estimated Performance Specifications for the Formation Temperature Sonde

1.	Primary parameter measured Additional information obtained	Formation temperature Neutron absorption and moderation (saturated porosity). (Section 2.4.1.2)
2.	Estimated technique accuracy	$\pm 3.5^{o}C$ near room temperature $\pm 2^{o}C$ at $T \gtrsim 100^{o}C$ (Section 2.4.1.5).
3.	Neutron absorber concentration limit	Technique applicable in all known liquid dominated hydrothermal systems; inapplicable when dissolved mineral content becomes 7 to 10 times that of Salton Sea KGRA.[a] Technique inapplicable in completely dry formations with absorber concentrations resulting in cross sections equivalent to that of 25 percent the Cl^{-} concentration of Salton Sea KGRA.
4.	Temperature limitations	No inherent technique limitations. He-3 detectors are designed to operate at $\lesssim 260^{o}C$.[b] Electronic component operating temperature range is presently the limiting factor. High temperature multiconductor cable successfully tested at $\lesssim 260^{o}C$.[c]
5.	Logging mode	Continuous or step by step
6.	Maximum logging speed	25 to 50 ft/min continuous logging 20 to 70 ft/min step-by-step logging
7.	Source strength	50 to 150 μg Cf-252
8.	Depth of penetration	5 to 10 inches[d]
9.	Borehole effects	Minimized by sidewalling and neutron shielding design. (Section 2.4.2.2)

[a] Estimated from published values of Salton Sea brine salinities.

[b] Reuter-Stokes, private communication.

[c] Sandia geothermal well logging cable.

[d] References 3 and 4.

because of preferential absorption of neutrons in the lowest energy (thermal) range. However, this is the portion of the neutron energy spectrum which is sensitive to the medium temperature, T, via the parameter T_n (neutron temperature) which characterizes the Maxwellian. $T_n = T_n (T, \Sigma_a, \xi\Sigma_s)$ (Equation 2). Therefore, for a medium with moderating power $\xi\Sigma_s$, there exists a value of Σ_a, or concentration of absorber, above which T_n cannot be used to describe the thermal neutron energy spectrum. In this range, T_n is no longer a valid parameter because the thermal neutron spectrum can no longer be represented by a Maxwellian function. Therefore, the technique is only applicable in media with $4\ \Sigma_a/\xi\Sigma_s \lesssim 1$ (Ref 12). The range of applicability listed in Table 2 was estimated assuming a fifteen percent porous silica matrix. Since the salinity of hot water fields is generally $\lesssim 12$ percent that of the Salton Sea field, the technique should be applicable in all known liquid dominated hydrothermal systems. The reason for the lower absorber concentration limit in the completely dry matrix is the very low moderating power of this medium due to the lack of moisture content. Since even the hot "dry" rock resources are not free of moisture or bound water, the technique should be applicable in hot dry rock formations with a much larger range of absorber concentrations than the listed estimate for the completely dry matrix ($\xi\Sigma_s$ increases very rapidly with increased moisture content).

There is no inherent temperature limitation on the technique itself in the range of $4\ \Sigma_a/\xi\Sigma_s$ in which the method is valid. In this range of moderator properties, it will be applicable for temperatures even higher than may be encountered in magmatic and other long-range applications, i.e., 1000 to 1100°C. Temperature limitations, however, do exist at the present time with respect to the instrumentation. He-3 detectors can presently be operated at temperatures $\lesssim 260$°C. Reuter-Stokes (a major supplier of neutron detectors) claims that extension of the operating temperature range to ~ 325°C may possible with some redesign. The main limitation in achieving the DOE short range goal of tool operational capability at $\lesssim 325$°C may be posed by the operational temperature characteristics of presently available electronic components. It is interesting to note, however, that the maximum advertised temperature of neutron logging tools used by the oil industry is 260°C. The final temperature limited component is the logging cable. Sandia now owns what is considered the best currently available multiconductor (seven conducting wires) cable. It has been tested successfully at temperatures $\lesssim 260$°C.

Logging with the formation temperature sonde now envisioned could be either continuous (tool in continuous, uniform motion throughout the logging operation) or step-by-step (tool stationary while the detectors are counting). In the continuous mode of operation, the response will obviously be averaged over the well section traversed in a counting interval. Since the average expected temperature gradients will be $\lesssim 0.023^{\circ}C/ft$ ($75^{\circ}C/km$), this will not generally be a limitation. The tabulated logging rate estimates are based on these expected average temperature gradients and on a required precision similar to that obtained in the feasibility measurements. These rates are comparable to typical logging rates in oil wells (10 to 50 ft/min). They are reasonable in the absence of sharp temperature anomalies. Such regions should be logged at lower speeds consistent with locally higher gradients.

The penetration depth into the formation is a question which needs to be addressed specifically with regard to the temperature measurement. It will depend on the moderating power, $\xi\Sigma_s$, of the formation and the source/detector distances. The tabulated values are appropriate to neutron-neutron porosity sondes in water saturated sand formations, and particularly to the IRT uranium logging system which is thermal neutron dominated as is the case with the formation temperature sonde. Values of the same order would be expected for the temperature sonde.

2.5.2 Conceptual System Layout

A preliminary conceptual design of a logging system with the above performance specifications will be described below. In formulating this concept, use was made of experience gained in the development (design, fabrication, and testing) of the IRT uranium logging system under a separate DOE contract. As a result, many of the subsystems developed under that program could be transferable to the formation temperature logging system with only minor modifications.

Figure 37 presents a schematic overview of the logging system. All of the essential subsystems are shown and the labels are generally self-explanatory. These are the standard components of a borehole logging system except perhaps for the source cask and the sonde and cask support. The cask which will be stored inside the logging truck prior to and following a logging operation will be used to store the neutron source when logging is not being performed. It will be designed so as to absorb the source radiation while the source is in storage. Furthermore, the source will be transferred directly from the storage cask to the sonde and back prior to and after a logging

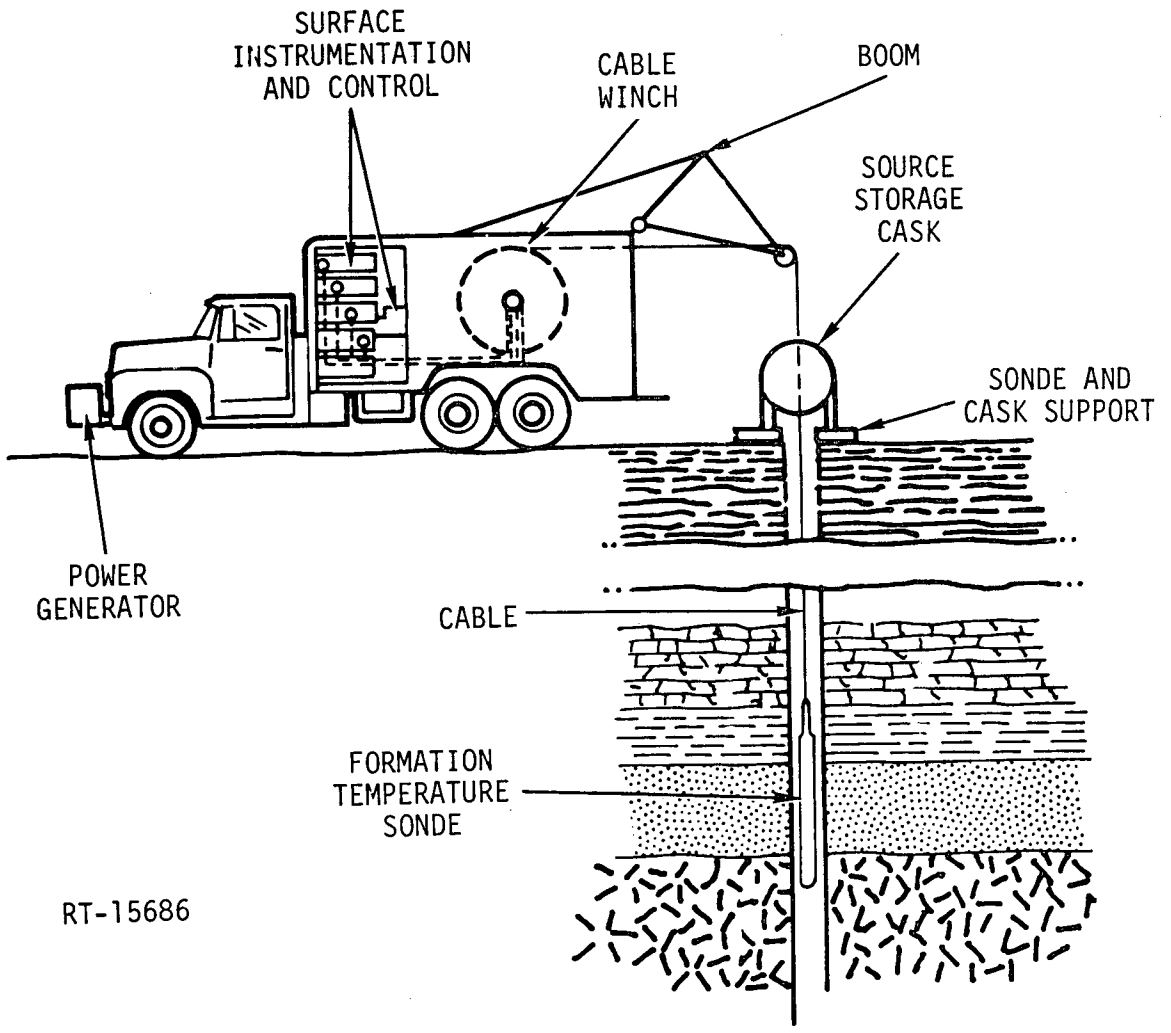

Figure 37. Schematic overview of logging system hardware

operation in order to minimize exposure of the operating personnel to radiation to a level below the maximum allowable dose. This requires that the cable pass through the middle of the cask as shown in Figure 37. The sonde and cask support will serve as a firm support base for the storage cask during logging and as a holding device for the sonde during source insertion and removal prior to and following well logging operations. The cask and sonde support will be designed to accomodate the tubing and valves in place over the well. The surface instrumentation and control subsystem will include all the surface electronics, and data processing and display equipment. The generator (gasoline powered) will power the surface and downhole (sonde) electronics.

A conceptual layout of the sonde is shown in Figure 38. The insertion/retrieval mechanism will be used in the process of inserting the neutron source into or removing it from the sonde. It will also make possible retrieval of the source in the event the sonde becomes permanently lodged in a well. The in-sonde storage source position designates the source location immediately after the insertion into or prior to removal from the sonde. It will also be the source position during neutron detector checks for stability, electronic noise and background levels. Prior to the start of the logging process, the source will be moved from its in-sonde storage to the logging source position in the neutron detection sonde subsystem which also contains the neutron detectors with the associated filters and shields. The associated detector high voltage (H.V.) supplies and counting electronic will be located together with the logic and downhole signal handling components immediately below the source storage region. A temperature sensor will be used to monitor temperature inside the sonde. This information should be useful in the interpretation of data.

The electronics can be grouped into the downhole and surface subsystems. Figure 39 represents a block diagram of the downhole electronics. These consist of the He-3 neutron detectors and their associated counting electronics, power supplies, switching, logic, and data and command handling circuits. The He-3 neutron detectors consist of one bare counter, ^{3}He3, one covered with gadolinium, ^{3}He2, and one covered with cadmium ^{3}Hel. Each detector will be connected to a H.V. supply and its signal will be capacitively coupled to the input of a charge sensitive preamplifier. Each detector will have its own amplifier, discriminator (or single channel analyzer), and scaler. The H.V. supply, however, will be common to all three. The preamplifier output is further amplified and shaped by the amplifier whose output is fed into the pulse discriminator. Its output is logic level pulses which are input to the scaler. Upon interrogation, the scaler content will be dumped for transmission. The scaler interrogation commands

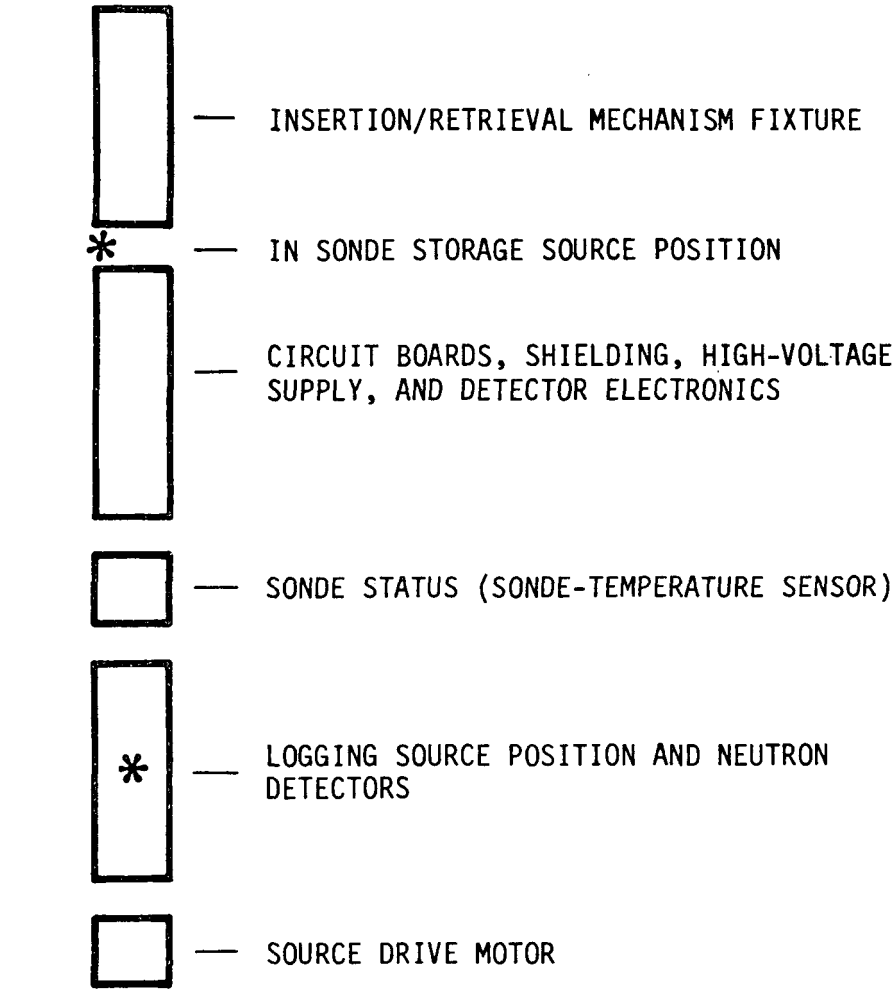

Figure 38. Conceptual layout of the formation temperature sonde subsystems

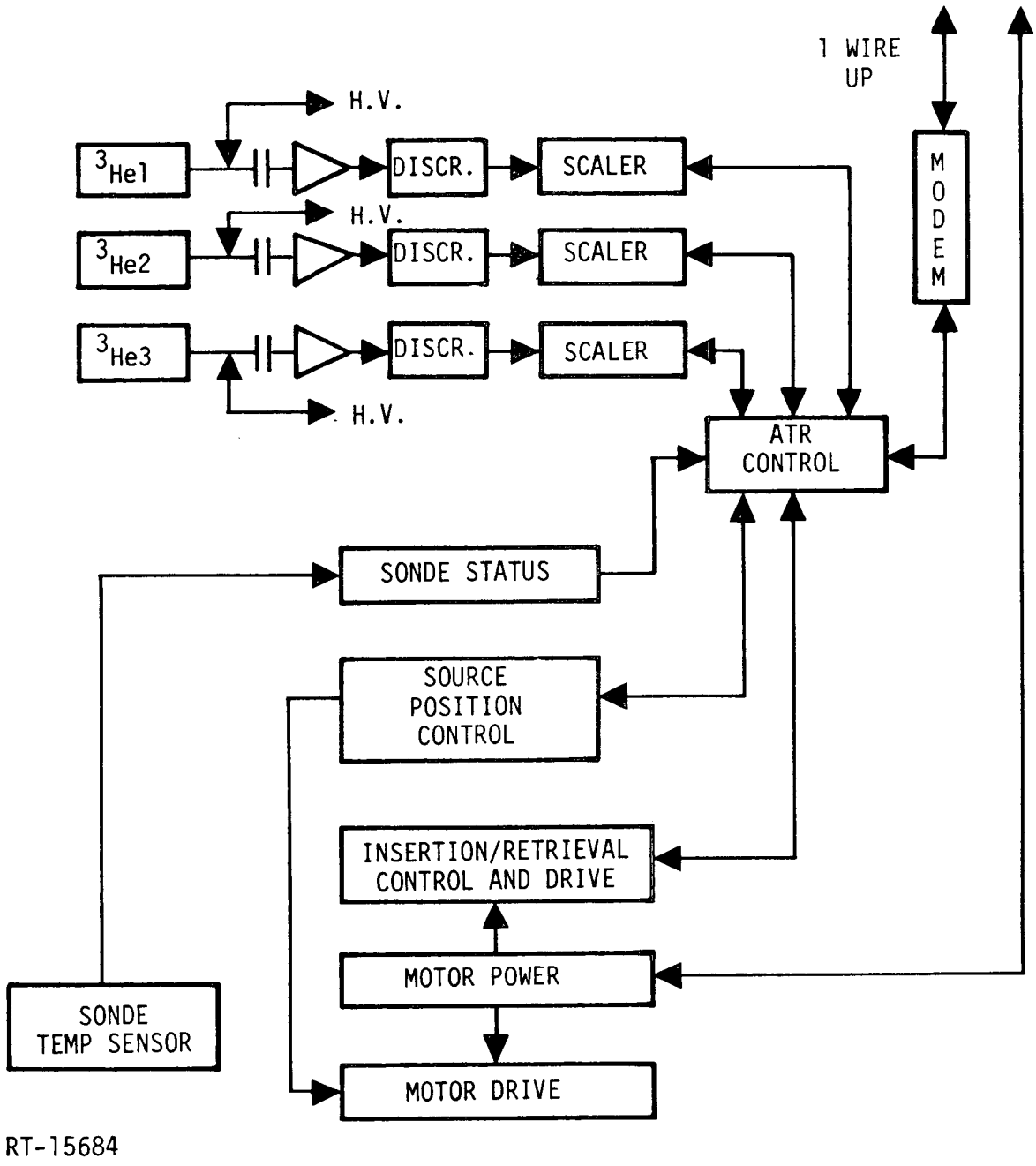

Figure 39. Block diagram of downhole electronics

from the surface controller will be transmitted into the sonde by an FM modem-ATR (asynchronous transmitter receiver). The modem-ATR circuit also controls insertion and retrieval of the source, source movement inside the sonde, and transmission of the sonde temperature sensor and source position data.

The analog signal from the downhole modem will be transmitted to the surface via the logging cable. At this point it will be processed by a second modem-ATR circuit as shown in Figure 40 which is a block diagram of the surface electronics. The output from the surface modem-ATR will constitute the input to the system control and data analysis subsystem. This will consist of a microcomputer with the associated interfaces and appropriate software, a plotter for visual display of the logging data, and a teletype/recorder for display of the data in printed form. The teletype will be the communication link between the operator and the system control. A tachometer/odometer will be used to monitor the position (depth) of the sonde. A block diagram showing the flow of data in the overall system and the relationship between various subsystems is presented in Figure 41.

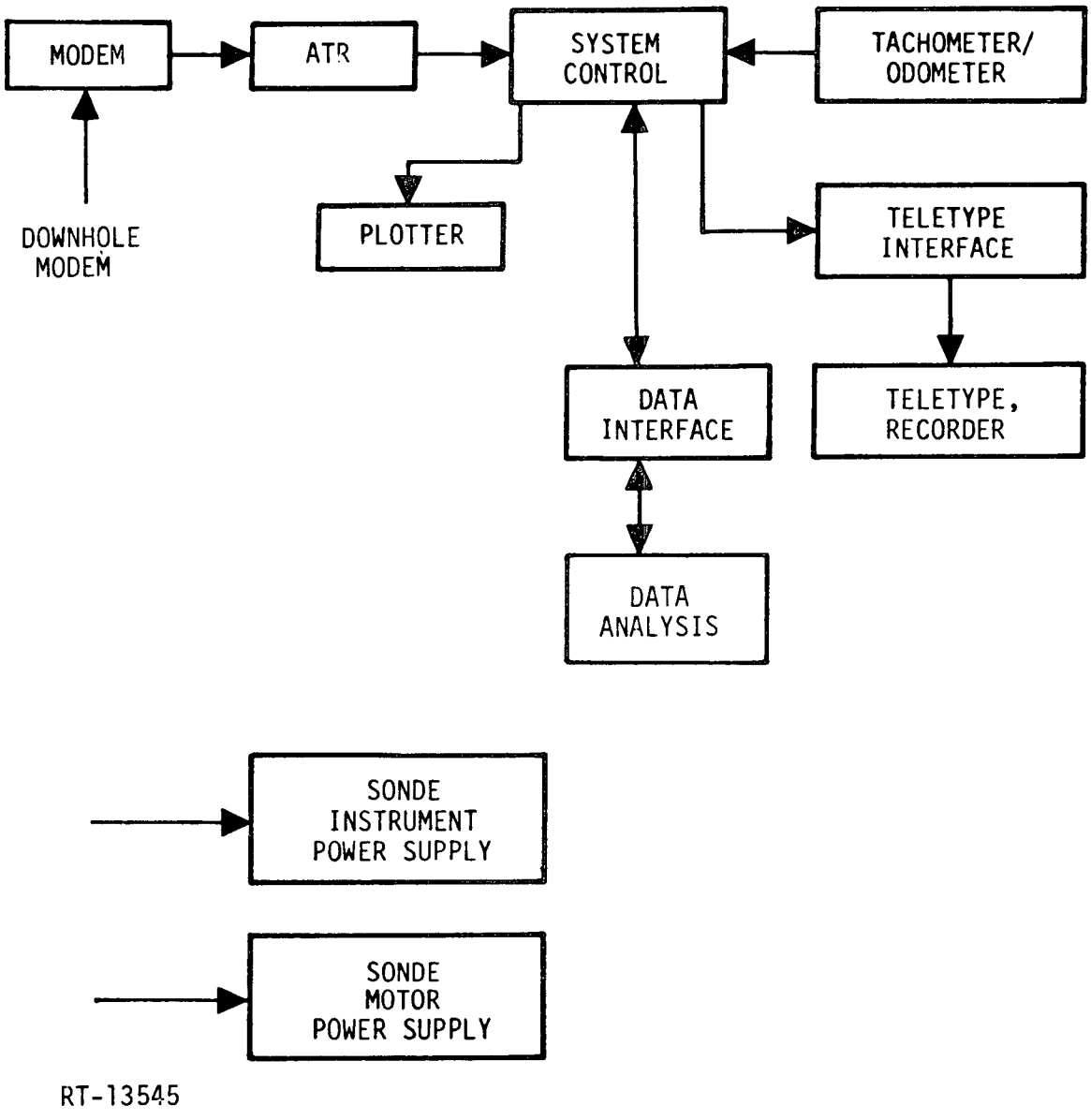

Figure 40. Block diagram of surface electronics

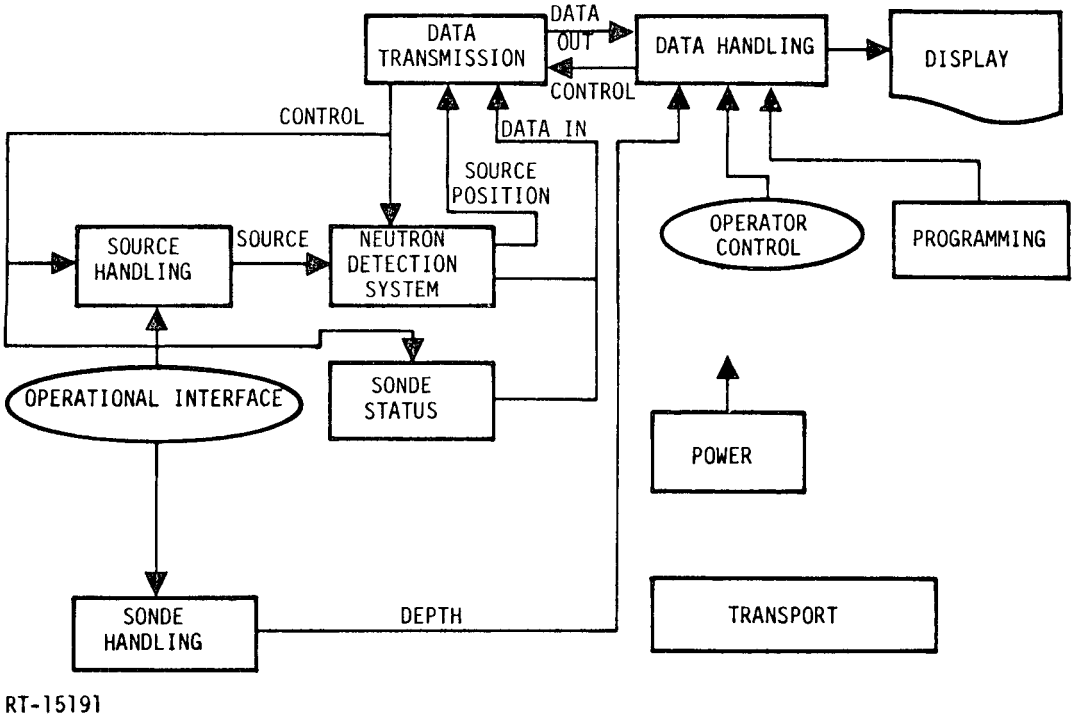

Figure 41. Schematic block diagram of system showing the flow of data and control between subsystems. Ballons are shown where operator control is required.

3. FEASIBILITY STUDY OF A NEUTRON ACTIVATION ANALYSIS BRINE FLOW METER

In addition to the study of the neutron formation temperature sensor, a rather brief study of the applicability of neutron activation analysis (NAA) techniques for the determination of two-phase fluid flow downhole has also been performed as part of the present program. This consisted of an analytical evaluation of various techniques. The methods and the results of the analysis are discussed below.

3.1 NEUTRON ACTIVATION-BASED FLOW RATE DETERMINATION

The results of computational analysis of NAA techniques for the determination of fluid flow rates inside a geothermal well bore are presented in this section. The techniques examined are based on in-situ activation by a Cf-252 neutron source in a sonde. Cf-252 is particularly suitable for geothermal applications because of the simplicity of design and the ability to withstand the severe environment. An appropriately designed neutron generator would be an alternative source. The activatable substances are among those found dissolved in geothermal brines. Activation occurs as the brine flows past the source. Detectors (in the sonde) located downstream from the source, monitor the density of the activated nuclei as they are carried past them by the flowing brine. Since the activated nuclei decay, with time each detector response depends on the source-to-detector transit time of the fluid, i.e., on the flow rate. This is a noncontact method which requires only that the fluid contain an activatable element. Therefore, it is applicable to two-phase fluid flow as long as each phase contains a proportionate amount of the activatable substance.

On the basis of the analysis presented in the following paragraphs, the methods examined appear to be feasible for vertical (along the bore axis) total mass flow rates $\lesssim 2000$ gal/min, or flow rates $\lesssim 450$ cm/sec in an eight-inch diameter borehole, and lateral (leakage in or out of the well) mass flow $\gtrsim 10^{-4}$ g/cm^2/sec. Experimental verification of the above is required to demonstrate the engineering feasibility of the technique.

3.1.1 Neutron Activation Analysis (NAA)

The methods make use of neutron activation analysis. That is, they involve production of unstable and/or excited nuclear species via neutron interactions with stable elements, and detection of gamma rays (photons) emitted in the subsequent decay and/or de-excitation to ground state, stable nuclei. The rate of production of the activated species depends on the affinity of the activatable nucleus for neutron capture and/or (neutron, particle) reaction, i.e., on the neutron activation cross section. The activated nuclide may be unstable and, thus, decay via electron (β^-, β^+) or particle (d, p, α) emission followed by the emission of a cascade of de-excitation photons. Alternatively, the activated nuclide may be metastable and, thus, decay via photon emission. In either case the activated nuclei decay at a characteristic rate, and the emitted photons have well-defined energies characteristic of the decaying nucleus. The decay rate of the nuclide is determined by its decay constant, λ, or its half-life, $T_{1/2}$. λ is defined as the probability that a nucleus which has not yet decayed at time, t, will decay before t+dt. $T_{1/2}$ is the time required for half of the active nuclides to decay.

$$T_{1/2} = \frac{\ln 2}{\lambda}$$

These constants are generally well known.

Although the gamma rays emitted by a decaying metastable nucleus or in the decay scheme of an unstable species have well-defined energies, the energy spectra obtained by gamma detectors generally consist of broadened peaks, due to the finite detector resolution, centered at the nominal gamma-ray energies superimposed on a continuum. The peaks result from deposition of the full energy of the detected photon in the sensitive region of the detector, while the continuum is due to partial energy deposition due to the finite size of the detector. Depending on the rate with which particular photons are emitted in the de-excitation cascade, corresponding peaks may or may not be distinguishable above the continuum. The peaks which are well resolved are conventionally termed prominent peaks. In many applications involving photon counting, it is possible to utilize the full energy spectrum i.e., count all events which result in some energy deposition (above background noise) in the detector, since each event, whether it results in full or partial energy deposition, represents one photon incident on the detector. In most cases, however, the photon energy spectra are very complex, and only those events are counted which result in total energy deposition.

This is not a limitation, since the probability that a photon incident on a detector will deposit its full energy inside the sensitive volume (detector peak efficiency) is known for standard detector configurations or can easily be obtained for special configurations. Both counting methods are used in neutron activation analysis.

3.1.2 In Situ Activation Method: Vertical Flow

In this section expressions are derived for the response of NAA systems applied to the determination fluid flow rates. Estimates of the systems' response are presented in the Tables and plots in subsections 3.1.2.1 and 3.1.2.2.

An expression has been derived for the density of gamma rays produced by a fast neutron source moving in an infinite water medium containing a concentration of certain activatable nuclei. It has been assumed that the source is at the origin of a cylindrical coordinate system (R = 0, z = 0) at time t = 0, and that it moves along the z-axis with a constant speed v for times $t>0$. Furthermore, the source emits no neutrons at $t< 0$, but has a strength S neutrons/sec at $t \geqslant 0$. Under these assumptions, the induced density of photons with energy E_γ, due to neutron capture by or particle reaction with the activatable nuclei and subsequent emission of de-excitation photons, is given by

$$\rho_\gamma(R, z, v, t) = S \cdot R \cdot \lambda \cdot \sigma_a \; N_{A_X} \cdot \int_0^{t_r} \phi_{th}(R, z-vt') \cdot e^{-\lambda \cdot (t-t')} \cdot dt' \quad . \tag{20}$$

In this expression, R is the fractional yield of the photon with energy E_γ, i.e., the branching ratio; σ_A is the activation cross section, N_{A_X} is the atom density of the activatable nuclide; A is the atomic mass number, t_r is the time during which the source strength is S, and $\phi_{th}(R, z-vt')$ is the thermal flux at (R, z) at time t' in units of thermal neutrons/cm^2/sec/source neutron/sec. The thermal flux is used because thermal neutron activation has been assumed. A fast neutron flux can be substituted in its place for fast neutron activation. Since the spatial distributions of fast and thermal neutrons are similar, the following analysis is equally applicable to both fast and thermal neutron activation.

Exact, analytical solution of the neutron transport equations to obtain the spatial distribution of the neutron flux resulting from a point source in an infinite medium is not possible. Approximate solutions, however, have been carried out. The fluxes obtained under the various approximation schemes constitute satisfactory approximations to observed spatial distributions. In the present analysis, use has been made of the thermal flux expression derived on the basis of three-group diffusion theory by Prof. G. C. Summerfield. According to this theory

$$\phi_{th}(r) = \frac{A}{r}\left[a_1 e^{-\frac{r}{L_1}} - a_2 e^{-\frac{r}{L_2}} - (a_1 - a_2) e^{-\frac{r}{L_3}}\right] , \qquad (21)$$

where

$$r^2 = R^2 + (z-vt)^2 ,$$

L_i = average diffusion length of neutrons in the i^{th} energy group,

and

A, a_1, a_2, a_3 = constants determined by the neutron properties of the medium.

Substituting Equation 21 in the integral of Equation 20 results in an expression which can be evaluated only by numerical techniques. Since the region of interest, however, is an annular region, i.e., the space between the sonde and the borehole wall, $\phi_{th}(R,z)$ given by Equation 21 with the appropriate values of the constants for water was closely approximated by a Gaussian function in the region $3.5 \lesssim R \lesssim 10$ cm corresponding roughly to a three-inch diameter sonde and an eight-inch diameter borehole. The flux obtained in this manner was substituted in Equation 20 and upon integration the following expression was obtained for the induced photon density.

$$\rho_\gamma(R,z,v,t) = 6.32 \times 10^{-2} \cdot R \cdot \lambda \cdot \sigma_a \cdot N_{A_X} \cdot S \cdot \frac{1}{v} \cdot$$

$$e^{-\left(0.02\ R^2 - 12.72 \cdot \frac{\lambda^2}{v^2}\right)} \cdot e^{-\lambda \cdot (t - \frac{z}{v})} \cdot \qquad (22)$$

$$\cdot \left\{ \operatorname{erf}\left[0.14 \cdot (z + 25.45 \cdot \frac{\lambda}{v})\right] + \operatorname{erf}\left[0.14 \cdot (v \cdot t_r - z - 25.45 \cdot \frac{\lambda}{v})\right] \right\} .$$

Obviously, $t_r \leqslant t$, the equality corresponding to the case of continuous irradiation.

Equation 22 is exactly the same whether the source is in motion in a stationary medium as assumed above, or whether the source is stationary in a moving medium, as will be the case in a borehole where the fluid flows past the source. It is the relative motion which is important. If a point detector is positioned at a distance $z = \zeta$ downstream from the source and at $R = R_d$ it will be exposed to a photon density

$$\rho_\gamma(v,t) = 6.32 \times 10^{-2} \cdot R \cdot \lambda \cdot \sigma_a \cdot N_{A_X} \cdot S \cdot \frac{1}{v} \cdot e^{-\left(0.02 \cdot R_d^2 - 12.72 \cdot \frac{\lambda^2}{v^2}\right)} \cdot$$

$$\cdot e^{-\lambda \cdot \frac{\zeta}{v}} \cdot \left\{ \operatorname{erf}\left[0.14 \cdot \left(v \cdot t - \zeta + 25.45 \cdot \frac{\lambda}{v}\right)\right] + \right. \qquad (23)$$

$$\left. -\operatorname{erf}\left[0.14 \cdot \left(v \cdot [t - t_r] - \zeta + 25.45 \cdot \frac{\lambda}{v}\right)\right]\right\} \cdot$$

It can be seen from this expression that, if the irradiation time t_r is very short compared to the time between the start of irradiation and the counting interval (pulsed operation), the difference between the two error functions is very small and unless S is very large the induced gamma-ray activity will be very low. On the other hand, if $t_r = t$ (continuous irradiation), ζ which is essentially a design parameter can be chosen so that the argument of the second error function is $\lesssim -2$ in which case the error function will be ~ -1. Furthermore, t can be chosen so that $v \cdot t$ is sufficiently large to make the argument the first error function $\gtrsim 2$ and the value of this function ~ 1. This case would require the minimum source strength and

$$\rho_\gamma(v,t) \sim 0.13 \cdot R \cdot \lambda \cdot \sigma_a \cdot N_{A_X} \cdot S \cdot \frac{1}{v} \cdot e^{-\left(0.02\, R_d^2 - 12.72 \cdot \frac{\lambda^2}{v^2}\right)} \cdot e^{-\lambda \cdot \frac{\zeta}{v}} \qquad (24)$$

The above arrangement, i.e., a single photon detector at a distance ζ downstream from the neutron source, can be used to determine the flow rate, v, if N_{A_X} and S are known at the site and time of the measurement. A slightly more complex arrangement involving two similar photon detectors at different distances ζ_1 and ζ_2 downstream from the neutron source can be used to make the system response independent of both N_{A_X} and S. Such an arrangement is shown in Figure 42. This method involves determination of the ratio of the response of the two detectors. This quantity is given by

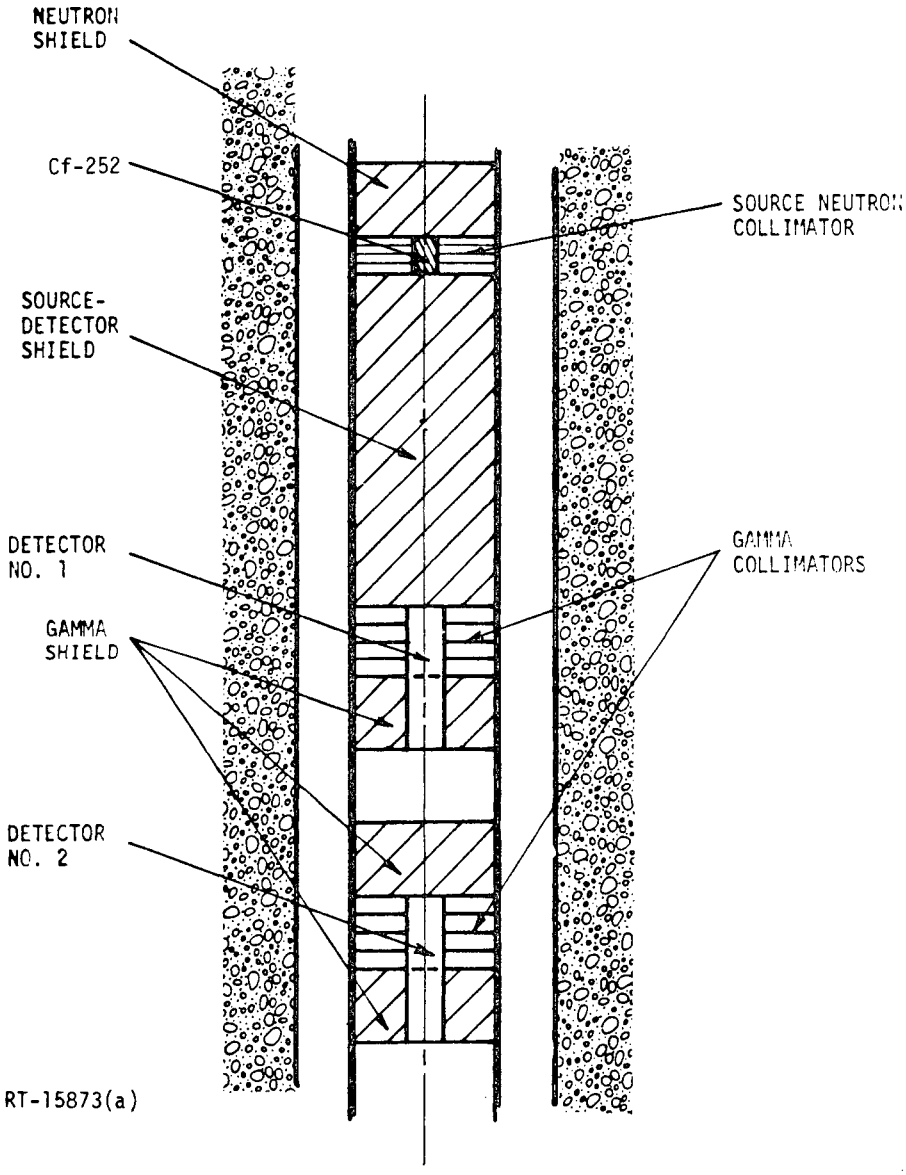

Figure 42. Schematic diagram of a two-detector neutron activation-based vertical flow rate gauge. The source-detector shield protects the detectors from direct exposure to source radiation. The neutron collimator defines the activation region in the borehole. The gamma shields and collimators define the brine volume sampled by the detectors at each instant.

$$\text{RATIO} = \frac{\rho_\gamma(v,t)_1}{\rho_\gamma(v,t)_2} = e^{-\frac{\lambda}{v} \cdot \left(\zeta_1 - \zeta_2\right)} = e^{-\frac{\lambda}{v} \cdot \Delta\zeta} \qquad (25)$$

This equation can be easily solved for v so that

$$v = \frac{\lambda \cdot \Delta\zeta}{\log\left[\rho_\gamma(v,t)_2\right] - \log\left[\rho_\gamma(v,t)_1\right]} \qquad (25a)$$

The sensitivity and accuracy of the two-detector method can also be calculated using Equation 24. The sensitivity defined here as the fractional change in the RATIO due to a unit change in the flow rate is given by

$$\text{SENSITIVITY} = \frac{d(\text{RATIO})}{\text{RATIO} \cdot dv} = \frac{\lambda \cdot (\zeta_1 - \zeta_2)}{v^2} \qquad (26)$$

The accuracy of the method is given by the estimated uncertainty in v, expressed as

$$\sigma_v \sim \frac{v^2}{\lambda \cdot \Delta\zeta} \cdot \left(\frac{1 + e^{\frac{\lambda}{v} \cdot \Delta\zeta}}{\rho_\gamma(v,t)_1}\right)^{1/2} \qquad (27)$$

The above expressions apply strictly to situations where there is no flow in or out of the borehole through the borehole wall, i.e., lateral or horizontal flow. The same expressions are approximately applicable when very slow lateral flow does occur. This is generally the case except in the vicinity of fractures where large quantities of brine may flow into or out of the borehole.

The feasibility of using in situ activation to determine lateral flow in the absence of vertical flow, i.e., along the borehole axis, is discussed in a later section. This method consists of irradiation (and activation) of a specific volume of the brine defined by appropriate collimation and monitoring of the induced photon activity. If the natural decay rate, λ, of the activated nuclide is small compared with the lateral flow rate, a decrease in the observed photon density with time will be the result of dilution of the activated nuclide by flow of nonactivated brine into and activated brine out of the sample volume.

3.1.2.1 Continuous Irradiation, Single-Detector Vertical Flow Rate Determination

The one-detector system described above was analyzed by estimating the expected photon counts for various flow rates along the borehole axis. The following assumptions were made:

1. Neutron source strength, $S \sim 8.2 \times 10^8$ n/sec, i.e., 350 μg Cf-252.
2. Three-inch sonde O.D. and eight-inch diameter well.
3. A three-inch diameter by three-inch long NaI(Tl) detector.
4. Cl-37 and O-16 activation by thermal and fast (14 MeV) neutrons, from the Cf-252 source, respectively. The concentrations of these isotopes were assumed to be N_{O-16} = 889,000 ppm and N_{Cl-37} = 250 ppm.

The assumed Cl-37 concentration is in the lower end of the concentration range observed in known geothermal fields, i.e., ~2 - 46,000 ppm (Ref 12,13). In the case of Cl-37 activation, the activated nuclide of interest is Cl-38m which decays via a 0.660 MeV photon emission with a half-life of 0.74 sec. In the case of O-16 the activated nuclide is N-16 which decays with $T_{1/2}$ = 7.2 sec. and produces a prominent peak at 6.143 MeV. Tables 3 and 4 give the estimated count rates at the corresponding nominal flow rates and the associated statistical uncertainties for Cl-37 activation. Tables 5 and 6 present similar information for O-16 activation.

Table 3. Determination of Vertical Flow Rates Using Cl-38m and a Single Detector at 60 cm from the Source. The counting Interval is One Hour

Nominal Flow Rate (cm/sec)	Total Counts (C/hr)	Uncertainty (cm/sec)
10	70	±0.22
20	937	±0.25
40	3437	±0.53
80	6581	±1.54
160	9106	±5.3
320	10711	±20.1

Table 4. Determination of Vertical Flow Rates Using Cl-38m and a Single Detector at 300 cm from the source. The Counting Interval is Four Hours

Nominal Flow Rate (cm/sec)	Total Counts (C/4 hrs)	Uncertainty (cm/sec)
40	76	±0.6
80	1959	±0.6
160	9937	±1.0
320	22378	±2.6

Table 5. Determination of Vertical Flow Rates Using N-16 and a Single Detector at 60 cm from the source. The Counting Interval is One Hour

Nominal Flow Rate (cm/sec)	Total Counts (C/hr)	Uncertainty (cm/sec)
2.5	562	±0.05
5	1742	±0.13
10	3067	±0.33
20	4072	±1.21
40	4687	±4.5
80	5033	±20.3

Table 6. Determination of Vertical Flow Rates Using N-16 and a Single Detector at 300 cm from the source. The Counting Interval is Four Hours

Nominal Flow Rate (cm/sec)	Total Counts (C/4 hrs)	Uncertainty (cm/sec)
5	75	±0.1
10	1276	±0.1
20	5250	±0.2
40	10649	±0.6
80	15166	±1.9
160	18099	±7.0

Tables 3 through 6 clearly show that activation of Cl-37 and O-16 can be used to determine the vertical flow rate thus indicating the feasibility of the one-detector method. It is also obvious that one or the other of the two nuclides can be used to cover the entire range of interest, i.e., $2.5 \leqslant v \leqslant 450$ cm/sec. The disadvantage of this method is that it requires accurate knowledge of the activatable isotope concentrations.

3.1.2.2 Continuous Irradiation, Two-Detector Vertical Flow Rate Determination

As noted above, the advantage of a two-detector system (see Figure 42) is that it does not require knowledge of the activatable isotope concentration in the brine, Equation 25. Equation 25a is plotted in Figures 43 and 44. Figure 43 presents the calculated two detector system response, i.e., the photon count ratio, as a function of vertical flow rate of the brine for various distances between the near and far detectors (relative to the source). The activity monitored is the 0.66 MeV photons emitted in the de-excitation of Cl-38m. Figure 44 presents similar information for the case where the activity monitored is that resulting from the decay of N-16 (6.143 MeV photons). These plots indicate that the method is feasible using either Cl-37 or O-16 activation. As for the one-detector system, Cl-37 activation may be preferable. This becomes more transparent if one examines the sensitivity of the method, Equation 26. Figures 45 and 46 are plots of the technique sensitivity as a function of flow rate for various near to far detector separations. Figure 45 shows the results for Cl-37 activation while Figure 46 gives the coresponding information for O-16 activation.

Use of a 350 μg Cf-252 source results in statistical uncertainties in the flow rate determination of 1 to 2 percent for counting periods $\lesssim$ four hours. Equation 27 has been used to estimate the accuracy of a two-detector flow rate gauge under the following assumptions.

1. 350 μg Cf-252 neutron source.
2. Two identical three-inch diameter by three-inch long NaI(Tl) detectors; the detector nearer the source is 50 cm away from it.
3. Cl-37 and O-16 activation by thermal and 14 MeV neutrons from the Cf-252 source, respectively; the concentrations of these isotopes assumed to be 250 ppm and 889,000 ppm, respectively.

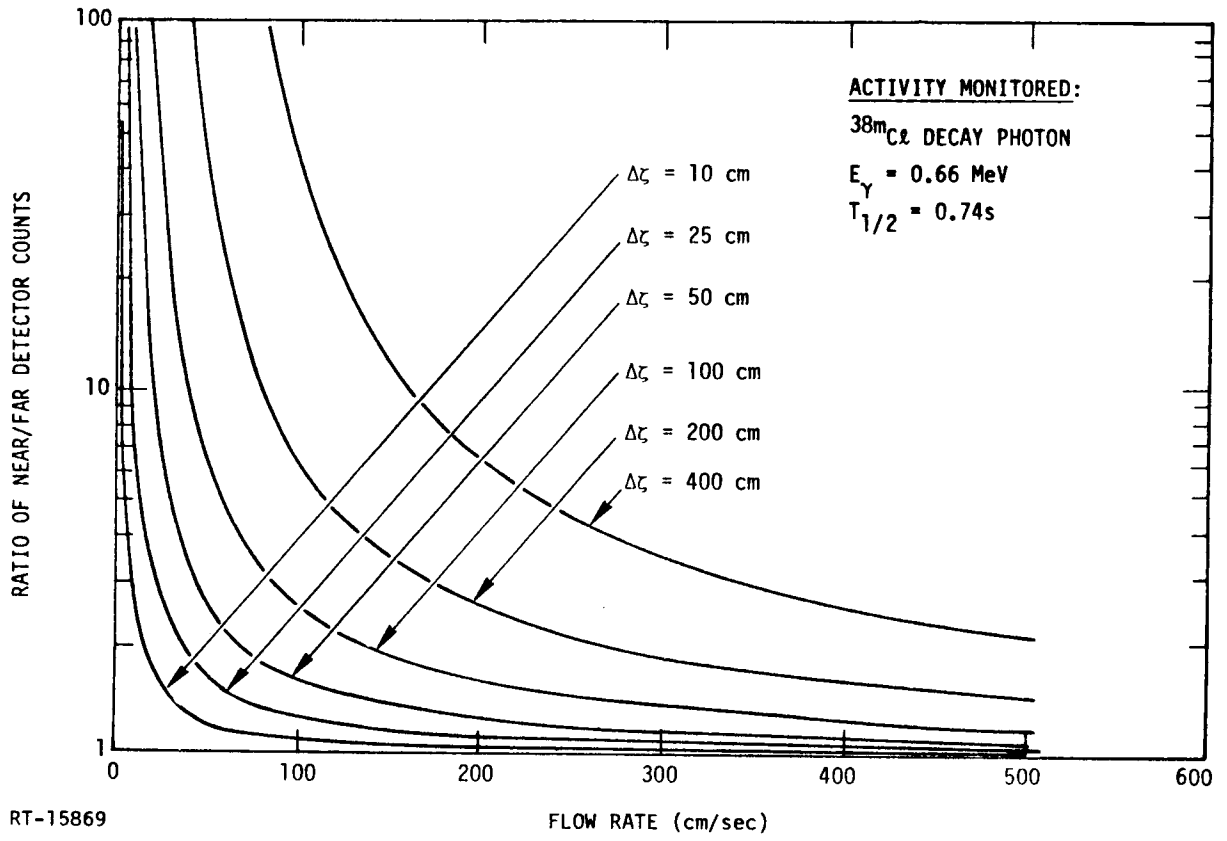

Figure 43. Calculated near- to far-detector photon count ratio as a function of the vertical flow rate for various distances ($\Delta\zeta$) between the two detectors. The near detector is 50 cm from the neutron source. The activated nuclide is ^{38m}Cl.

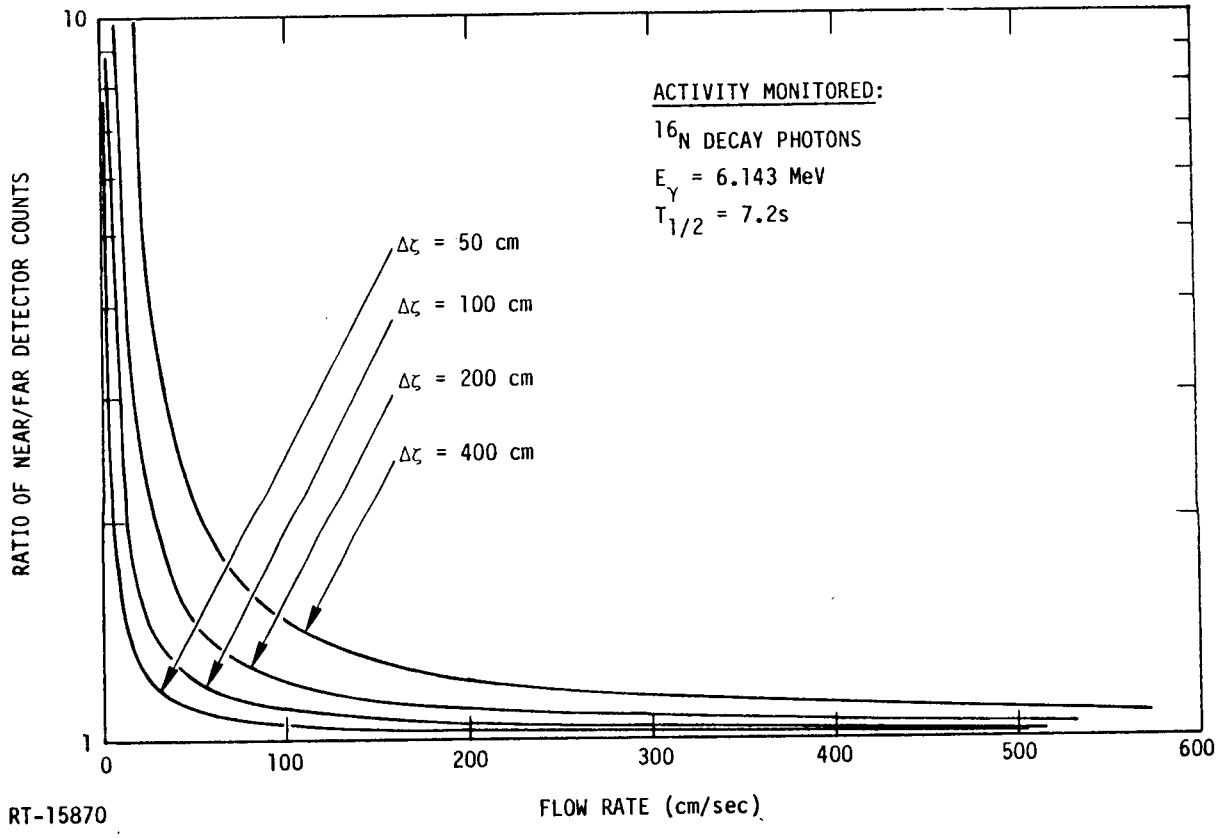

Figure 44. Calculated near- to far-detector photon count ratio as a function of the vertical flow rate for various distances ($\Delta\zeta$) between the two detectors. The near detector is 50 cm from the neutron source. The activated nuclide is ^{16}N.

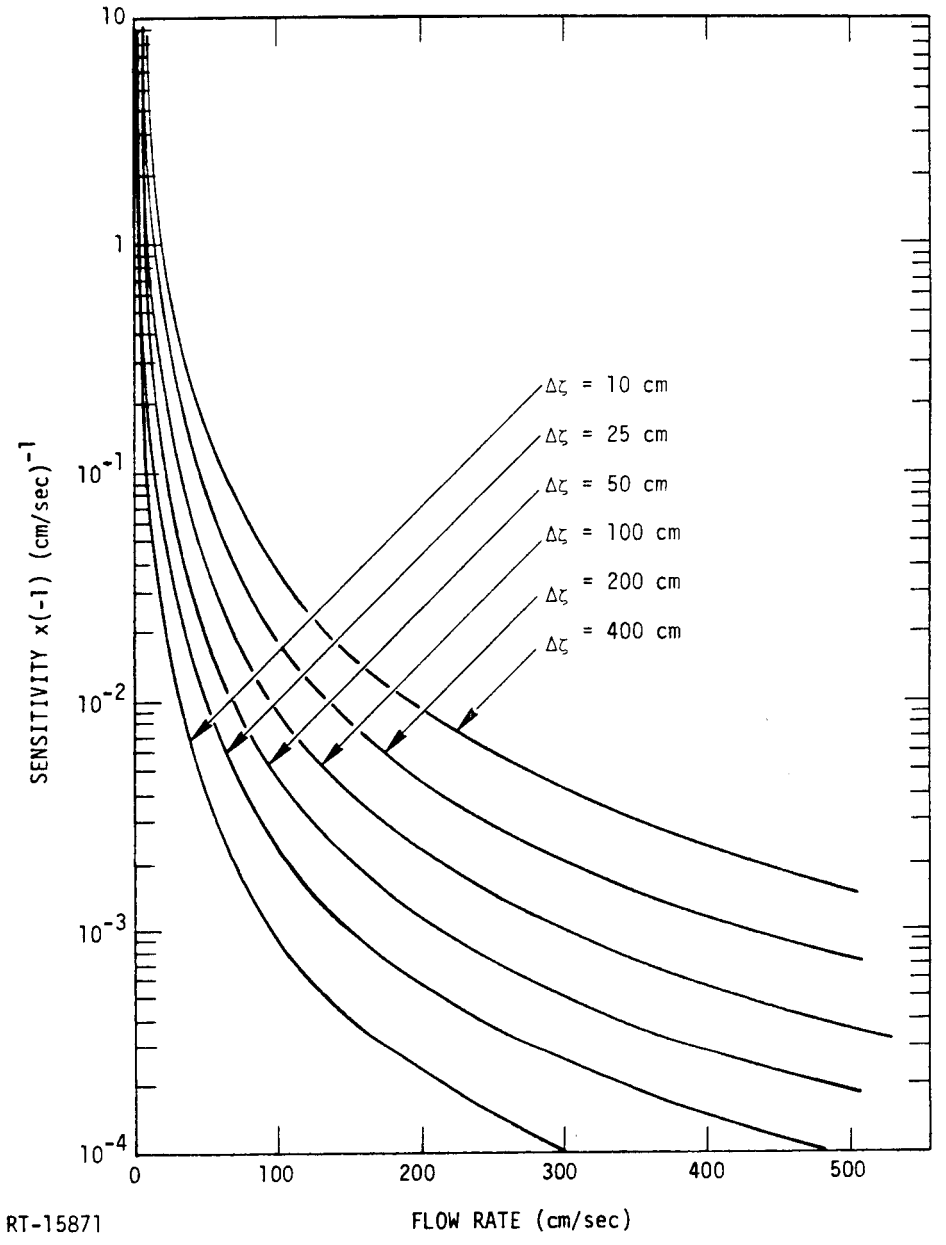

Figure 45. Relative change in the count ratio of near-to far-detector per unit change (one cm/sec) in the flow rate. The near detector is located 50 cm from the neutron source. The activated nuclide is $^{38m}C\ell$.

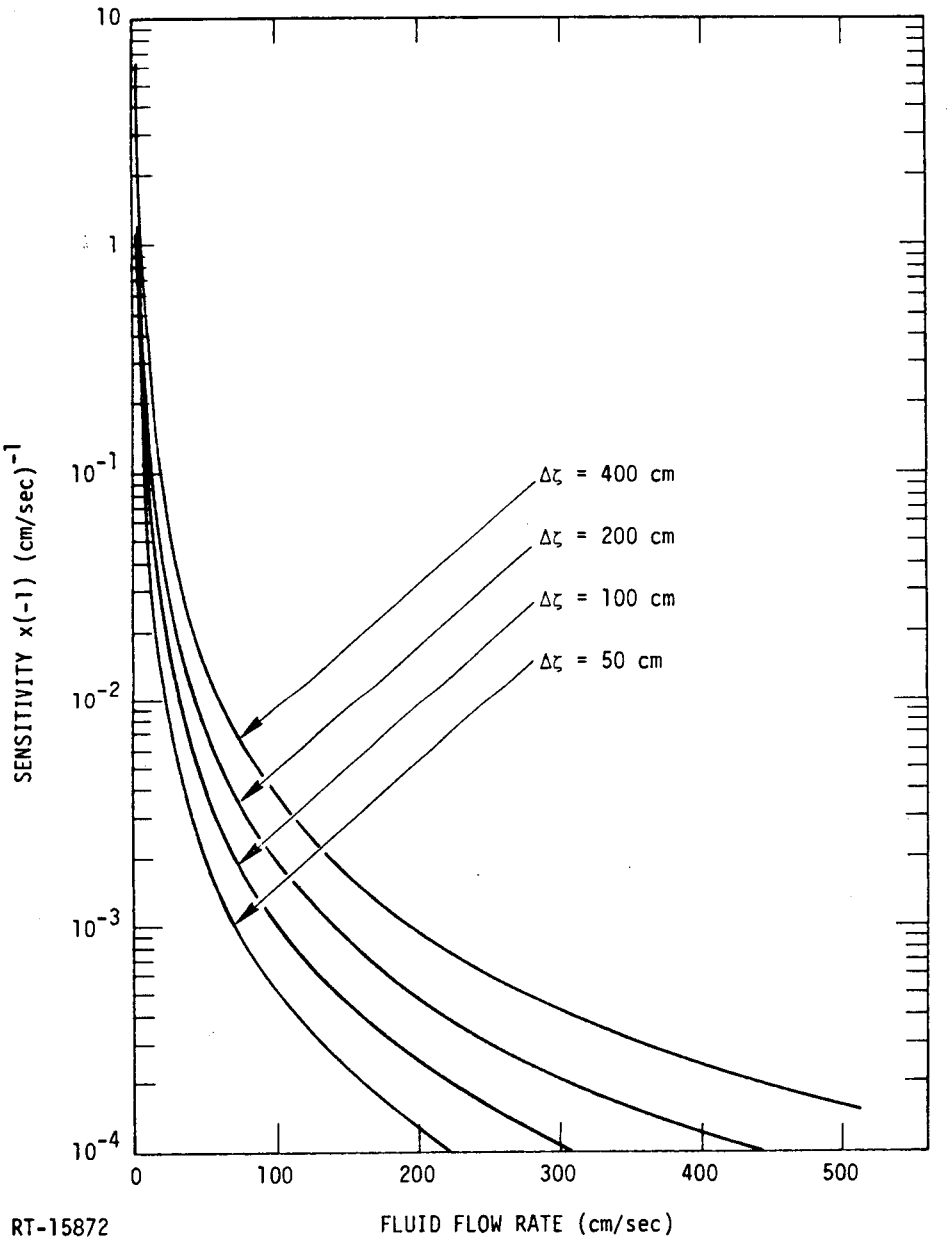

Figure 46. Relative change in the count ratio of near-to far-detector per unit change (one cm/sec) in the flow rate. The near detector is located 50 cm from the neutron source. The activated nuclide is ^{16}N.

The estimated uncertainties are plotted in Figures 47 through 50. Figure 47 shows the calculated uncertainty as a percentage of the flow rate for flow rates in the range of interest and for various detector separations, $\Delta\zeta$. The activity monitored is that resulting from activation of Cl-37. These uncertainties correspond to one hour counting periods. When the counting interval is increased to three hours the corresponding uncertainties decrease as shown in Figure 48. It is seen from this figure that uncertainties $\lesssim 2$ percent are predicted for a two detector system with $\Delta\zeta = 200$ cm for flow rates from 40 to 450 cm/sec.

Similar information is presented in Figures 49 and 50 for the case where the monitored activity is that of N-16 resulting from fast neutron activation of O-16. In this case it is seen that a two detector system with $\Delta\zeta = 300$ cm would yield ~ 2 percent uncertainties in the measured flow rates in the range from ~ 7 to ~ 50 cm/sec when the counting period is four hours (Figure 50). Therefore, using either chlorine or oxygen activation, the method can be used to determine linear brine flow rates in the range of interest with uncertainties $\lesssim 2$ percent.

It should be noted that the above estimates represent an ideal case of zero background radiation. Although it is not anticipated that background radiation will be a limiting factor, its effect must be examined.

3.1.3 In Situ Activation Method: Lateral Flow

The in situ activation technique for the determination of lateral flow in the absence of vertical flow consists of neutron activation of an isotope present in the brine which produces a nuclide with relatively long half-life, $T_{1/2}$. The sampled volume is defined as shown in Figure 51 by a conical collimator focussed on the photon detector so that only the photon activity induced in the immediate vicinity of the source is detected, and any photons produced by activation of the surrounding formation are largely excluded. Irradiation (activation) occurs during a finite period of time at the end of which the neutron source is moved to a shielded position so that no further activation occurs within the acceptance angle of the collimator. The irradiation period must be long enough to produce sufficient activity. As noted previously, the photon activity within the irradiated volume, i.e., the counts recorded by the photon detector, is a function of the time after the end of irradiation. If the activated nuclide half-life is long compared to the lateral mass flow, the observed photon count rate will decrease with time at a rate determined by the mass or volume flow rate. This is obviously due

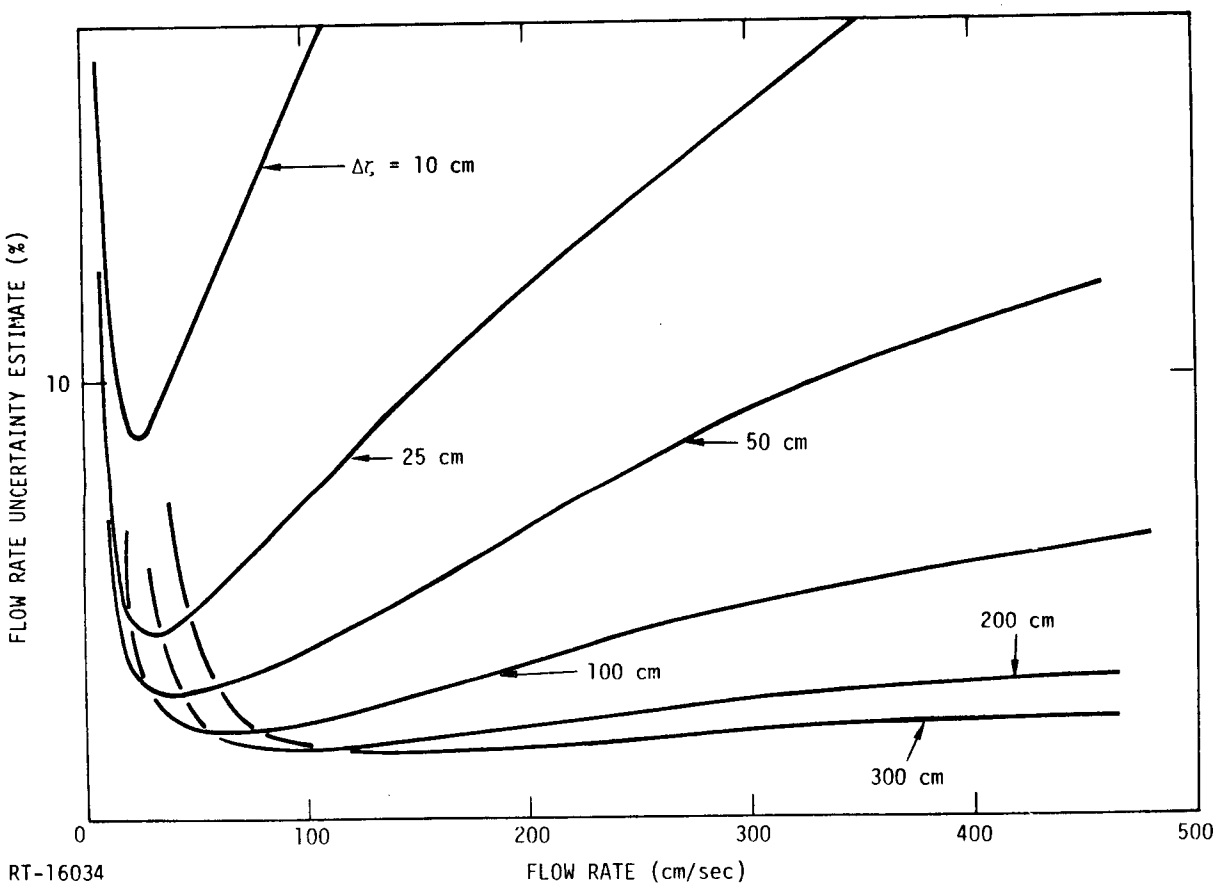

Figure 47. Estimated accuracy of a two-detector flow rate gauge. The source strength is 350 μg of ^{252}Cf, the near-detector distance from the source is 50 cm, the active element is ^{38m}Cl, and the counting period is one hour.

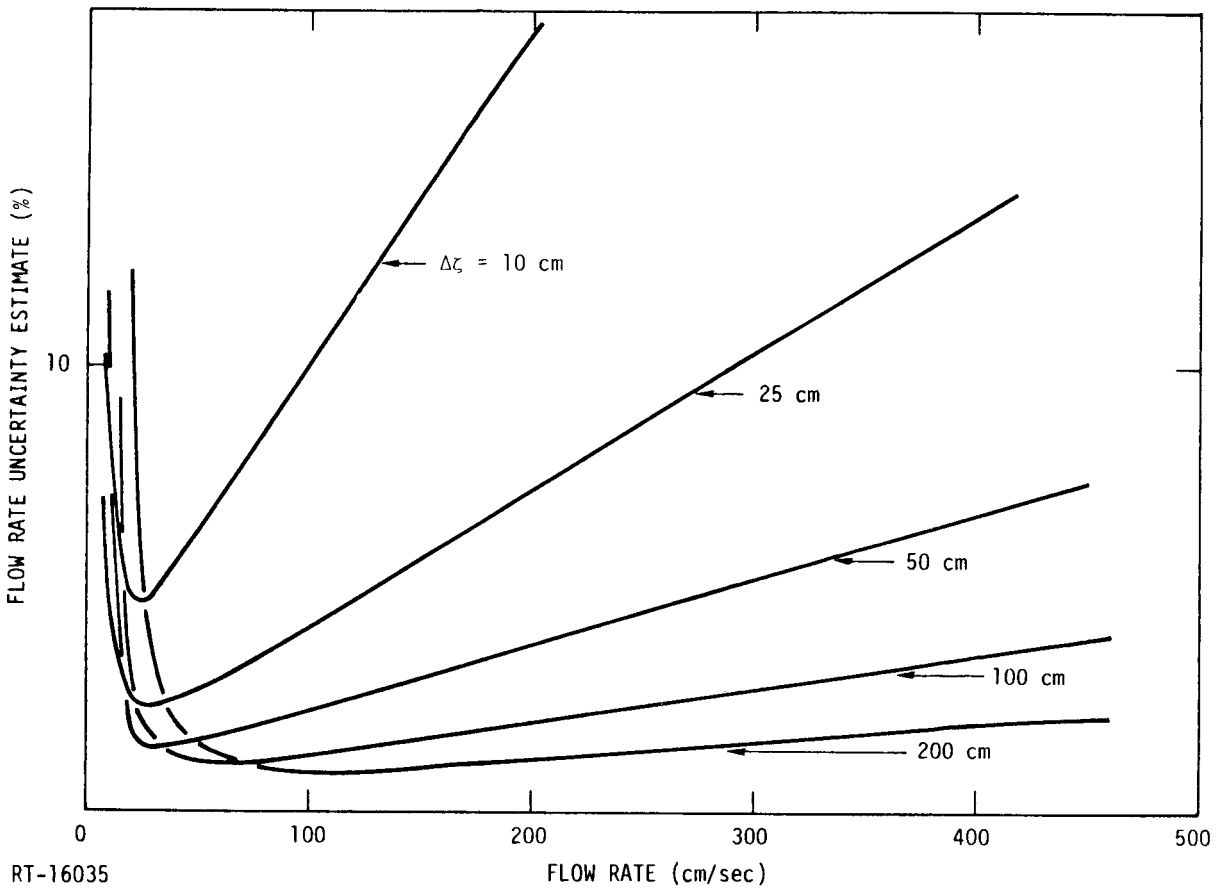

Figure 48. Estimated accuracy of a two-detector flow rate gauge. The source strength is 350 μg ^{252}Cf, the near-detector distance from the source is 50 cm, the active elements is ^{38m}Cℓ, and the counting period is three hours.

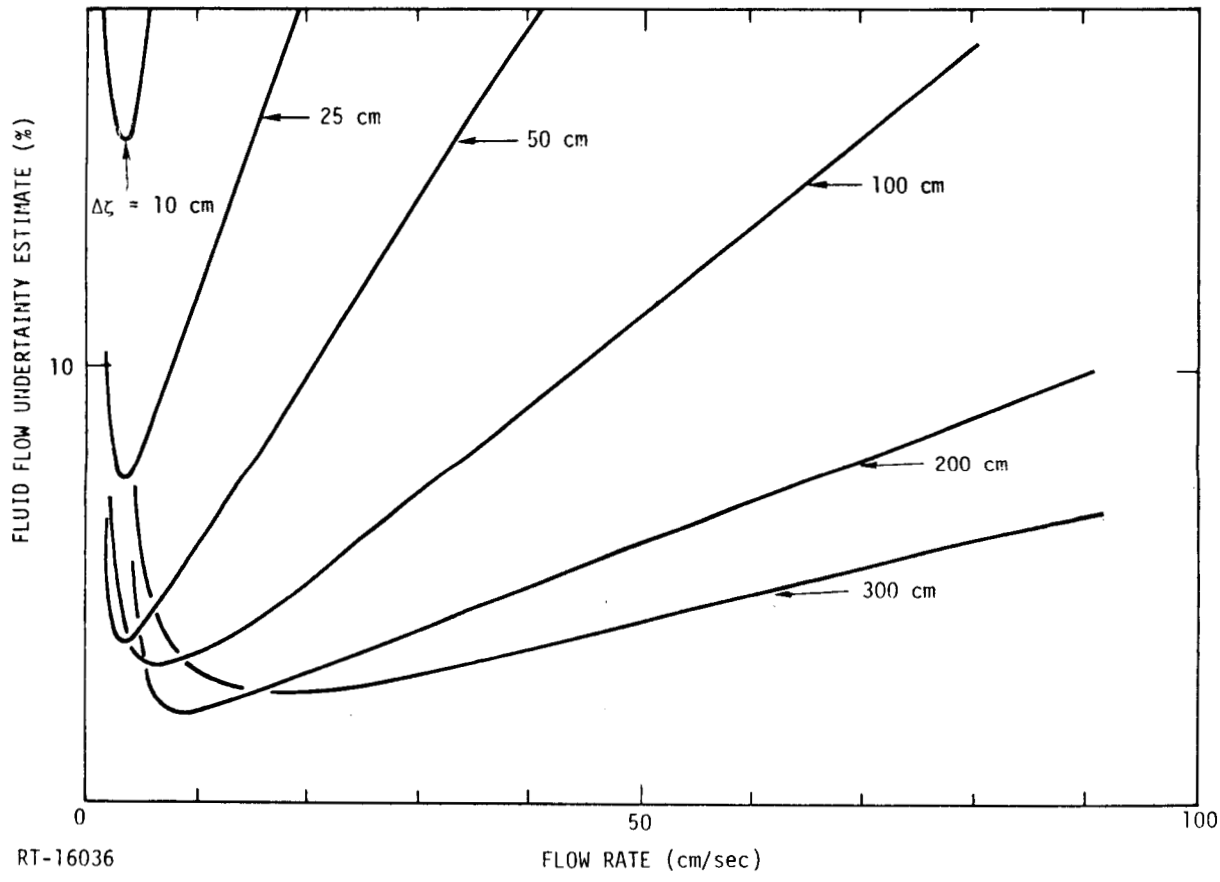

Figure 49. Estimated accuracy of a two-detector flow rate gauge. The source strength is 350 μg ^{252}Cf, the near-detector distance from the source is 50 cm, the active element is ^{16}N, and the counting period is one hour.

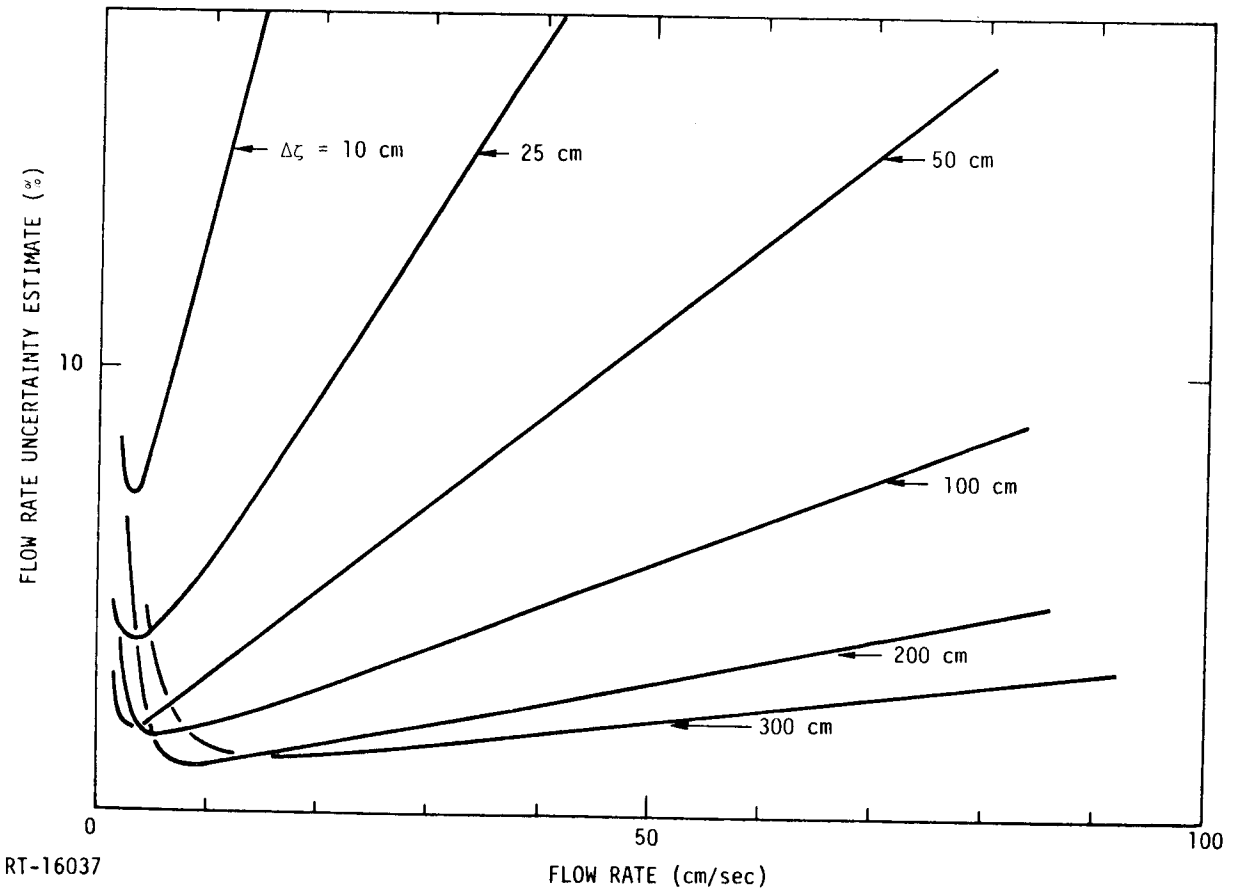

Figure 50. Estimated accuracy of a two-detector flow rate gauge. The source strength is 350 μg ^{252}Cf, the near-detector distance from the source is 50 cm, the active element is ^{16}N, and the counting period is four hours.

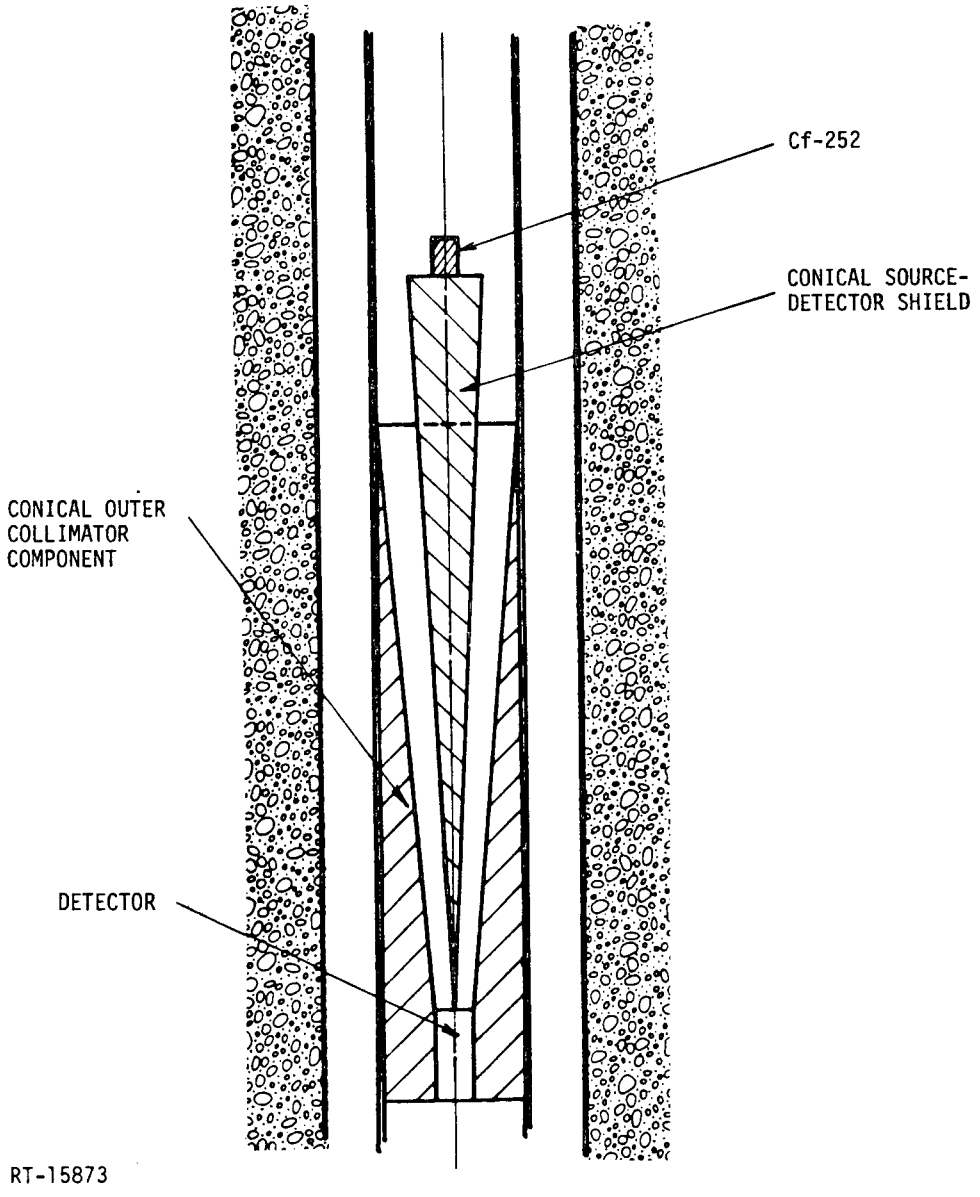

Figure 51. Schematic diagram of the source, detector and collimator arrangement for the determination of lateral flow in the absence of vertical flow.

to the dilution of the activated nuclide as nonactivated fluid flows into the sampled volume and activated fluid flows out.

An appropriate activatable isotope is Mn-55 which upon absorption of a thermal neutron produces Mn-56 whose half-life is 2.58 hours. The prominent photon energy is 0.847 MeV. The range of concentrations of Mn in geothermal fields is 0.01 - 1370 ppm (Ref 13). A concentration of 100 ppm will result in $\sim$6600 photons/hour recorded by the detector at the end of a one hour irradiation period. This estimate is based on the same source strength and photon detector assumed in our previous estimates. The source/detector distance (or collimator length) has been assumed to be 50 cm. Based on these estimates, the technique described here appears to be feasible for the determination of mass flow rates $\gtrsim 10^{-4}$ g/cm^2/sec.

3.2 TECHNIQUE APPLICABILITY

The above calculations were performed assuming that the borehole is filled with water containing certain amounts of the activatable element, i.e., Cl or Mn. This was because an expression for the thermal neutron flux had already been derived for the specific case of a point source in water. The assumption of a more realistic "brine" consisting perhaps of a water-steam mixture containing rock chips, various dissolved minerals and gases would require a much more involved neutron flux derivation, but would not yield significant additional information. The neutron flux will be different in various brines. This would effect the distribution of de-excitation photons, Equation 24, and, thus, the absolute response of the photon detectors. Consequently, the response of the single-detector, continuous irradiation system would likely require separate calibration for applications in various brines. The response of the two-detector system is independent of variations in the activating neutron flux, Equation 25, and, hence, the average composition of the brines.

In the above calculations it was also assumed that the "brine" flows past the source and detector at a uniform rate, i.e., an average flow rate. In reality, various volume elements of the brine will flow at different rates depending on the radial position in the annular region between the sonde case and the borehole wall. The flow profile will be further complicated by turbulent flow. The continuous irradiation techniques may be insensitive to irregularities in the flow pattern. An understanding of the flow mechanism(s) operable in the borehole is important not only for the selection of the most suitable NAA measurement technique, but, equally, for the development of the appropriate calibration procedure.

The occurrence of two phase flow (steam and water) in geothermal wells render conventional flow measuring devices, e.g., impeller type flow meters, inapplicable. NAA techniques described above can still be applied.

Since oxygen is present in both phases, O-16 activation with fast neutrons from either a Cf-252 source or a neutron generator can be used to determine the average flow rate of the two-phase flow. An instrument with this capability combined with capabilities to determine the average mass density of the fluid using, for example, a gamma-gamma method, and the borehole diameter using a caliper can provide the information necessary to determine the total mass flow rate of the two-phase fluid.

As indicated by the above calculations of the technique accuracy and sensitivity, O-16 activation is practical for flow rates $\lesssim$100 cm/sec ($\lesssim$500 gal/min in an eight-inch diameter borehole). Flow rates encountered during exploration or in the preproduction development of wells are generally within this range. For example, the ability to measure very low flow rate (a few cm/sec) is very important in understanding the interaction between adjacent fracture zones penetrated by the same borehole. Under the right temperature and pressure conditions, flow in the region between adjacent fractures is often extremely slow, but it may be relatively high above the upper fracture zone and below the lower one. This situation may arise when the lower fracture zone acts as a sink for high temperature fluid from a deeper producing zone while the upper zone acts as a source of lower temperature fluid. Under these circumstances, it is the lower temperature fluid which will be extracted. Temperature (fluid), pressure and flow data are essential to the understanding of this particular region of the reservoir. On the basis of this information, a decision might be made to seal the lower fracture zone in order to allow extraction of the hotter fluid.

For flow rates above the range accessible with oxygen activation, the NAA methods can be used to determine the average flow rate of the liquid phase of the brine. This is accomplished by activation of the chlorine generally present in sufficient concentrations in liquid dominated hydrothermal systems. It may even be possible to correct the data obtained using Cl-37 activation to derive the average flow rate of the two-phase fluid. Empirical corrections may be derived using data obtained by both O-16 and Cl-37 in the overlap region of the flow rate ranges accessible by the two methods. Corrections for higher flow rates can then be estimated by extrapolation.

4. CONCLUSIONS AND RECOMMENDATIONS

Techniques for the determination of formation temperature and brine flow rates have been described in the preceding sections. The computation (simplified model) analysis discussed in subsection 2.3, the results and analysis of the preliminary measuremetns described in subsection 2.4.1, as well as the more exact theoretical work of G. C. Summerfield (Appendix) demonstrate the scientific feasibility of the formation temperature gauging technique. Measurements performed to date in the well geometry (subsection 2.4.1) have produced results in agreement with those of the preliminary measurements, and they indicate that with the present sensor design conditions in the borehole, i.e., fluid temperature, salinity, density, do not affect the determination of the formation temperature. These results demonstrate the engineering feasibility of the method for the test formations examined. In order to complete the demonstration of the engineering feasibility, it is necessary to perform measurements in the well geometry using test formations with different neutron moderating properties ($\xi\Sigma_s$). These will serve to complete the analogy between the well geometry and preliminary measurement results, thus establishing the general validity of the data analysis method described in subsection 2.4.1. The results of the computational analysis of the brine flow gauging technique discussed in subsection 2 warrant further, experimental verification.

Although much has been achieved by the work described in this report, work still remains to be done before either a formation temperature sonde or a brine flow instrument can be designed. In view of the importance of these parameters in reservoir potential assessment and efficient resource exploitation, and the encouraging results of the present study, continued development of the above tools is warranted. Further work in the development of the formation temperature sensor should include measurements performed with progressively more realistic test formations to demonstrate the result of the present preliminary measurements (subsection 2.4.1). Experiments must be performed to assess the effects of borehole wall rugosity, mudcake, and radial temperature gradients, and to determine the depth of penetration (range of investigation). Based on

the results of the present study and those to be obtained from the above measurements, and with input from the goethermal community, the design specifications of a formation tempeature sonde should be delineated. A sonde could then be designed and fabricated.

It is generally agreed that a formation temperature gauge is essential for the assessment of reservoir potential and well productivity. It is also generally agreed that current methods are inadequate, because their results are ambiguous. Furthermore, current methods are extremely time consuming and, therefore, are not conducive to timely development of geothermal resources. A formation temperature sonde utilizing the technique described in this report would provide a reliable determination of the true formation temperature on a time scale which would expedite the decision making process regarding development or continued exploitation of a particular field or further drilling of specific wells. This would reduce investment risks, permit efficient utilization of equipment and resources, and expedite geothermal development (Ref 14). An additional, important use of this instrument at this point of geothermal development would be to provide data which could be used to test theoretical models of goethermal fields. This capability is essential in enhancing our understanding of such very complex systems which would expedite future geothermal development.

An important parameter in applying the present method for geothermal well logging is the useful depth of penetration inside the formation, or the technique range of investigation. It is not generally agreed what this range should be. Our estimate with regard to the present method based on the range of investigation of other "neutron-neutron" gauging techniques (subsection 2.5.1) is several inches. It is essential that this be verified experimentally. It is clear, however, that a depth of investigation several inches into the formation is sufficient when the measurement is performed soon after drilling or during brief interruptions between drill bit changes (wireline use) when the formation is least disturbed and the radial temperature profile is flat to within a very short distance from the borehole wall (Ref 14,15). An instrument based on the present technique could be used in this mode. If for any reason such operation were not convenient or practical in specific instances, the present method would provide additional formation temperature information not obtainable by current methods to permit more reliable extrapolation to the undistrubed formation temperature. This additional information would consist of at least one more temperature value several inches away from the borehole wall to supplement the value at the wall determined by current methods.

REFERENCES

1. Meghreblian, R. V. and D. K. Holmes, "Reactor Analysis," McGraw-Hill Book Company, Inc., Chapter 4, p. 69 (1960).

2. Coveyou, R. R., R. R. Bates, and R. K. Osborn, J. Nucl. Energy 2, 153 (1956).

3. Steinman, D. K., D. G. Costello, C. S. Pepper, W. E. Gober, D. B. Breuner, J. S. M. Wilson, J. C. Young, and J. John, ERDA Status Report INTEL-RT 7019-004 (February 1977).

4. Sherman, H., and S. Locke, Society of Petroleum Engineers of AIME, Paper No. SPE 5510 (1975).

5. Weber, H. J., C. A. Preskitt, and C. E. Rinehart, "A Cf-252 Thermal Neutron Cross Section Gauge for Interpretation of Neutron Logs for Oil Applications," presented at the Symp. International Sur L'Utilization Du Californium-252, Paris, France, April 1976.

6. Stoddard, D. H., and H. E. Hootman, "Cf-252 Shielding Guide," Savannah River Laboratory, AEC Research and Development Report DP-1246 (March 1971).

7. Reuter-Stokes Catalogue 12, "Neutron Proportional Counters for Neutron Physics Experiments, Neutron Monitoring, Industrial Gauging."

8. Mathews, D. R., P. K. Koch, J. Adir, and P. Watti, "GGC-5, A Computer Program for Calculating Neutron Spectra and Group Constants," Gulf General Atomic Company, Report GA-8871 (September 27, 1971).

9. Czubek, J. A., in Proceedings of the Symp. on the Use of Nuclear Tech. in the Prospecting and Development of Natural Resources, IAEA, Buenos Aires, Nov. 5-9, p. 3 (1969).

10. Beckurts, K. H., and K. Wirtz, "Neutron Physics," Springer-Verlag, Section 15.3, p. 333 (1964).

11. Kunz, J. F. and J. F. Whitbeck, Idaho National Engineering Laboratory, Aerojet Nuclear Company, Report ANCR-1318 (May 1976).

12. Ellis, A. J. Am. Scientist 63, No. 5, 510 (1975).

13. Miller, R. L., Idaho National Engineering Laboratory, Aerojet Nuclear Company Report ANCR-1342 (August 1976).

14. Rowley, J. C. Los Alamos Scientific Laboratory, Private Communication (sc: C. Carwile and T. Veneruso) July 27, 1977.

15. Crosby, G., Exploration Director, Geothermal Operations Phillips Petroleum, Private Communication, January 27, 1978.

APPENDIX

NEUTRON TRANSPORT CALCULATIONS IN INFINITE MODERATING MEDIA

NEUTRON TRANSPORT CALCULATIONS IN INFINITE MODERATING MEDIA

G. C. Summerfield

A number of detailed computations of neutron spectra in infinite media have indicated that for small absorption one can measure the moderator temperature by a fairly simple measurement of the neutron spectrum. However, even in an infinite medium any significant absorption can confuse the results.

The parameter which measures the size of the absorption appears to be

$$\Delta = \frac{2A\ \Sigma_a(T)}{\Sigma_s} \tag{A1}$$

where A is the moderator mass number, $\Sigma_a(T)$ is the thermal absorption cross section and Σ_s is the thermal scattering cross section.

The relevant papers here are:

H. Hurwitz, Jr., et al., Nucl. Sci. and Eng. 1, 280 (1956).

E. R. Cohen, Geneva Conf. Paper No. 611 (1955).

R. R. Coveyou, et al., J. Nucl. Energy 2, 153 (1956).

If Δ is small one can represent the neutron spectrum in the thermal group by

$$\phi(E) = \alpha E\ e^{-E/T_n} \tag{A2}$$

where

$$T_n = (1 + 0.46\Delta)T \tag{A3}$$

We can get an idea how this comes about as follows:

The infinite medium transport equation is

$$\Sigma_a(E)\ \phi(E) = \int_o^\infty dE\left\{\phi(E')\ \Sigma_s(E'\to E) - \phi(E)\ \Sigma_s\ (E\to E')\right\} + S(E) \qquad (A4)$$

Integrating gives the normalization of ϕ

$$\int_o^\infty dE\ \phi(E)\Sigma_a = S_o \qquad (A5)$$

where

$$S_o = \int_o^\infty dE\ S(E) \qquad (A6)$$

If we multiply by E^ν and integrate, we get

$$\int dE\ E^\nu\ \Sigma_a\phi = \int dE \int dE'\ E^\nu \left\{\phi(E')\ \Sigma_s\ (E'\to E) - \phi(E)\ \Sigma_s\ (E\to E')\right\} \qquad (A7)$$

We have ignored

$$E^\nu\ S(E)\ dE\ .$$

This should be alright if $\nu < 0$, since the source is at high energy.

Now we make our assumption

$$\phi(E) = \alpha E\, e^{-E/T'} \tag{A8}$$

with

$$T' = T + \Delta T \tag{A9}$$

Then to first order in ΔT

$$\int dE\, E\, \frac{\alpha B}{\sqrt{E}}\, E\, e^{-E/T} = \Delta T \int dE \int dE'\, E^{\nu}\, \alpha \left(\frac{E'^2}{T^2}\, e^{-E'/T}\, \Sigma_s\,(E' \to E) - \frac{E^2}{T^2}\, e^{-E/T}\, \Sigma_s\,(E \to E') \right) \tag{A10}$$

Then using the heavy gas cross section

$$\Sigma_s(E\ E') = \Sigma_s \sqrt{E'/E} \left\{ \delta(E'-E) + \frac{1}{A}\,(E'+E) \left\{ \delta'(E'-E) + \delta''(E'-E) \right\} \right\} \tag{A11}$$

This gives

$$\frac{\Delta T}{T} = \frac{A\, \Sigma_a(T)}{4\Sigma_s[\Gamma(\nu+2) - \tfrac{1}{2}\Gamma(\nu+3)]} \tag{A12}$$

An appropriate value for ν would seem to be $\nu = -2$, for which

$$\frac{\Delta T}{T} = \frac{A\, \Sigma_a}{2\, \Sigma_s}$$

The crude arguments here should be used only to justify the factor .

What is known is that for $\Delta > 1$ the neutron distribution is seriously distorted and does not give a good temperature measurement.

However, we must find a reliable relationship between T_n and T for small Δ. Coveyou et al. claim that

$$\Delta T = 0.46\,\Delta \tag{A13}$$

gives the neutron distribution to within 5 percent for ideal gases A going from 1 to 25.

It would seem from these results that this technique should work like a charm. However, the problem is space dependent. We can consider a fast point source in an infinite medium. The slowing down density for a point source at $\underset{\sim}{r} = 0$ is

$$q = \frac{e^{-r^2/4\tau}}{(4\pi\tau)^{3/2}}\; p \tag{A14}$$

where τ is the fermi age and p is the resonance absorption. The age equation for the thermal group is

$$-D\nabla^2 \phi_{th} + \Sigma_a \phi_{th} = q \tag{A15}$$

where

$$\phi_{th} = \int_0^{E_{th}} dE\; \phi(E) \tag{A16a}$$

and

$$D = \frac{\int_0^{E_{th}} dE\; D(E)\; \phi(E)}{\phi_{th}} \tag{A16b}$$

$$\Sigma_a = \frac{\int_0^{E_{th}} dE\ \Sigma_a(E)\ \phi(E)}{\phi_{th}} \qquad \text{(A16c)}$$

The Green function for the diffusion equation is $[e^{-r/L}]/4\pi r$

$$L^2 = \frac{D}{\Sigma_a} \qquad \text{(A17)}$$

Thus the solution of (15) is

$$\phi_{th} = \frac{p}{4\pi D(4\pi\tau)^{3/2}} \int d^3r' \ \frac{e^{-|\underline{r}-\underline{r}'|/L}}{|\underline{r}-\underline{r}'|}\ e^{-r'^2/4\tau} \qquad \text{(A18)}$$

For large r this becomes

$$\phi_{th} = \frac{e^{-r/L}}{r}\ \frac{p}{4\pi D} \qquad \text{(A19)}$$

We can note that

$$\nabla^2\ \frac{e^{-r/L}}{r} = L^{-2}\ \frac{e^{-r/L}}{r} \qquad \text{(A20)}$$

$$\nabla^2 \phi_{th} = \frac{1}{L^2}\ \phi_{th}$$

For small r we must change variables

$$\underline{R} = (\underline{r}-\underline{r}')/L$$

$$\phi_{th} = e^{-r^2/4\tau} \frac{L^2 p}{4\pi D(4\pi\tau)^{3/2}} \int d^3R \frac{e^{-R}}{R} e^{-\frac{L^2R^2}{4\tau}} e^{L\underline{r}\cdot\underline{R}/2\tau} \quad (A21)$$

if $rL \ll \tau$, the r dependence of the integrand can be ignored and

$$\nabla^2 \phi_{th} \cong -\frac{3}{2\tau} \phi_{th} \quad (A22)$$

This suggests that the normalization condition on ϕ_{th} be written

$$\left\{A_{eff} + \Sigma_a\right\} \phi_{th} = q \quad (A23)$$

where A_{eff} is $3D/2\tau$ for small r and D/L^2_{eff} for large r. Assume for the moment that A_{eff} is constant in energy. The normalization condition should be

$$A_{eff} \int dE\ \phi(E) + \int dE\ \Sigma_a\ \phi(E) = q \quad (A24)$$

Then taking

$$\phi(E) = \alpha E e^{-E/T} \quad (A25)$$

and $\Sigma_a = B/\sqrt{E}$ we find

$$\alpha = \frac{q}{BT^{3/2}\Gamma(3/2) + A_{eff}T^2\Gamma(2)} \quad (A26)$$

and

$$\int dE\ \phi(E) = \frac{q}{\Sigma_a(T)\Gamma(3/2) + A_{eff}} \tag{A27}$$

and

$$\int dE\ \Sigma_a(E)\phi(E) = \frac{q\ \Sigma_a(T)\Gamma(3/2)}{\Sigma_a(T)\Gamma(3/2) + A_{eff}} \tag{A28}$$

For the case of an infinite medium A_{eff} is zero and (A27) increases like $T^{1/2}$ and (A28) is constant.

If we are going to discuss the filtered count rate we need to break the thermal flux into two energy groups.

$$\phi_1 = \int_o^{E_1} dE\ \phi(E) \tag{A29a}$$

$$\phi_2 = \int_{E_1}^{E_{th}} dE\ \phi(E)$$

Then

$$-D_1\nabla^2\phi_1 + \left(\Sigma_{T_1}\ \Sigma_1 - \Sigma_{S_1}\right)\phi_1 = \Sigma_{S_{2\to1}}\phi_2 \tag{A30a}$$

$$-D_2\nabla^2\phi_2 + \left(\Sigma_{T_2} - \Sigma_{S_2}\right)\phi_2 = \Sigma_{S_{1\to2}}\phi_1 + q \tag{A30b}$$

We can get an idea of the relative effects of geometry and such by taking

$$-D_1\nabla^2\phi_1 = A_{eff_1}\,\phi_1 \tag{A31a}$$

$$-D_2\nabla^2\phi_2 = A_{eff_2}\,\phi_2 \tag{A31b}$$

Then we get

$$\left\{A_{eff_1} + \left(\Sigma_{T_1} - \Sigma_{S_{1-1}}\right)\right\}\phi_1 = \Sigma_{S_{2\to1}}\,\phi_2 \tag{A32a}$$

$$\left\{A_{eff_2} + \left(\Sigma_{T_2} - \Sigma_{S_{2-2}}\right)\right\}\phi_2 = \Sigma_{S_{1\to2}}\,\phi_1 + q \tag{A32b}$$

Define,

$$\Sigma'_{R_1} = A_{eff_1} + \Sigma_{T_1} - \Sigma_{S_{1-1}} \tag{A33a}$$

$$\Sigma'_{R_2} = A_{eff_2} + \Sigma_{T_2} - \Sigma_{S_{2-2}} \tag{A33b}$$

This gives

$$\phi_1 = \frac{\Sigma'_{R_1}\,q}{\Sigma'_{R_1}\Sigma'_{R_2} - \Sigma_{S_{1\to2}}\Sigma_{S_{2\to1}}} \tag{A34a}$$

$$\phi_2 = \frac{\Sigma_{S_{2\ 1}}\,q}{\Sigma'_{R_1}\Sigma'_{R_2} - \Sigma_{S_{1\to2}}\Sigma_{S_{2\to1}}} \tag{A34b}$$

$$R \equiv \frac{\phi_1}{\phi_1 + \phi_2} = \frac{1}{1 + \Sigma_{S_{2\to1}}/\Sigma'_{R_1}} \tag{A35}$$

Then R finally becomes

$$R = \frac{1}{1 + \dfrac{\Sigma_{S_{2\to1}}}{A_{eff_1} + \Sigma_{a_1} + \Sigma_{S_{1\to2}}}} \tag{A36}$$

If one holds the other properties constant and increases T, R will clearly increase giving a measure of T.

If one holds the scattering properties of the medium constant and measures R and $\int dE\phi(E)$ we see that one can measure Σ_a from Equation (A27). Then these two combined measurements should yield both Σ_a and the temperature. A_{eff_1} depends in a rather complicated way upon the diffusion and slowing down properties of the medium. One can fix the diffusion and slowing down properties in several ways. One way would be to measure the flux at large energies, for example, the cadmium shielded detector. One could measure the spatial variation of say the thermal flux.

The high energy measurement could be difficult because there are not a lot of counts. The spatial vairation might be a bit complicated in that it requires at least two detectors several inches apart.

FUTURE WORK

The curvature of $\phi(\underline{r})$ that is $\{\nabla^2 \phi(\underline{r})/\phi(\underline{r})\}$ appears to change sign somewhere in the range of distances covered in these experiments. It might be possible to optimize the distance between source and detector to eliminate A_{eff}.

From a theoretical viewpoint it would seem a good idea to solve Equation (A30) with the slowing down source from age theory (A14).

SUPPLEMENT

Now let's solve Equation (A30) for a point fast source where q is given by (A14). Define $\Sigma_{R_1} = \Sigma_{T_1} - \Sigma_{S_1}$ and $\Sigma_{R_2} + \Sigma_{T_2} - \Sigma_{S_2}$. The Green's function here is a solution of

$$\begin{bmatrix} -D_1\nabla^2 + \Sigma_{R_1} & -\Sigma_{S_{2\to 1}} \\ -\Sigma_{S_{1\to 2}} & -D_2\nabla^2 + \Sigma_{R_2} \end{bmatrix} \begin{bmatrix} q_1(\underline{r}) \\ q_2(\underline{r}) \end{bmatrix} = \begin{Bmatrix} 0 \\ \delta(\underline{r}) \end{Bmatrix} \tag{S1}$$

Then

$$q_1(\underline{r}) = -\frac{e^{-r/L_+}}{4\pi r} \frac{\Sigma_{2\to 1}}{D_1D_2(L_+^{-2}-L_-^{-2})} + \frac{e^{-r/L_-}}{4\pi r} \frac{\Sigma_{2\to 1}}{D_1D_2(L_+^{-2}-L_-^{-2})} \tag{S2}$$

$$q_2(\underline{r}) = -\frac{e^{-r/L_+}}{4\pi r} \frac{(-D_1L_+^{-2} + \Sigma_{R_1})}{D_1D_2(L_+^{-2}-L_-^{-2})} + \frac{e^{-r/L_-}}{4\pi r} \frac{(-D_1L_-^{-2} + \Sigma_{R_2})}{D_1D_2(L_+^{-2}-L_-^{-2})} \tag{S3}$$

where

$$L_\pm^{-2} = \Sigma_{R_1}\Sigma_{R_2}(D_1 + D_2) \pm \sqrt{(D_1+D_2)^2\Sigma_{R_1}^2\Sigma_{R_2}^2 - 4D_1D_2(\Sigma_{R_1}\Sigma_{R_2} - \Sigma_{S_{1\to 2}}\Sigma_{S_{2\to 1}})} * \frac{1}{2D_1D_2} \tag{S4}$$

then of course

$$\phi_1(\underline{r}) = \frac{p}{(4\pi\tau)^{3/2}} \int d^3r' q_1(\underline{r}'-\underline{r})\, e^{-r'^2/4\tau} \qquad (S5)$$

$$\phi_2(\underline{r}) = \frac{p}{(4\pi\tau)^{3/2}} \int d^3r' q_2(\underline{r}'-\underline{r})\, e^{-r'^2/4\tau} \qquad (S6)$$

This is obviously too complicated to give much in the way of physical insight. If needed numerical computations from these equations would be easy.

☆U.S. GOVERNMENT PRINTING OFFICE: 1978-740-206/160